Building Exhaust Recovery, A Small Scale Wind Turbine Design

Jeremy Lee Yandell

A thesis
submitted in partial fulfillment of the
requirements for the degree of

Master of Science in Mechanical Engineering

University of Washington

2013

Committee

Alberto Aliseda

Brian Fabien

James J. Riley

Program Authorized to Offer Degree:
Mechanical Engineering

University of Washington

Abstract

Building Exhaust Recovery, A Small Scale Wind Turbine Design

Jeremy Lee Yandell

Chair of the Supervisory Committee:

Small−scale wind turbine design is a growing field as larger utility turbine wind recovery sites are nearing saturation. We present a complete method for the design of small, application-specific turbines based on the blade element theory. This thesis consisted on the design, manufacturing and wind-tunnel-testing of the rotor of a small turbine for wind energy recovery. A complete redesign loop allowed for the implementation of lessons-learnt from the first prototype, in terms of both structural deformation and root twist starting torque, on the second prototype that was thoroughly tested for aerodynamic performance in the wind tunnel. The design process was focused on a novel motivation: the recovery of energy from building ventilation exhaust. Building exhaust systems present a unique opportunity for energy conversion based on how air is moved using a system of exhaust fans and the inefficiency and costliness of those systems. This thesis approaches this problem from a theoretical, computational and experimental perspective, with the goal of producing a practical prototype to validate the design and manufacturing process. The design takes the theoretical-optimum characteristics from blade element momentum theory. The design is refined after computational modeling, while exploring various manufacturing techniques. Prototype development and testing is used to further understand the operation of the system and optimization in preparation for the final design. A final

prototype, based on experimentation on the first design, was built and tested in the wind tunnel, providing experimental performance data for real life power generation and operating conditions evaluation. This data also allows for comparison against the design values in order to validate the design-build-test process.

-

TABLE OF CONTENTS

Page

LIST OF FIGURES

Figure Number Page

LIST OF TABLES

Table Number Page

ACKNOWLEDGMENTS

The author wished to express extreme gratitude to Proffessor Alberto Aliseda for consistent guidance, instruction, encouragement and perspective throughout this project. To my friends and colleges who contributed greatly each in unique aspects of the project. Finally, to my wife who supported me and took care of many things so that I could focus on research.

Soli Deo Gloria

Chapter 1

INTRODUCTION

1.1 Problem Statement

The goal of any exhaust system is to move air from one location to another. In the case of buildings that goal is accomplished by producing a sub−atmospheric pressure in the building or space. This leads to air being sucked into the exhaust vent and venting to the outside. In the case of fan and ducting systems the fan used to create the pressure drop also imparts velocity on the air. The below equation is a simplified expression for the power expended to move the air.

$$\delta E = \delta PQ + \frac{1}{2}\rho V^2 Q \tag{1.1}$$

There are two parts primary parts of the equation that make up the energy needed to do the work. The first part is the change in pressure (the pressure drop between the outside atmosphere and inside the building), this is the useful part of the energy, the second part is kinetic energy that a by product of the exhaust fan. The kinetic energy is what we are trying to recover without increasing the pressure drop that the exhaust system has to produce. The volume flow rate Q is determined by building need, either for clean air, heat removal, or biomedical necessity. So for a given Q, from an engineering standpoint you can reduce the required pressure drop by increasing the size of the ventilation duct, which would reduce pipe losses and velocity at the outlet. Realistically, the size of the ducts are set by building code, space constraints, and the cost of materials. Therefore, there is potiential for energy recovery in these systems.

Secondarily, building heating, ventilation, and air conditioning (HVAC) systems as well as general purpose exhaust systems are typically overpowered or oversized for the intended job. The ideal case from an energy efficiency standpoint would be building−by−building specific systems that included right−sized duct work and appropriately matched exhaust fans. This would allow for almost zero waste of energy to cool a building or move the desired amount of air. In actuality, ducting only comes in certain sizes and custom exhaust fans and motors are much more expensive than their standard size off−the−shelf counterparts. Building space, capital cost and build−to−code industry norms also limit the customization of ducting and fans to save energy, and therefore operating cost, in most commercial buildings. Almost all cases result in oversizing the system for the need. Resultantly, there is residual kinetic energy that is dissipated to the atmosphere. In some cases, however, as is true for server buildings and the medical research community, exhausting or exchanging air is essential as part of the fundamental function of the building. This thesis explores a design, from theory through prototype testing with the intention of recovering as much of that wasted energy as possible and feeding it back into the same inefficient system without affecting its normal operation in any way.

1.2 Literature Review

The concept of energy recovery from existing infrastructure is not a new idea, though its theoretical development is still in its infancy. Many patents have been filed describing various types of energy recovery systems, including many that focus on exhaust or wind energy recovery. Two such designs shown below follow a similar general concept to the one that motivates this study.

Any large−scale exhaust system has the potential for significant inefficiencies that has not gone unnoticed to inventors, engineers, and building operators. Secondly, utility−scale wind energy recovery location sites are at or nearing saturation, so alternative, smaller scale means of wind energy production are beginning to be more and more the focus of invention and design. When the energy source is significant, trade-offs can be explored to reach the best annual energy production, but when the source is small, every opportunity for efficiency should be exploited. The critical aspect in small-scale energy recovery is the efficiency of the recovery system. The focus of this research is to design a highly efficient system that recovers energy from building exhaust streams without additionally loading, hindering, or changing the characteristics of the installed system. This is accomplished by starting with an extremely efficient blade design, directly coupled with a custom generator, all surrounded by a shroud to focus, smooth, and accelerate the flow through the turbine.

The principles of the blade design come primarily from research that was accomplished for the purpose of commercial scale wind turbine design, which incidentally had their origin in the small scale wind mills used for pumping water or grinding grain [**?**]. In the book 'The Generation of Electricity by Wind Power' **?**], the basics of available power in the wind are described and the limit at which it can be extracted, as reported by Betz, is highlighted as a theoretical maximum efficiency for this type of energy conversion. The power available is given by $P = \frac{1}{2}\rho A V^3$ and Betz limit is 0.593 of that, based on an optimum axial induction factor of 1/3 calculated by the velocities in the wind far upstream, far downstream, and passing through the wind turbine. The condensed result is shown here:

$$P = \rho A V^2 (V_1 - V_2) = \rho A (\frac{V_1 + V_2}{2})^2 (V_1 - V_2) \tag{1.2}$$

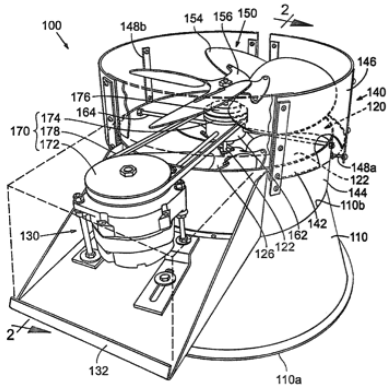

FIG. 1

(a) Vertically Mounted Turbine with Drive Belt[**?**]

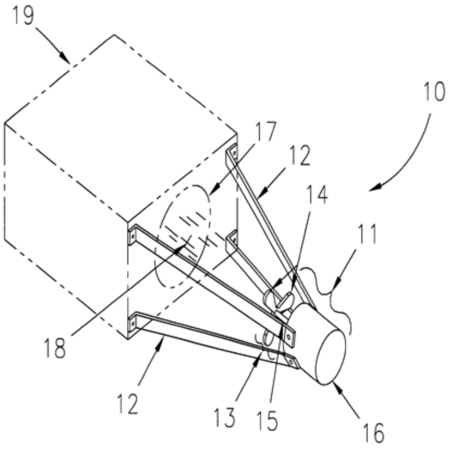

(b) Horizontally Mounted Turbine Without Shroud [**?**]

When the axial induction factor (a) is given by $a = 1 - \frac{V_2}{V_1}$ the result is:

$$P = \rho \frac{AV_1^3}{4}[(1+a)(1-a)] \tag{1.3}$$

Eggleston and Stoddard [**?**] in Wind Turbine Engineering Design, provide an important source for the broad picture of wind turbine design from concept all the way through to fatigue and turbine life considerations. They clearly make the point that if anyone focuses too narrowly on a single aspect of the system, without giving consideration to the whole picture, they will all together fail to produce a whole and complete design that accomplishes the purpose for which it was intended. They also present a critical chart shown below that illustrates where the linear momentum theory is and is not valid.

In the Aerodynamics of Wind Turbines, **?**] reviews Glauert's classical blade element momentum theory and discusses it in terms of use with a wind turbine and how a table of lift and drag coefficients verses angle of attack can be used to calculate forces of lift and drag and thus torque, thrust, power, etc. everything needed for wind turbine design. Hansen also shows how solidity ratio is included in the formulation of how the normal force and torque effect the control volume. WT_Perf and Harp−opt are codes whose foundations are the blade element momentum theory, which will be discussed later.

1.3 Theory

1.3.1 Nondimensional Numbers

In order to characterize a physical system in the most general manner, we propose a set of non-dimensional numbers that determine its behavior under different conditions. The non-dimensional numbers that characterize the flow in wind turbine design theory are the Reynolds Number and the Mach Number. Reynolds number is

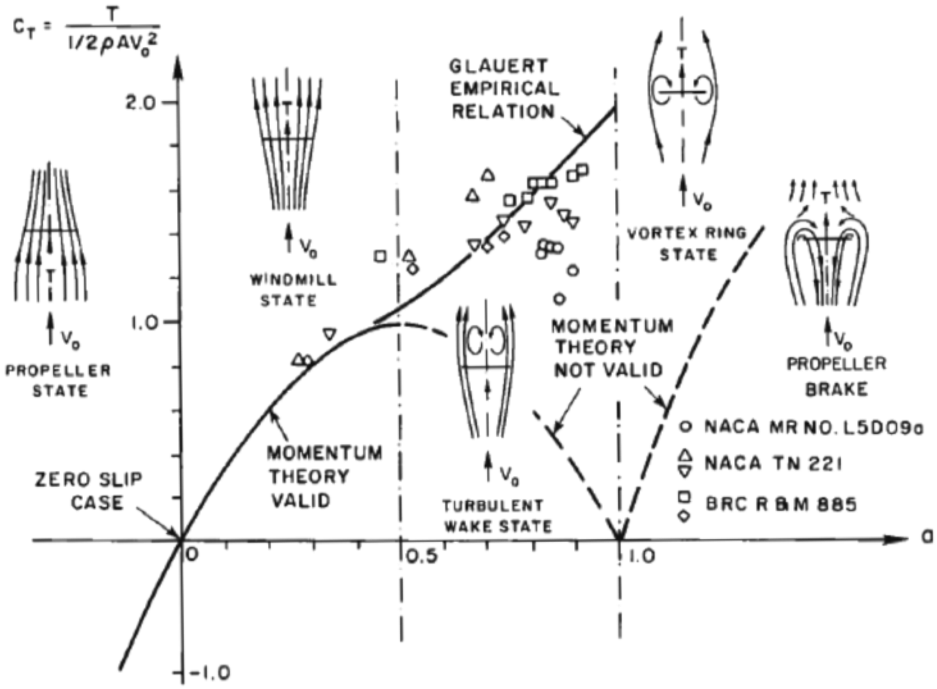

Figure 1.1: Coefficient of Thrust vs Axial Induction Factor [?]

the ratio of inertial forces to viscous forces. In this particular application, there are three important Reynolds numbers. The first is the overall Re of the system, which is found using the following equation:

$$Re = \frac{\rho V_\infty D}{\mu} \tag{1.4}$$

where D is the diameter of the turbine, ρ is the density of the fluid, V_∞ is the free stream velocity, and μ is the dynamic viscosity of the fluid. In order to determine the lift and drag data for the airfoils in the numerical simulation, the local Reynolds number is more relevant:

$$Re_{local} = \frac{\rho V_{rel} c}{\mu} \tag{1.5}$$

where c is the local chord length of the section and the relative velocity is the combination of free stream velocity and the wind speed due to rotation of the blade.

The final relevant Reynolds number is for the exhaust outlet; it is Re_*jet*.

$$Re_{jet} = \frac{\rho U_o H}{\mu} \tag{1.6}$$

Where U_o is the velocity of the jet at the outlet and H is the diameter of the jet. In the case of a square exhaust outlet the diameter of a circle with the equivalent area of the square was used. The Mach number can also be critical in the basic calculations used for simulating a turbine design, but did not play a significant part in this design. It is included here for generality and because it could become critical in future designs at other wind speeds. Mach number is defined as the ratio of the speed of an object in relation to the speed of the fluid it is in over the speed of sound of the fluid it is in. In turbine design applications, the characteristic speed is the relative velocity between the blade sections and the incoming wind. Divided by the speed of sound of air, the Ma for this wind turbine, operating at optimum performance at 11 m/s, is 0.179 midspan and 0.354 at the tip.

The turbine blade is formed by airfoils, the behavior of which is given in terms of the Coefficient of Lift (C_l) and Coefficient of Drag (C_d). The coefficients of lift and drag are defined similarly where lift, the component of the force perpendicular to the free stream velocity, or drag, the component of the force parallel to the free stream velocity is in the numerator and each are divided by half of the density times the free stream velocity squared times the chord length of the airfoil or airfoil section being evaluated.

$$C_l = \frac{L}{\frac{1}{2}\rho V_\infty^2 c} \tag{1.7}$$

$$C_d = \frac{D}{\frac{1}{2}\rho V_\infty^2 c} \tag{1.8}$$

The overall performance of the turbine, in terms of aerodynamic forces and power generation, is reported in non-dimensional terms for comparison between designs as the Coefficient of Thrust (C$_T$), Coefficient of Torque (C$_Q$) and Coefficient of Power (or Performance) C$_P$. There are multiple ways to define both the C$_P$ and the C$_T$. When designing a turbine starting with theory, C$_P$ and the C$_T$ can be expressed in terms of the axial induction factor used in the Blade Element Momentum Theory:

$$C_P = 4a(1-a)^2 \tag{1.9}$$

$$C_T = 4a(1-a) \tag{1.10}$$

More generally, however, the Coefficient of Power is defined as the power extracted by the turbine divided by the total power available in a 'stream tube' of the wind with the same diameter of the turbine.

$$C_P = \frac{P}{\frac{1}{2}\rho V_\infty^3 A} \tag{1.11}$$

You can easily notice the similarity between the two formulations where the Coefficient of Thrust is written as:

$$C_T = \frac{T}{\frac{1}{2}\rho V_\infty^2 A} \tag{1.12}$$

The Coefficient of Torque is given the label C$_Q$ so as not to confuse it with thrust. This coefficient is formulated by dividing the torque by the momentum of the wind using the free stream velocity.

$$C_Q = \frac{T_r}{\frac{1}{2}\rho R V_\infty^2 A} \tag{1.13}$$

In the case of this design the blade speed is significant in comparison to the incoming wind speed. This comparison is made using another non-dimensional ratio, which is also key in the operation of the rotor. It is the Tip Speed Ratio (TSR or λ), which simply defined, is the ratio of the speed of the rotor divided by the wind speed.

$$\lambda = \frac{\Omega R}{V_\infty} \tag{1.14}$$

TSR is also equivalent to the coefficient of power divided by the coefficient of torque. Figure 1.2, below, shows the Power, Thrust (or Drag) and Torque for four different operating conditions, on the left. On the right, we can observe the collapse of the non-dimensional performance metrics, C_P, C_T, C_Q, when plotted as a function of TSR, the non-dimensional rotational speed of the rotor.

1.3.2 Blade Element Theory

The calculations for blade design were conducted with WT_Perf, a code developed by the National Renewable Energy Laboratory. Shroud design calculations were run in ANSYS Fluent (Ansys Inc., Cannonsburg, PA.), a commercial code that uses the finite volume formulation. The shroud simulations were conducted using the Reynolds Averaged Navier Stokes equations with a closure model for turbulent fluctuations. The presence of the turbine rotor was simulated using the Virtual Blade Model, a rotor−modeling tool programmed within Fluent. Both WT_Perf and the Virtual Blade Model are based on Blade Element Theory, a technique to calculate rotor performance and flowfield originally developed for helicopter rotors that has been extensively applied to wind turbine studies. For a horizontal axis turbine design, the BET divides the blade into spanwise sections, considering the resulting two-dimensional airfoil geometry and flowfield associated with each of those “slices”. Coefficients of lift and drag in tabular form are required as input information into the BET computation. These are typically provided by existing experimental data from the literature or two dimensional computational fluid dynamics models, such as XFoil. That information, along with the blade sections

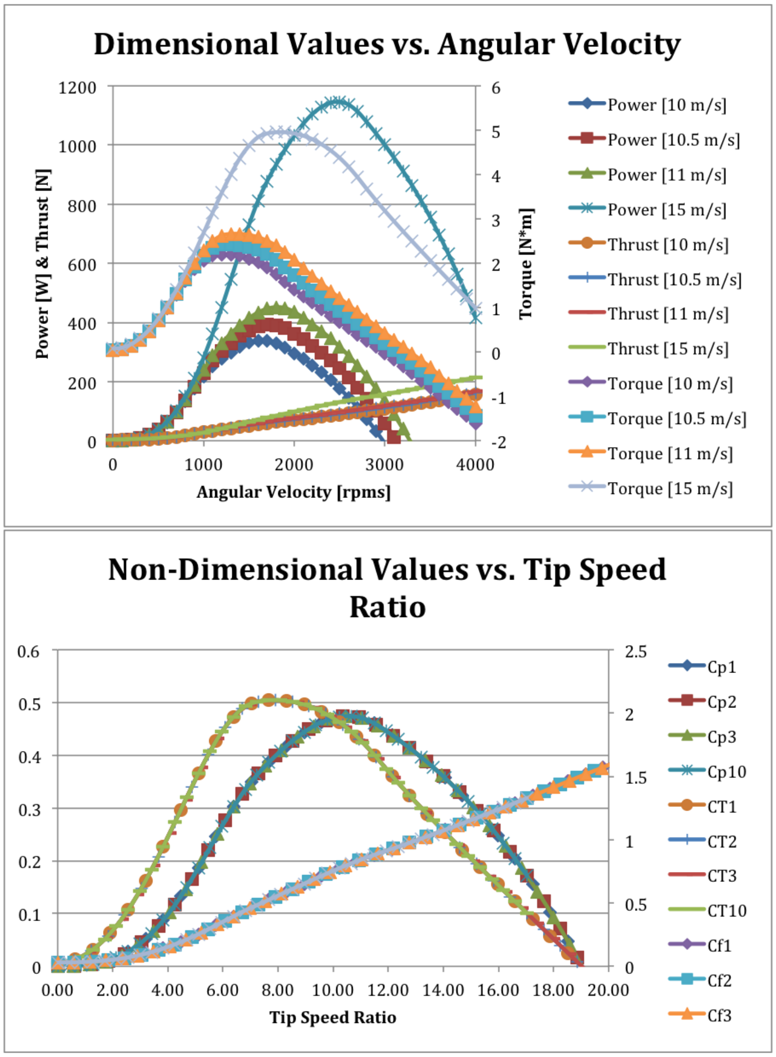

Figure 1.2: Dimensional vs. Non-Dimensional Values

total pitch angle (the combination of local twist and overall pitch) that is already known from the blade geometry and relative wind direction are used to calculate torque and power of the airfoil section. The relative wind direction is a combination of the incoming wind velocity and the rotational velocity of the blade sections resulting from the blade rotation.

This velocity due to rotation is particularly important in this thesis because the design of this wind turbine is critically influenced by the desired angular velocity of the output shaft, which is determined by the electrical generator properties and the choice of a direct drive between the rotor and the generator, with no gears to accommodate their rotational speeds.

The BET implementation imposes the forces of the blade on the fluid flow and iterates in calculating the wind speed, resulting angle of attack and lift and drag forces and feeding back into the flow, until the solution converges. At that point the forces on the blades are calculated for each section it has been discretized into, and the resulting data is integrated along the span of the blade to obtain thrust, torque and power.

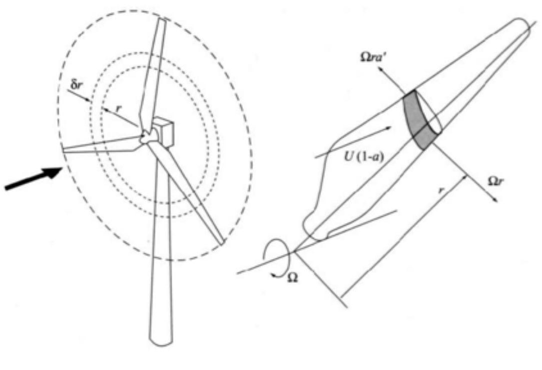

Figure 1.3: Span-wise Dissection of Turbine Blade [?]

1.3.3 Blade Element Momentum Theory

In Blade Element Momentum Theory the concepts from blade element theory and linear momentum theory are combined to form a basis for theoretical design. By connecting the basic dimensions of the design to the axial induction factor, a simple relationship is made by which to optimize the design based on the ideal axial induction factor of 1/3. The following equation is the foundation of the BEMT.

$$\frac{V_\infty - u}{u} = (\frac{Bc}{8\pi r})(\frac{c_l cos(\theta) + c_d sin(\theta)}{sin^2(\theta)}) \tag{1.15}$$

For uniformity V_∞ is used as the free stream velocity in place of V_o and u is the local velocity at the blade section. r is the radial location of the section being evaulated and θ is the local combined pitch and twist. This equation can be rewritten using the non−dimensional solidity ratio σ. In general solidty ratio is the ratio of the total swept area of the blade to the area that the blades physically occupy. **?**] uses the retangular solidity ratio when rewriting the above equation, which assumes that the blade has a the same chord length along the span of the blade. The local solidity ratio is more applicable for our case and is given by $\sigma = \frac{Bc}{2\pi r}$. This ratio diverges at the root, but is applicable everywhere else. Though the overarching equation accounts for the twist, none of the formulations for solidity take into account the effect of twist or pitch on the solidity that the incoming velocity encounters. The new formulation is important because it is incoporated into the functionality of WT_Perf and is the basis for explaining why the algorithm tends towards lower solidity blades for higher tip speed ratios. Also recalling the definition of the axial induction factor $a = 1 - \frac{V_2}{V_1}$.

$$\frac{a}{1-a} = (\frac{\sigma}{4})(\frac{c_l cos(\theta) + c_d sin(\theta)}{sin^2(\theta)}) \tag{1.16}$$

1.3.4 Shroud Design Theory

Though the size of conventional wind turbines makes the use of shrouding, or flow conditioning, impractical, small−scale turbines can greatly benefit from their use. In addition to a nose cone, a correctly sized shroud can improve overall performance. The main goal of adding a flow conditioner is to provide support for the flow as it goes around the blade tips. Flow swirling on the blade tip bypasses the airfoil sections near the edge of the blade, reducing performance and inducing the characteristic blade-tip vortices that dominate the turbines near wake. This mechanism reduces performance by decreasing the pressure difference across the blades suction and pressure surfaces precisely at the largest radial location, where this pressure difference can produce the most torque. There are two other secondary effects that can take advantage from the presence of a shroud: first it should increase the mean velocity of the flow, which is critical when power extracted from the flow is a cubed function of wind speed. Secondly, flow uniformity and reduced longitudinal and radial turbulence will improve the power output of the system. In a study by Hussain and Ramjee [**?**], four axisymmetric contraction shapes were experimentally studied to determine the effects of contraction shape on incompressible turbulent flow. The four shapes are displayed with dimensional indicators for each. Ultimately, all of the contractions produce the same mean outlet flow field. However, the turbulent intensity and distribution varies with each design as well as the effect of the contraction on the upstream flow. The cubic equation contour (a) was the preferred design for our application, because our goal is to minimize upstream influence of the turbine, and because it results in the lowest turbulent intensity in the boundary layer. The equation governing the shape of the cubic contour is:

$$R = \frac{D_i}{2} - \frac{3}{2}(D_i - D_e)(\frac{x}{L})^2 + (D_i - D_e)\frac{x}{L}^3 \tag{1.17}$$

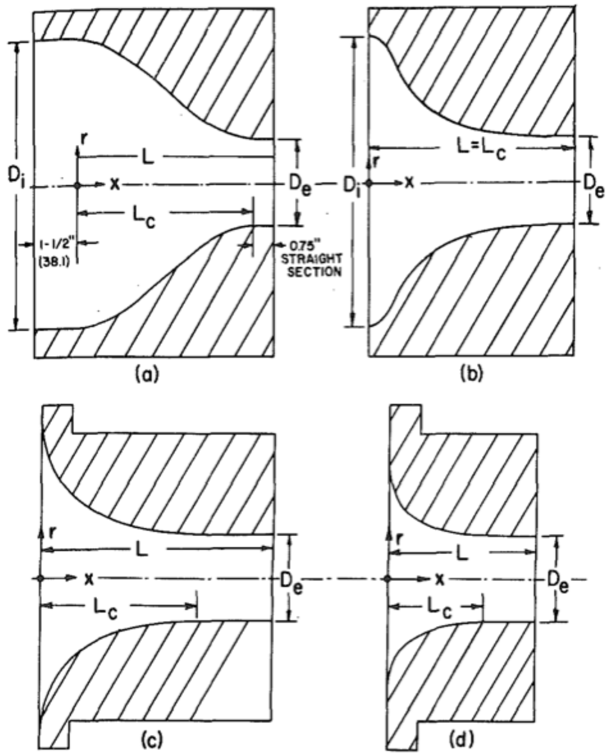

Figure 1.4: Axisymmetric Contraction Shapes[**?**]

The contraction ratio for each shape is defined by the ratio of the inlet diameter squared to the outlet diameter squared:

$$c = (\frac{D_i^2}{D_e^2}) \tag{1.18}$$

Linear theory suggests that longitudinal turbulent kinetic energy monotonically decreases for increasing values of geometric contraction ratio. However, the experimental results by Hussain and Ramjee indicate that longitudinal turbulent kinetic energy decreases for contraction ratios up to about 4 and then increases through ratios up to 11. For this contraction design a smaller contraction ratio was chosen due to the fact that this turbine is not in an infinite or approximately infinite free stream velocity. For a 4-foot diameter exhaust outlet and a turbine located at 2 feet from the flow exit, the entire jet expansion can be captured by a shroud inlet diameter of 58 inches. This results in a geometric contraction ratio of 1.37.

The next point of concern is where to locate the turbine inside the contraction. The ideal location would be the place of highest velocity and lowest turbulent intensity. Figure 1.6 indicates that the location of max velocity is in the range of x/l of 1.2 to 1.6, which is just downstream of the contraction shape, but still within the overall form. Note that both longitudinal and radial turbulence intensity are dramatically reduced at this location. Further research on the topic of increasing wind turbine efficiency with shrouds yields a completely different concept for shroud design. Bare

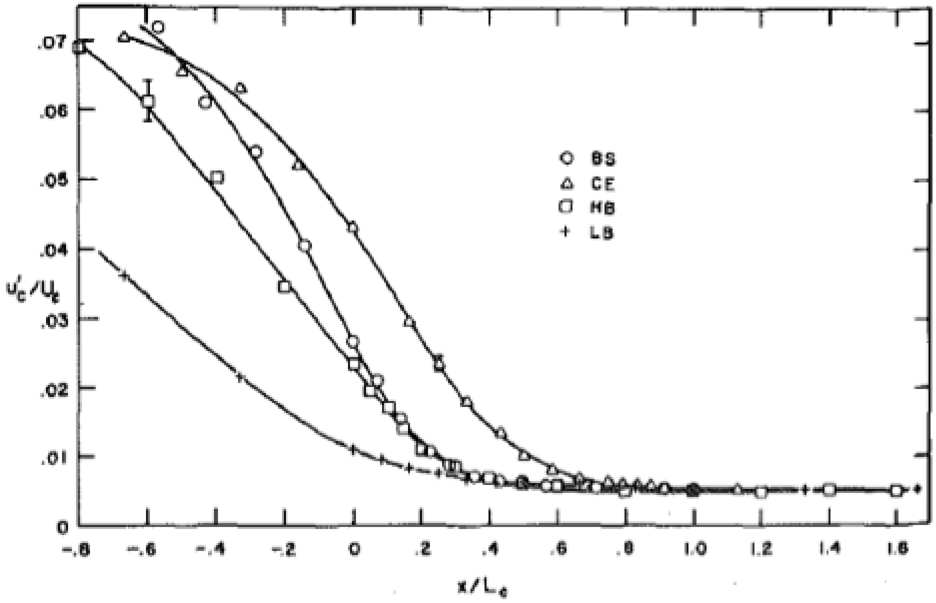

Figure 1.5: Centerline Variation of Longitudinal Turbulence Intensity Through the Contraction [?]

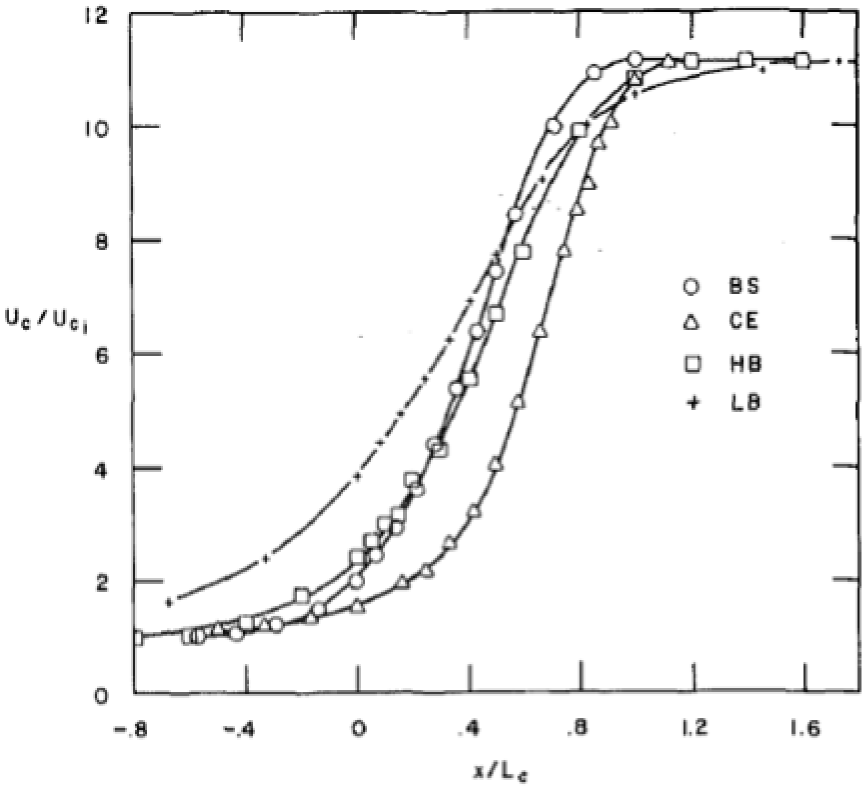

Figure 1.6: Centerline Variation of Velocity Through the Contraction [?]

wind turbines present a blockage to the flow, which results in an increase in pressure locally and in some cases upstream of the rotor disk. As previously discussed, back-pressure in our system would be a significant issue because it could change the operating characteristics of the exhaust system. Additionally, this blockage is the key theoretical concept behind the Betz limit that establishes a maximum efficiency for turbines in the free stream of 59%. Though the cubic shaped nozzle improves the overall flow characteristics seen by the turbine, it fundamentally operates on back-pressure as well. An airfoil-shaped ducted system, as shown in Figure 1.8,

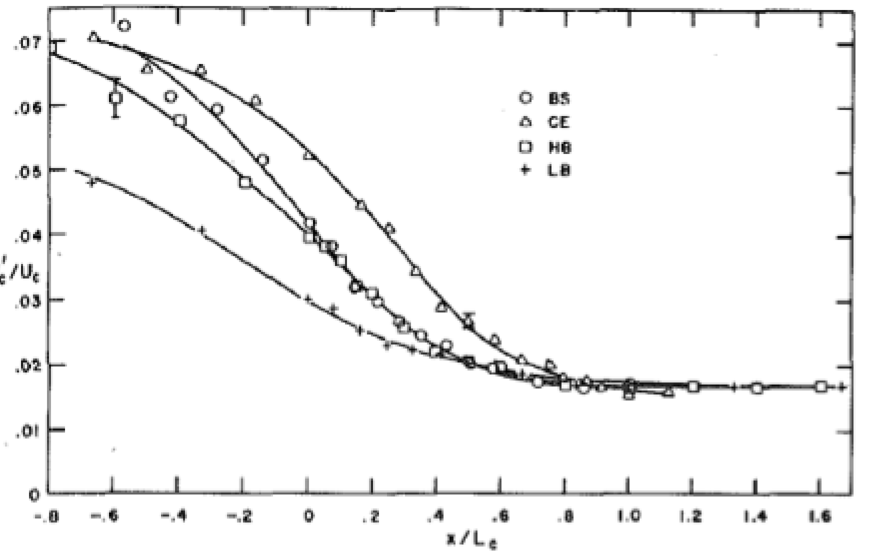

Figure 1.7: Centerline Variation of Radial Turbulence Intensity through the of the Contraction [?]

could lead to significant advantages in power production and efficiency. This type of shroud uses the aerodynamic forces on the airfoil-shaped cross section to create a low-pressure zone, the classical peak minimum pressure near the leading edge of the suction side, just behind the turbine blades. This effect can reduce the pressure in front of the turbine to and even below local pressure. The associated flow increase provides the potential to significantly increase the power production of a wind turbine. The aerodynamic “funneling induced by the shroud on the free stream flow (assumed to be infinite) leads to higher kinetic energy density at the turbine rotor than present in the free stream, and thus efficiencies higher than Betz limit are possible, when defined in terms of the cross sectional area of the rotor. If defined in terms of the maximum cross sectional area of the shroud on the outside flow, which is the “capture area for this turbine, the efficiency would still be limited by Betz theory. Werle and Presz [**?**] have explored this mechanism of energy conversion numerically and experimentally and found efficiency could reach levels up to about 0.83. Two other advantages of this type of shroud design also lend themselves to our application. First, the size of the airfoil shaped duct does not have to have a long chord length, thus saving on material cost, though the structural loads required to sustain the high pressure difference between the pressure side of the airfoil (outside of the shroud) and the suction side of the airfoil (the inside of the shroud) would be significant and determine the design and manufacturing process. Additionally, it is

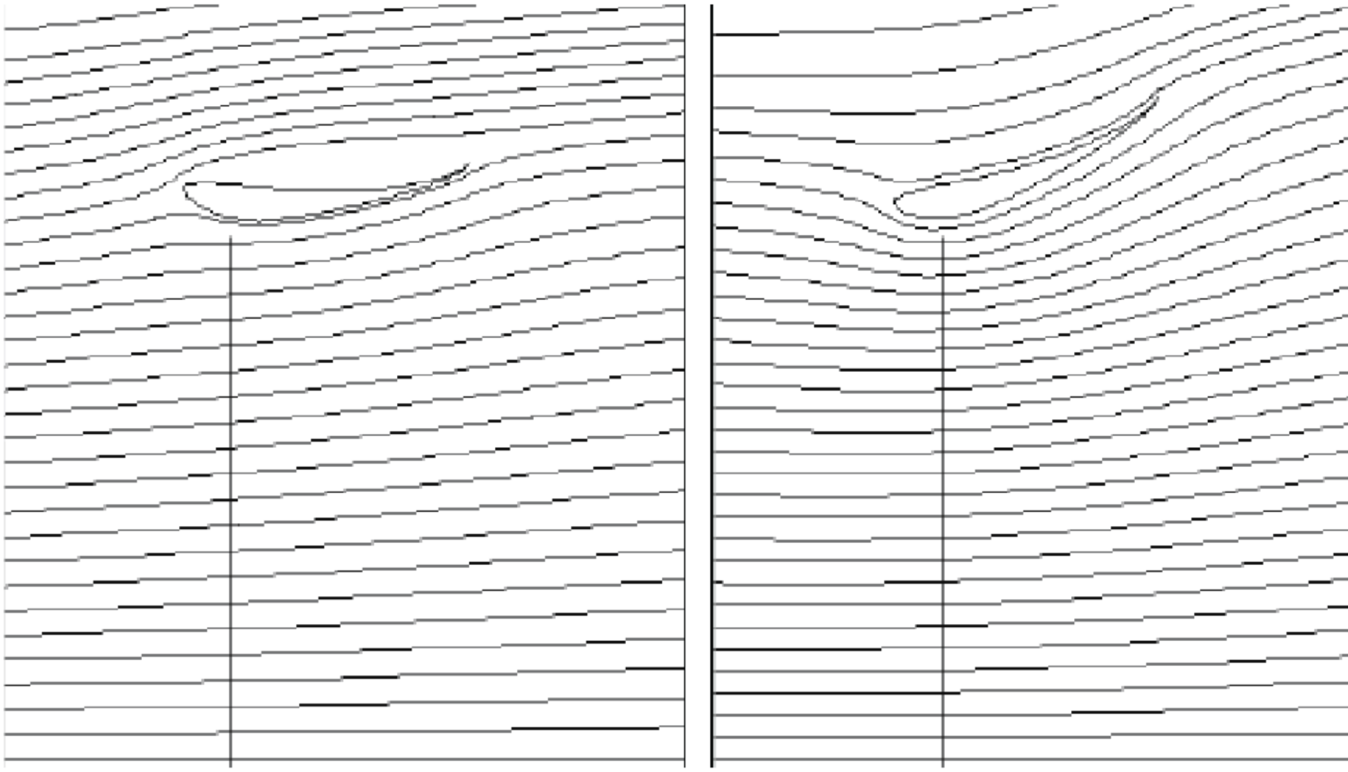

Figure 1.8: Crosssection of Ducted Turbine [**?**]

important to remember that any strut or support member that obstructs the smooth flow around the outside of the shroud (even near the trailing edge) would add a penalty in the aerodynamic effectiveness of the shroud as an airfoil, and therefore on the efficiency of the turbine inside. Secondly, because the shape of the shroud (both inside and outside has to be very accurately modeled and manufactured to exact specifications for it to operate adequately, a very narrow gap between the turbine blades and the shroud inside can be naturally designed and implemented. This will lead to a significant reduction of tip losses that represent an important loss of torque and power to any airfoil-shaped wing or blade application.

Chapter 2

METHODS

2.1 Numerical Methods

2.1.1 WT_Perf

WT_Perf is a software code, based on BEMT, that rapidly provides power, torque, moment, thrust, and coefficient of performance data. One important note is knowing generally what your given parameters are, because, from a theoretical perspective, a blade can be optimized for high efficiency at multiple points. The required inputs are number of blades, rotor and hub radii, coefficient of lift and drag for a range of angle of attack for the given airfoil or airfoils, and pre-twist and chord values. Though the inputs can be limiting, wind speed or tip speed ratio, angular velocity, and pitch can all be varied simultaneously to evaluate many predesigns in a short time. This allows the user to quickly narrow parameters, saving a significant amount of time, in order to move on to more detailed analyses.

2.1.2 Harp−Opt

Harp−Opt utilizes WT_Perf in a batch mode to run thousands or millions of possible blade configurations, and is able to optimize the twist and chord values that previously were fixed inputs. This code uses a multiple objective genetic algorithm that uses evolutionary principles for a population of parameter sets that adapt to find combinations of parameters that yield better metrics. This process can converge to a non−physical result and thus the output most be closely evaluated to ensure that the results are what is expected for the design. The program can take up to 3 or 4 hours to find an optimum design, therefore WT_Perf should be used whenever possible to eliminate or reduce the variables in order to decrease the overall time for Harp−Opt to converge. Figure 2.1 is a view of the input screen. This software has the ability to not only search for an optimum aerodynamic design

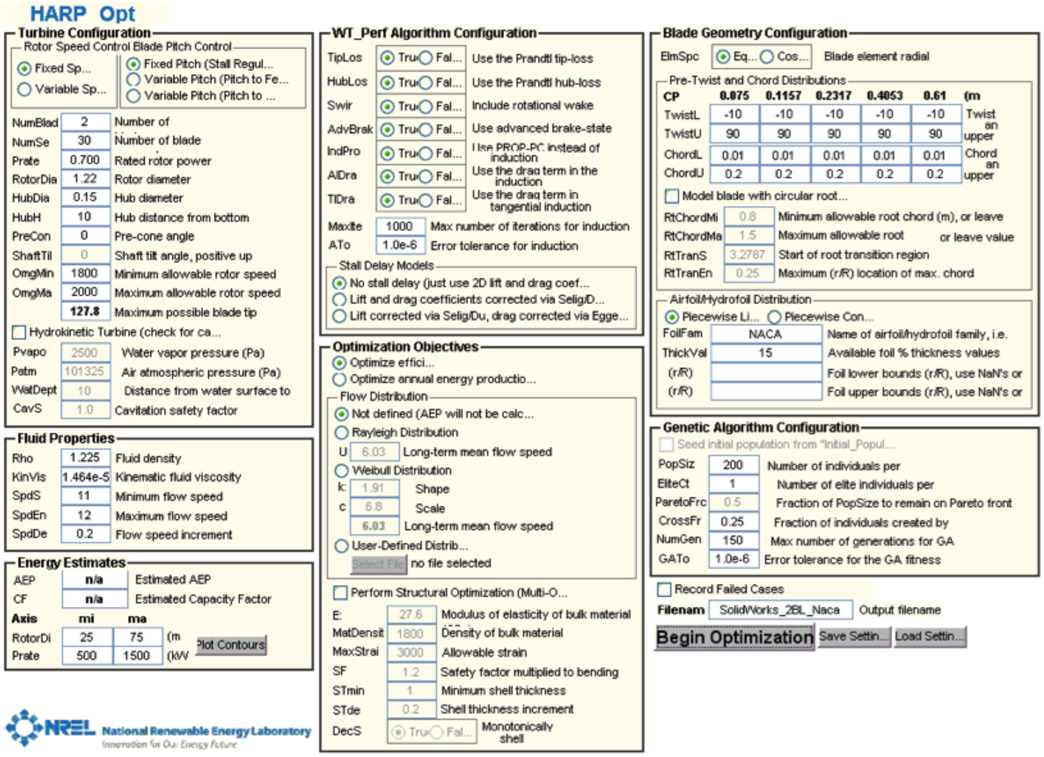

Turbine Configuration

Rotor Speed Control Blade Pitch Control
● Fixed Sp...
○ Variable Sp...
● Fixed Pitch (Stall Regul...
○ Variable Pitch (Pitch to Fe...
○ Variable Pitch (Pitch to ...

NumBlad	2	Number of
NumSe	30	Number of blade
Prate	0.700	Rated rotor power
RotorDia	1.22	Rotor diameter
HubDia	0.15	Hub diameter
HubH	10	Hub distance from bottom
PreCon	0	Pre-cone angle
ShaftTil	0	Shaft tilt angle, positive up
OmgMin	1800	Minimum allowable rotor speed
OmgMa	2000	Maximum allowable rotor speed
	127.8	Maximum possible blade tip

☐ Hydrokinetic Turbine (check for ca...

Pvapo	2500	Water vapor pressure (Pa)
Patm	101325	Air atmospheric pressure (Pa)
WatDept	10	Distance from water surface to
CavS	1.0	Cavitation safety factor

Fluid Properties

Rho	1.225	Fluid density
KinVis	1.464e-5	Kinematic fluid viscosity
SpdS	11	Minimum flow speed
SpdEn	12	Maximum flow speed
SpdDe	0.2	Flow speed increment

Energy Estimates

AEP	n/a	Estimated AEP
CF	n/a	Estimated Capacity Factor

Axis	mi	ma	
RotorDi	25	75	(m
Prate	500	1500	(kW

WT_Perf Algorithm Configuration

TipLos	● Tru ○ Fal...	Use the Prandtl tip-loss
HubLos	● Tru ○ Fal...	Use the Prandtl hub-loss
Swir	● Tru ○ Fal...	Include rotational wake
AdvBrak	● Tru ○ Fal...	Use advanced brake-state
IndPro	● Tru ○ Fal...	Use PROP-PC instead of induction
AIDra	● Tru ○ Fal...	Use the drag term in the induction
TIDra	● Tru ○ Fal...	Use the drag term in tangential induction
MaxIte	1000	Max number of iterations for induction
ATo	1.0e-6	Error tolerance for induction

Stall Delay Models
● No stall delay (just use 2D lift and drag coef...
○ Lift and drag coefficients corrected via Selig/D...
○ Lift corrected via Selig/Du, drag corrected via Egge...

Optimization Objectives
● Optimize effici...
○ Optimize annual energy productio...

Flow Distribution
● Not defined (AEP will not be calc...
○ Rayleigh Distribution

U	6.03	Long-term mean flow speed

○ Weibull Distribution

k:	1.91	Shape
c	6.8	Scale
	6.03	Long-term mean flow speed

○ User-Defined Distrib...
no file selected

☐ Perform Structural Optimization (Multi-O...

E:	27.6	Modulus of elasticity of bulk material
MatDensit	1800	Density of bulk material
MaxStrai	3000	Allowable strain
SF	1.2	Safety factor multiplied to bending
STmin	1	Minimum shell thickness
STde	0.2	Shell thickness increment
DecS	● Tru ○ Fal...	Monotonically shell

Blade Geometry Configuration

ElmSpc	● Eq... ○ Cos...	Blade element radial

Pre-Twist and Chord Distributions

CP	0.075	0.1157	0.2317	0.4053	0.61	(m
TwistL	-10	-10	-10	-10	-10	Twist an
TwistU	90	90	90	90	90	upper
ChordL	0.01	0.01	0.01	0.01	0.01	Chord an
ChordU	0.2	0.2	0.2	0.2	0.2	upper

☐ Model blade with circular root...

RtChordMi	0.8	Minimum allowable root chord (m), or leave
RtChordMa	1.5	Maximum allowable root or leave value
RtTranS	3.2787	Start of root transition region
RtTranEn	0.25	Maximum (r/R) location of max. chord

Airfoil/Hydrofoil Distribution
● Piecewise Li... ○ Piecewise Con...

FoilFam	NACA	Name of airfoil/hydrofoil family, i.e.
ThickVal	15	Available foil % thickness values
(r/R)		Foil lower bounds (r/R), use NaN's or
(r/R)		Foil upper bounds (r/R), use NaN's or

Genetic Algorithm Configuration

☐ Seed initial population from "Initial_Popul...

PopSiz	200	Number of individuals per
EliteCt	1	Number of elite individuals per
ParetoFrc	0.5	Fraction of PopSize to remain on Pareto front
CrossFr	0.25	Fraction of individuals created by
NumGen	150	Max number of generations for GA
GATo	1.0e-6	Error tolerance for the GA fitness

☐ Record Failed Cases

Filenam	SolidWorks_2BL_Naca	Output filename

Figure 2.1: HARP-Opt Input Screen[?]

but also to optimize the structure. Structural optimizations were intended for commercial scale design and thus are not applicable for this thesis. Another unused option is the Annual Energy Production optimization. The environment that is being studied here has the ideal situation where wind speed and direction is constant, therefore efficiency is the sole objective of the optimization. Inputting a range of flow speed is essential for the program to operate on a basic level, so even though the goal of the design is to be the most efficient at a single wind speed, a range is required even if the intervals are very small.

2.1.3 FLUENT

The computer simulation of the operating environment of the turbine was performed using ANSYS FLUENT software. This software uses a finite volume method to solve for the fluid properties. A specific advantage of this type of formulation is that it, by its nature, satisfies the conservation laws at every point. Unlike the finite difference and the finite element approaches which calculate local values at mesh points, finite volume averages values in an entire cell (e.g. a control volume), solves the equations of motion (the Reynolds Averaged Navier-Stokes equations in this case), and then associates those values with a mesh point (the cell centroid). Though this type of formulation works very well with structured and unstructured meshes, mesh creation and type is still very important in ensuring an accurate solution.

There were two main objectives of the domain that was created for the simulation; one of which makes my domain a unique application to small wind turbine design. Given that the desired location of the turbine is a rooftop, unlike commercial scale wind turbines, the no-slip boundary condition along the plane below the turbine plays a critical role in understanding the operation and dynamics of this system.

Most unique in this domain is the jet expansion. In the case of exhaust systems, we are operating in the wake of a turbulent jet as opposed to a uniform free stream flow or even a restricted channel flow.

Figure 2.2 shows the complete domain with the jet expansion, surrounding volume with rooftop and the rotor disc. The mesh was shaped to include the jet volume

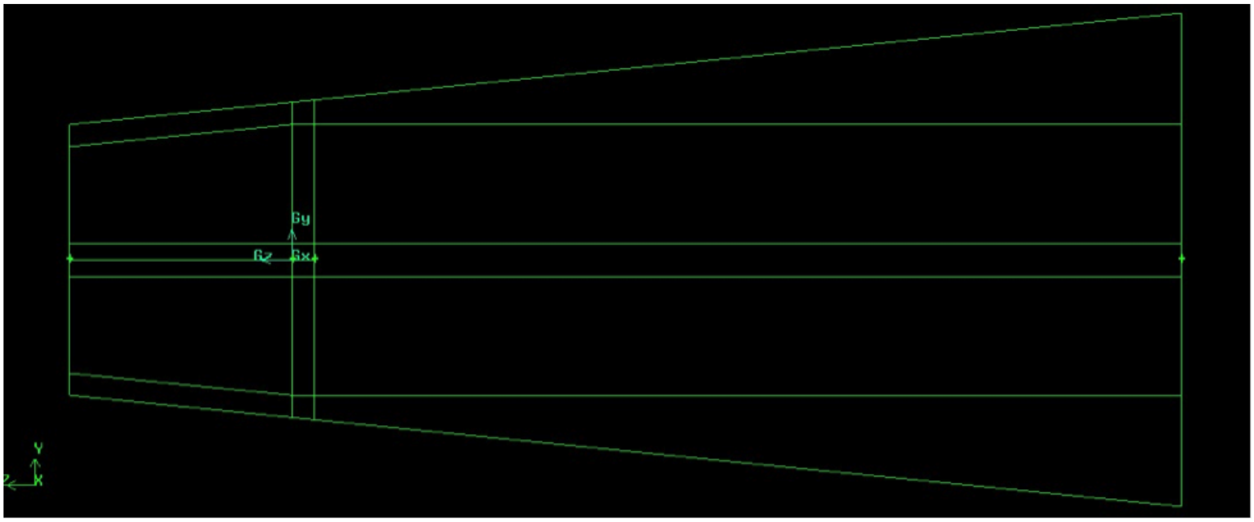

Figure 2.2: Computational Domain

expansion to prevent the boundary between the finer mesh near the rotor and the courser mesh from the outer volume from impeding the natural jet expansion in the simulation. The exact dimensions were developed based on a turbulent jet. Turbulent jet theory states that for any given Reynolds Number the boundary layer of the jet expands linearly with the distance downstream of the jet. For Reynolds numbers approaching infinity the slope of the expansion is 0.110 Panton argues that $\delta = Cx$ where C = 0.110 when $Re- > \infty$ based on experimental data. To cover the jet expansion region well within the mesh created in the domain between the ventilation exhaust and the turbine disk, in our case where the jet Re is on the order of 1 million, we adopted a uniform slope for the fine mesh of 0.2 and the result can be seen in the previous figure.

2.1.4 Virtual Blade Model

The Virtual Blade Model (VBM) is ANSYS Fluents implementation of the Blade Element Theory (BET). VBM averages the lift and drag forces on the different sections of the blades through an entire rotation of the turbine rotor, thus creating a body force per unit volume that is applied on the mesh cells that compose the rotor disk. This implementation is capable of determining power and torque characteristics with higher accuracy at a lower computational cost, in comparison to modeling the actual geometry of the blade as is done by the Single Reference Frame model[**?**].

VBM requires the user to select a discretization of the blade into radial slices, up to a maximum of 20 from a minimum radius where the blade emerges from the hub, to the tip. At each radial slice, the blade element is characterized by its chord length, its twist angle (added to the global pitch angle provided by the user for the entire blade), and the lift and drag coefficient as functions of angle of attack tables for the airfoil that conforms that blade section. Additionally, the VBM requires inputs on the rotor such as number of blades, rotor radius, rotational speed of operation and pitch angle. With this information, the VBM takes the local wind speed impinging on each blade section, composes it with the rotational velocity at that radial position to form the relative wind speed, calculates the effective angle of attack adding the pitch and twist angle to the angle formed by the relative wind speed with the rotor disk plane, and calculates the aerodynamic forces from the lift and drag lookup tables. Those tables include the possibility of making the Cl and Cd coefficients dependent on the Reynolds number and the Mach number. For the work in this thesis, the Mach number dependency was not considered and the Reynolds number of the blade elements was in a narrow range (one of the advantages of the exhaust energy recovery wind turbine is that it works in almost constant wind speed) and therefore there was no need to introduce data for widely differing Reynolds numbers. The information on the lift and drag on each blade elements is averaged over an entire revolution and then divided over the volume occupied by that blade element as it rotates forming a ring. The reaction forces, the same forces applied on the blade element, but with opposite direction, are then applied on the fluid inside the rotor volume. With these forces, a new flow velocity is calculated by solving the Navier-Stokes equations, and the process is repeated iteratively, until the flow field is in equilibrium with the forces exerted on it by the turbine rotor. The thrust (or drag), torque and power on the rotor can be calculated by integrating the aerodynamic forces calculated by VBM on each blade section, at convergence. The flow field around the turbine can also be investigated. Most important for this application, the influence of the turbine on the pressure field at the exhaust inlet was studied. The effect of turbine location on power production could also be analyzed.

2.2 Experimental Methods

2.2.1 Brake Selection

The next effort was to acquire a braking system with a torque range up to 9 Nm and with an angular speed range of 1600 to 2500 rpms. Three types of controllable brakes were considered: magnetic particle, eddy current, and hysteresis brakes. Magnetic particle brakes have a cylindrical drum that is attached to the input shaft, a gap that is filled with finely ground magnetic particles and an inner cylinder that is fixed to the casing, and a set of windings that surround the outer drum. When electric current is passed through the windings a magnetic field is generated that links the inner cylinder with the outer drum. The tensile and shear forces of the magnetic connection resist the relative motion of the two members. This force is directly related to the current and independent of the shaft speed. Though particle-braking systems have the ability to brake at the desired torque, readily available brakes were not able to handle a high angular velocity in combination with our torque requirements. Additionally, these types of brakes provide a constant torque independent of angular velocity, which is the opposite of how a generator would operate with a wind turbine. Thus this type of brake is not useful for our application. The hysteresis brake is another option that is desirable because it is commercially available in ratings that handle both the torque and angular velocity requirements. Below are two figures that illustrate the basic components of a

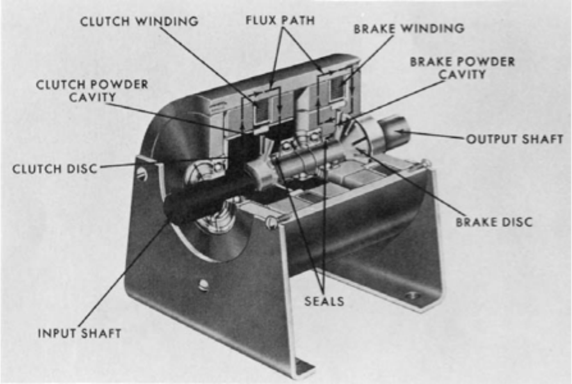

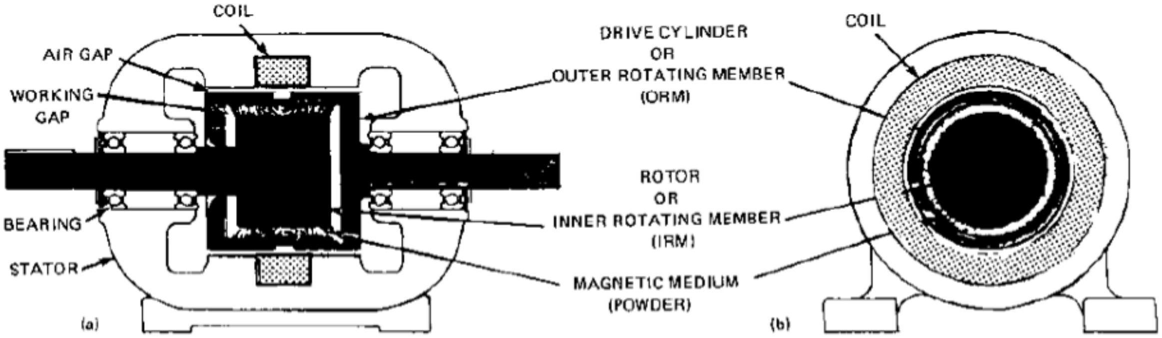

Figure 7 Magnetic lines of force linking the outer member (OM) and the inner member (IM). (Courtesy of Sperry Electro Components, Durham, NC.)

hysteresis brake.

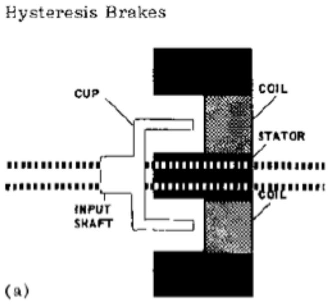

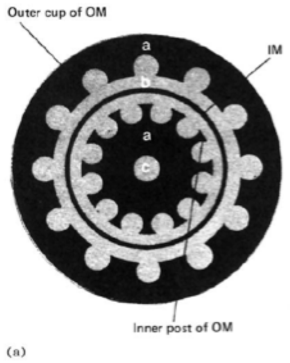

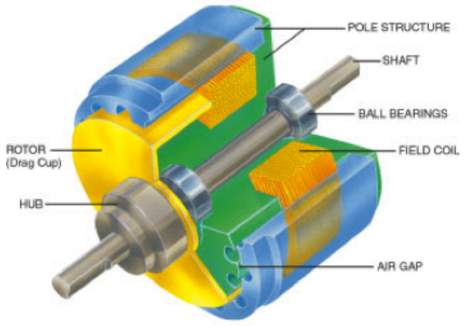

Hysteresis brakes are designed such that the stator wells and posts alternate polarity with energized with a current. That magnetic field is disturbed when the rotor turns because the rotation tends to pull opposite poles apart and push opposing poles together. The rotor is made up of a material that resists a change in magnetism. This type of brake can be controlled to produce a constant torque, but the upper limit of that torque decreases with increasing angular velocity. In the case of wind power torque increases with increasing wind speeds and thus typically higher torque is produced at a higher angular velocity for a higher wind speed. The preferred braking system is the eddy current brake because it is able to handle the required parameters and controls the turbine in a similar manner to how a coupled generator would in a realistic environment. Eddy current brakes are designed similarly to hysteresis brakes except that the rotor is made up of a material that easily responds to magnetic field changes. Eddy currents are generated on the rotor that oppose the change of magnetic field that occurs as the rotor turns.

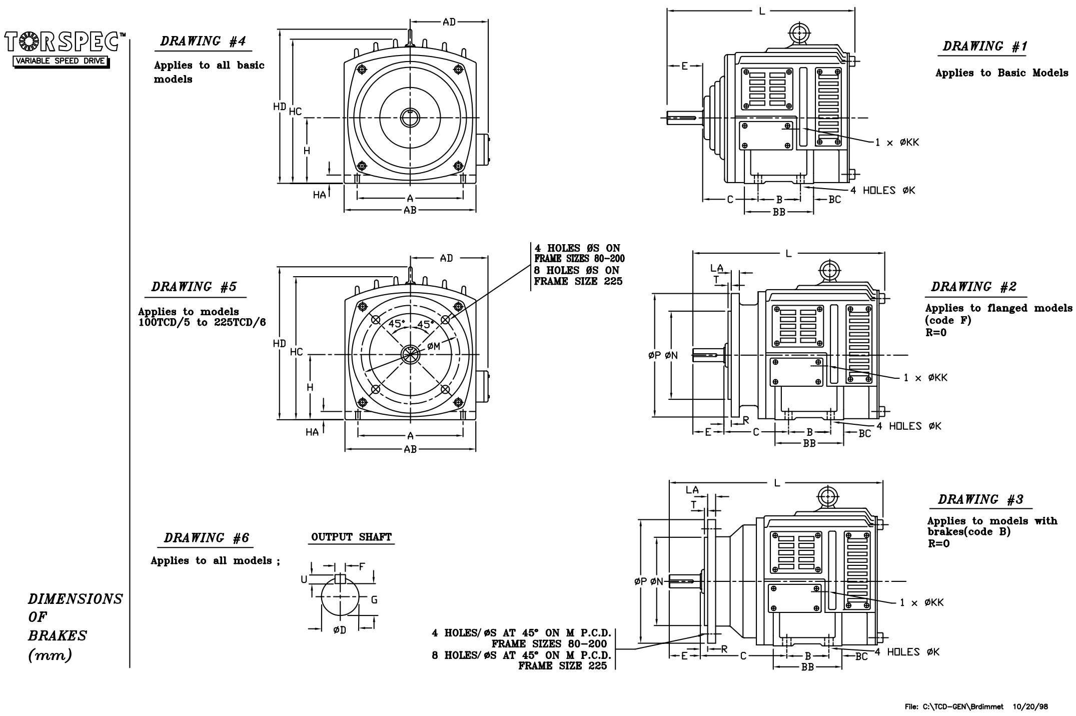

Figure 2.3: Eddy Current Brake Dimensional Drawings

The selected brake is a Torspec model 100TCD/5 that has a maximum angular velocity of 3600 rpms at 9 Nm of torque and it was coupled with the S5702TCP closed loop controller. Figure 2.4 is S5702TCP control board for the torspec brake. This particular system was designed for small industrial applications involving assembly lines where the conveyor belts require either controllable speed or

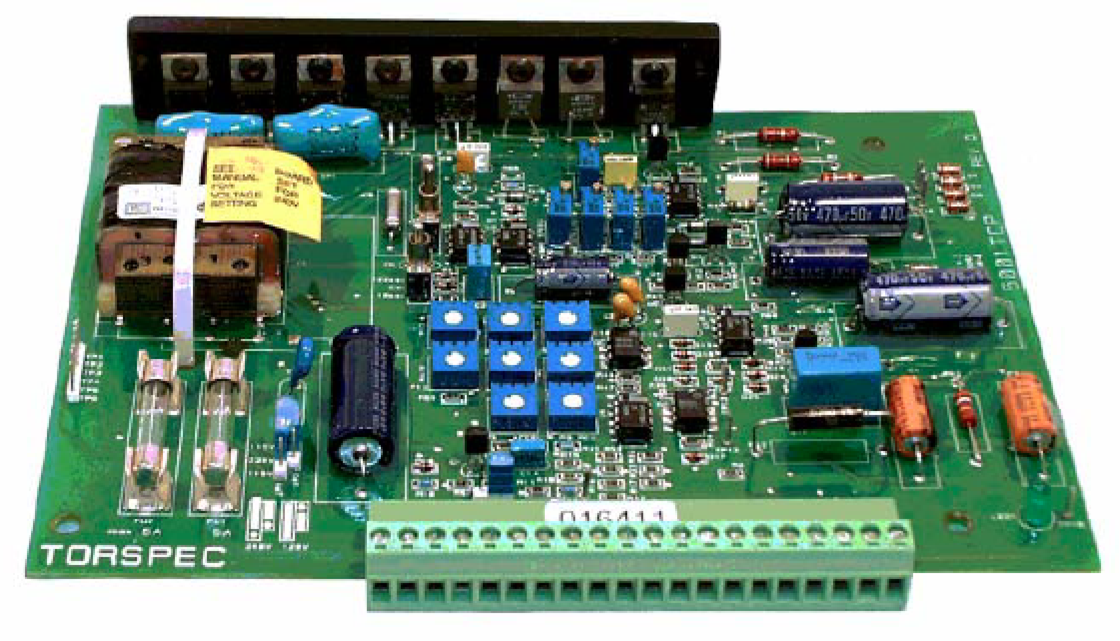

Figure 2.4: S5702TCP Control Board

controllable tension. This was particulary useful in our tests because we also needed controllable angular velocity. The controllable velocity also has a direct relationship with torque which can be evaluated so that the single controller will replace the brake, encoder, and torque cell.

Chapter 3

ROTOR DESIGN AND MANUFACTURING

3.1 Design Process

3.1.1 Blade Design

The initial phase of the design for a small−scale wind turbine appears to be a simple process, unless one understands the underlining mechanisms behind what is occurring. Given a small number of inputs, such as maximum radius, rated power and nominal wind speed, major design features like number of blades, pitch angle, and angular velocity can all be determined. This design began with evaluating the major design features just mentioned using the blade element momentum theory (BEMT). In this thesis, we focused on a nominal case for the ventilation exhaust energy recovery industry: the parameters given were a wind speed of 25 miles per hour (which corresponds to about 11.2 meters per second), and an exhaust outlet of 4 feet by 4 feet square. This is all that was needed to begin a basic design, however one major assumption was made; the range of angular velocity desired. The first iteration focused on the goal of maintaining a range centered near 500 rotations per minute. This provided a TSR of about 3−4 and represented a common starting point for a high efficiency but low mechanical complexity design, with low bearing velocity and vibration requirements on shaft and support. To obtain the desired high efficiency, a large number of blades was required to reduce the overall rotational speed. The initial design parameters that resulted were a 10 bladed turbine with a high efficiency and a low rotational speed. With this information, the data was input into Harp−Opt, which is a software code developed by a lab member, Daniel Sale, and available from the National Renewable Energy Lab repository of wind and water power codes. The desired goals for which Harp Opt was utilized in this project were twist and chord information. With the new optimum twist and chord values, WT_Perf was again utilized to re−evaluate optimums of blade pitch, rpms, and tip speed ratio.

For the first run of the optimization process, a generic airfoil was used. Once the blade design parameters had been outlined, the next step was to research different airfoils to fine tune the design for a high lift airfoil, and see if the change in shape could result in higher efficiency. Because of the wide variety of airfoil types and the specific file format needed in both WT_Perf and Harp−Opt, it is neither efficient nor wise to try to pick an airfoil geometry by running through hundreds of geometries in these programs. With the simplifications of constant speed and constant direction, extreme airfoil geometries could be evaluated because there is no need to have high coefficients of lift over a wide range of angles of attack. Instead, only the peak value was important, even if the range of that peak value was narrow.

Airfoil Selection

After the initial test runs with simple airfoils, the design process lead to a search for an optimum airfoil for high efficiency, structural strength, and manufacturability. The two primary criteria for airfoil selection was high lift coefficient and high lift to drag ratio. The University of Illinois Urbana-Champaign has an extensive airfoil database that includes airfoil geometry, extensive testing data and information on airfoil usage. Of particular interest to this thesis is the information covered in the 5 volumes of low speed airfoil tests for model aircraft, unmanned aerial vehicles, and small wind turbines. These tests were conducted at Reynolds Numbers between

100,000 and 500,000 (the Reynolds number based on the average chord length for our turbine is 250,000). Volume 3 had the most useful information to determine optimum airfoil candidates for this application. Figure 3.1 is the list of airfoils tested from this volume:

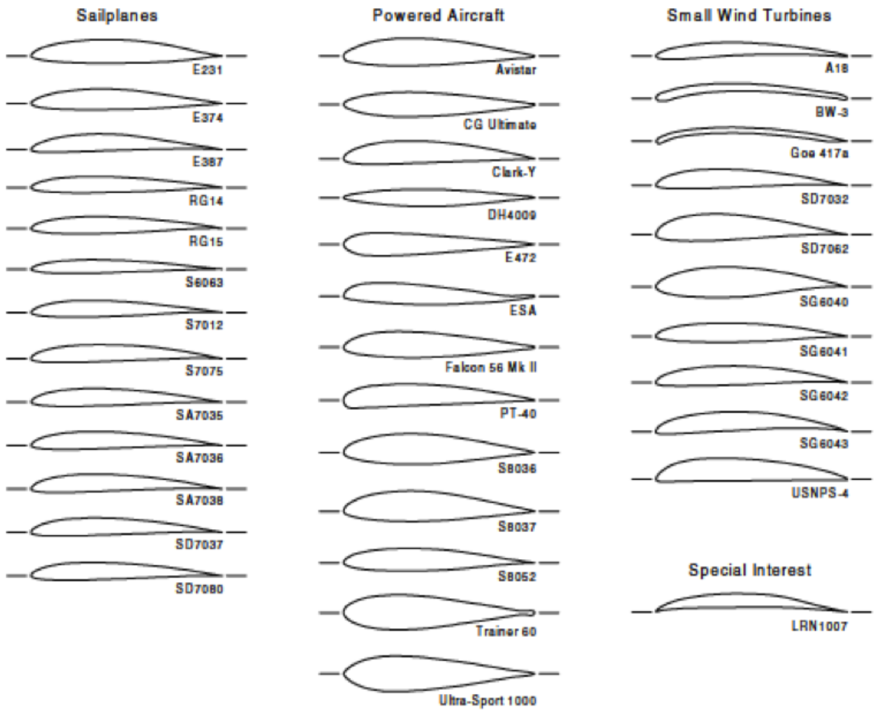

Figure 3.1: Low−Speed Airfoil Designs [?]

Powered aircraft foils were not considered because of the fundamental difference in the nature of the intended operation. Both Sailplanes and small wind turbine airfoils were considered. Looking for the airfoils that had the highest peak coefficient of lift further narrowed the list. Each airfoil had data in the following form: Figure 3.2 shows the coefficient of lift versus the coefficient of drag and the

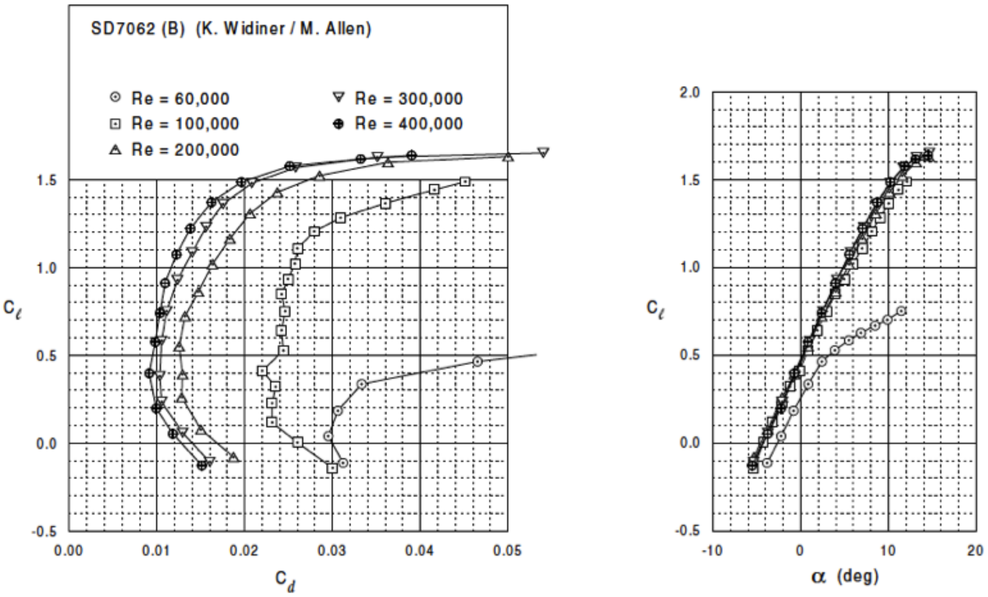

Figure 3.2: Lift Versus Drag and Lift Versus AoA [?]

coefficient of lift versus the angle of attack for the SD7062, a typical example of airfoil considered in the design. Table 3.1 compiles a list of the top airfoils considered and their original applications:

Searching through Figure 3.1, the list of airfoil considered initially in the design, BW−3 had a high coefficient of lift, but was one of the thinnest airfoils in any of the studies, so even with the dramatic camber, maintaining a stiff blade would be difficult, given the theoretical chord lengths that were being considered (less than an inch near the tip). The top three airfoils selected were the SD7062, SG6043, and the USNPS−4. SD7062 initially had the best overall characteristics. Though the USNPS−4 does have the highest lift to drag ratio, it overall has higher drag through the entire range of lift coefficients, which was noted in the report. Before moving

Table 3.1: Airfoil Decision Matrix

Airfoil	Thick (%)	Camber (%)	Max Lift	Lift/Drag	Max Re	Original Purpose
A18	7.26	3.84	1.22	32.97	300,000	Small Wind Turbine
E-387	9.06	3.90	1.28	44.14	460,000	Sailplane
SD 7032	9.95	3.66	1.26	29.65	300,000	Small Wind Turbine
SD7037 (D)	9.20	3.02	1.28	49.23	300,000	Small Wind Turbine / RC Soaring Competition
SD7037 (E)	9.20	3.02	1.35	32.93	300,000	Sensitive to small changes
SD7062	13.98	3.97	1.60	41.03	400,000	Small Wind Turbine / Keep Relatively Clean
SG 6041	10.00	2.00	1.35	38.57	500,000	Small Wind Turbine / Design to Max L/D
SG 6042	10.00	3.80	1.49	35.48	500,000	Small Wind Turbine / Design to Max L/D
SG 6043	10.00	5.50	1.62	39.51	500,000	Small Wind Turbine / Design to Max L/D
USNPS-4	11.94	5.00	1.60	47.06	400,000	Similar range to SD 7062 but with much higher overall drag
BW-3	5.02	5.65	1.40	26.67	400,000	Small Wind Turbine / Designed to be extrudable

forward one other factor was considered which was the effect of blade cleanliness on the overall performance.

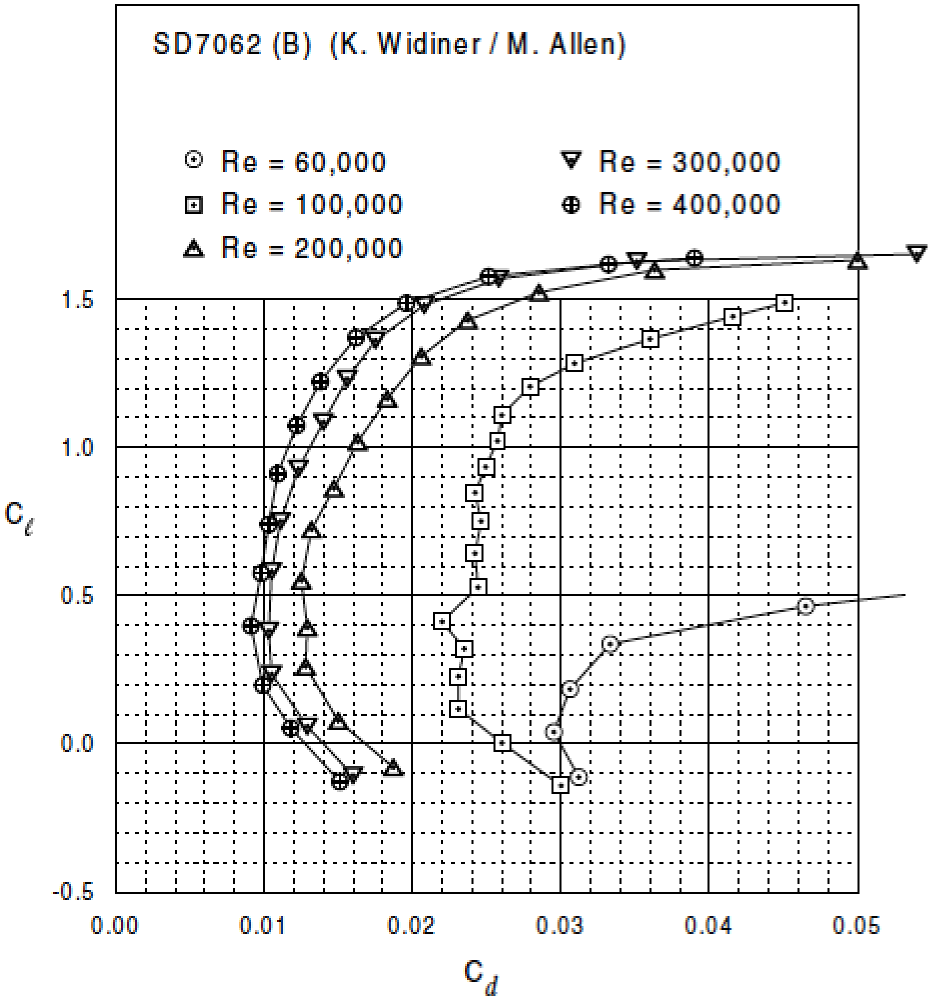

Figure 3.3: SD7062 Lift and Drag Characteristics for a Clean Blade [?]

Experiments had been conducted, and reported in the same UIUC database [?], to simulate dirty−blade conditions. The two above figure represent the effects of a

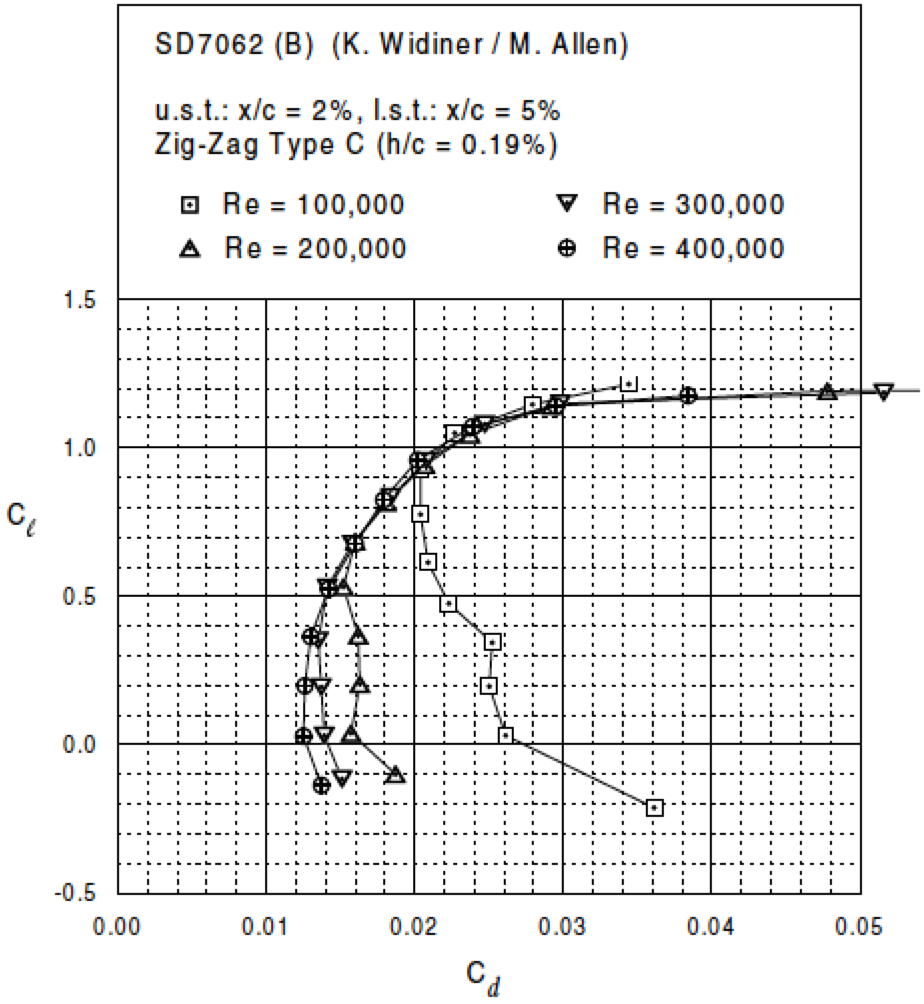

Figure 3.4: SD7062 Lift and Drag Characteristics with Fixed Transition [?]

dirty blade on the SD7062. Notice that (as noted in the report): “The fixed transition cases used to simulate dirty−blade conditions not only caused severe drag penalties but also decreased $C_{l,max}$. At Re = 100,000, the $C_{l,max}$ was reduced from 1.52 to 1.22 (a 19.7% decrease), and for Re = 400,000, the $C_{l,max}$ was reduced from 1.68 to 1.19 (a 29.2% decrease)”[?]. Since our free stream velocity source is an exhaust fan, the potential for the blade to ‘get dirty’ is very high, so therefore this blade must be discarded in favor of a blade that is less affected by adhered particles.

Roughness in the composite layup manufacturing process was also considered a source of uncertainty in the aerodynamic performance of this airfoil. The possibility of adding a polishing step to the manufacturing process was discarded as unnecessary expense, complication in logistics and source of variability in the final rotor shape. Though the USNPS−4 had not been tested under simulated dirty blade conditions, it was noted that due to similar characteristics to the SD7062, it would likely have the same difficulty with surface roughness from particle adherence.

Unlike the SD7062 and the USNPS−4 airfoils, the SG6043 exhibited significantly less degradation under dirty blade conditions. At Re = 300,000, $C_{l,max}$ was reduced from 1.6 to 1.4 (a 12.5% decrease). It is worth of note that the higher the max C_l the more significant the effect the dirty blade condition had on the overall performance characteristics.

Once the SG−6043 airfoil selection was made, the C_l and C_d data from the experiments were input into WT−Perf, the Blade−Element−Momentum design code created by NREL for wind turbine aerodynamics. Selecting a fixed wind speed and direction, as is characteristic of the exhaust energy recovery application, rather than a distribution of wind conditions, the data shown in Figures 3.8 and 3.9 was computed.

For the initial prototype construction, structural integrity and stiffness of the blade was a concern, even at 10% thickness. Therefore, another airfoil was needed to perform testing with the prototype. Until the manufacturing process was selected and fine−tuned, a thicker (15%of chord length) airfoil was used to design the rotor blades, in order to ensure that the first prototype would be structurally sound and the aerodynamic characterization would not be detrimentally affected by large

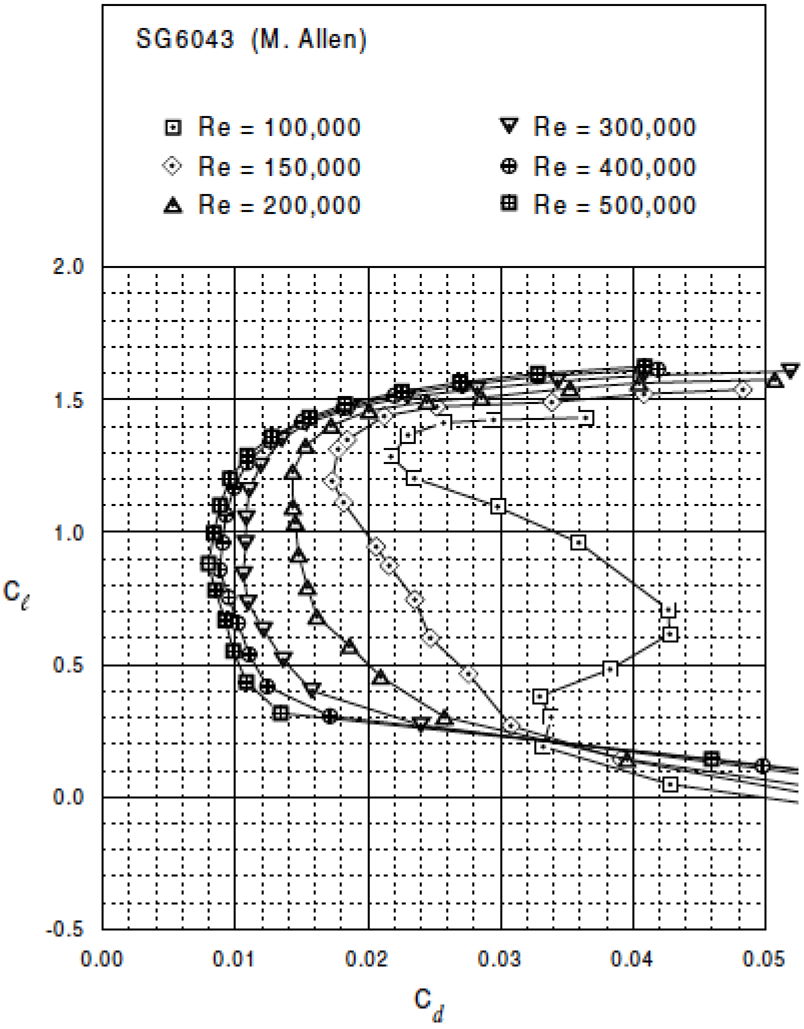

Figure 3.5: SG6043 Lift and Drag Characteristics for a Clean Blade [?]

deformations of the rotor that would mask the true performance, as predicted by the BEM design code (WT−Perf).

Information from this first built prototype would be used in the design and testing procedure, if it was determined that a thinner and more efficient airfoil design was

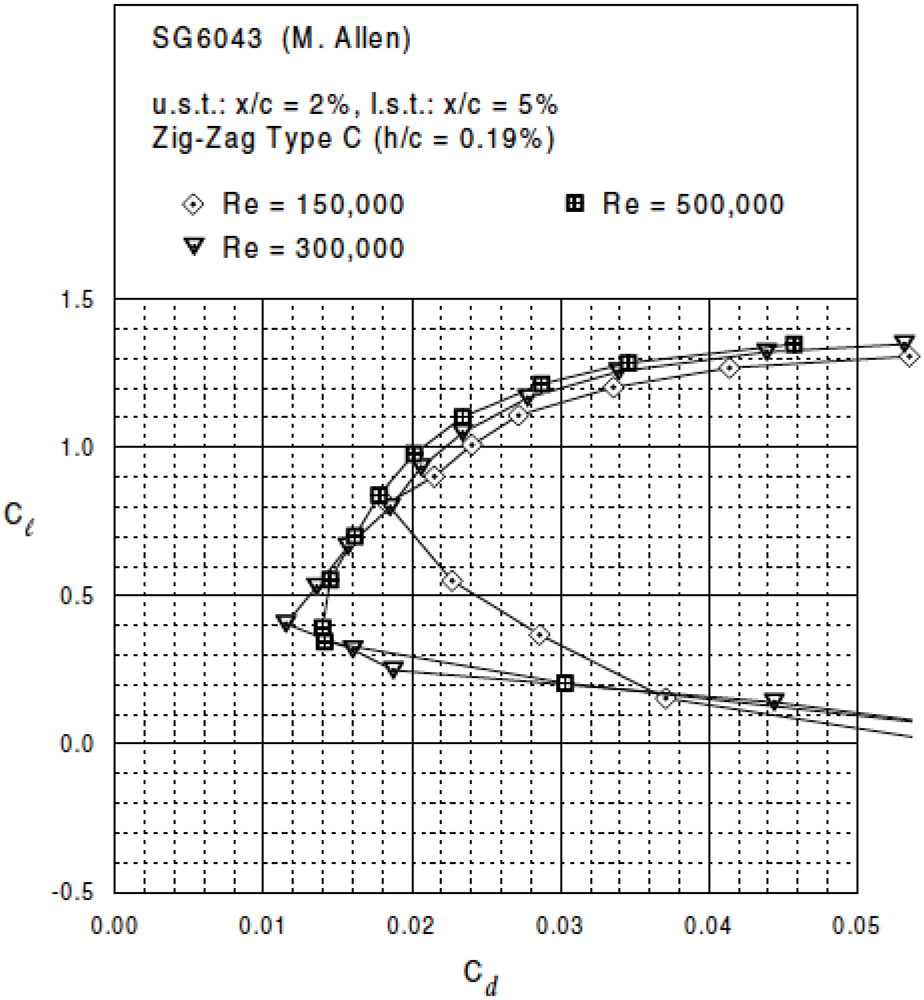

Figure 3.6: SG6043 Lift and Drag Characteristics with Fixed Transition [**?**]

achievable using the compression-molded dry lay−up composite manufacturing technique. The NACA 4415 was chosen as an ideal candidate for this first, structurally robust, prototype blade airfoil.

The performance characteristics of the rotor using the NACA 4415 airfoil, as

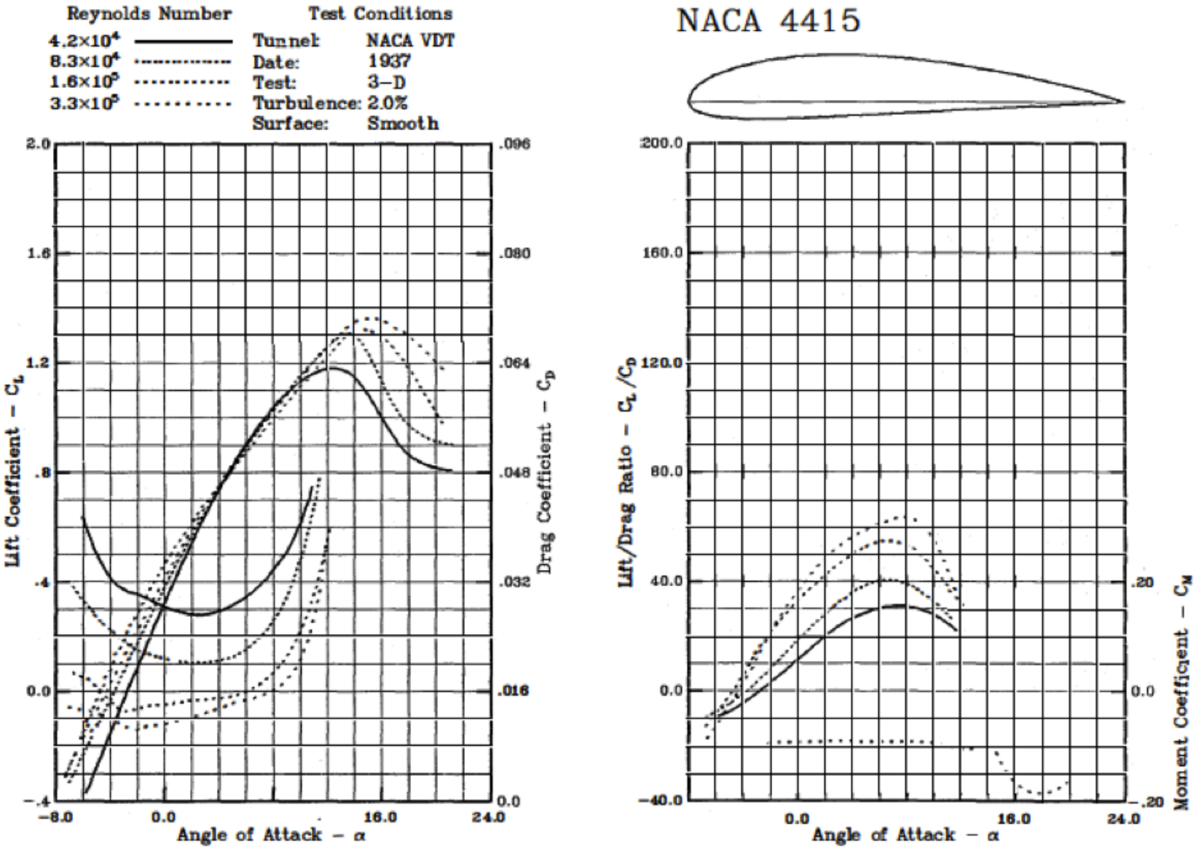

Figure 3.7: Lift v AoA & Lift to Drag Ratio Versus AoA

predicted by the design code, WT−Perf, are shown in Figures 3.12 and 3.13. Figure 3.11 presents the comparison between the performances of the two rotors based on the preferred airfoils. We can see that the efficiency penalty in using the thicker NACA airfoil compared to the high lift−to−drag SG airfoil is minimal. The shape of the blades is compared in Figure ??.

The lift to drag ratio for the SG6043 airfoil is slightly higher than the NACA 4415 at Re = 2E6, but the added thickness of the 4415 airfoil will give us greater strength

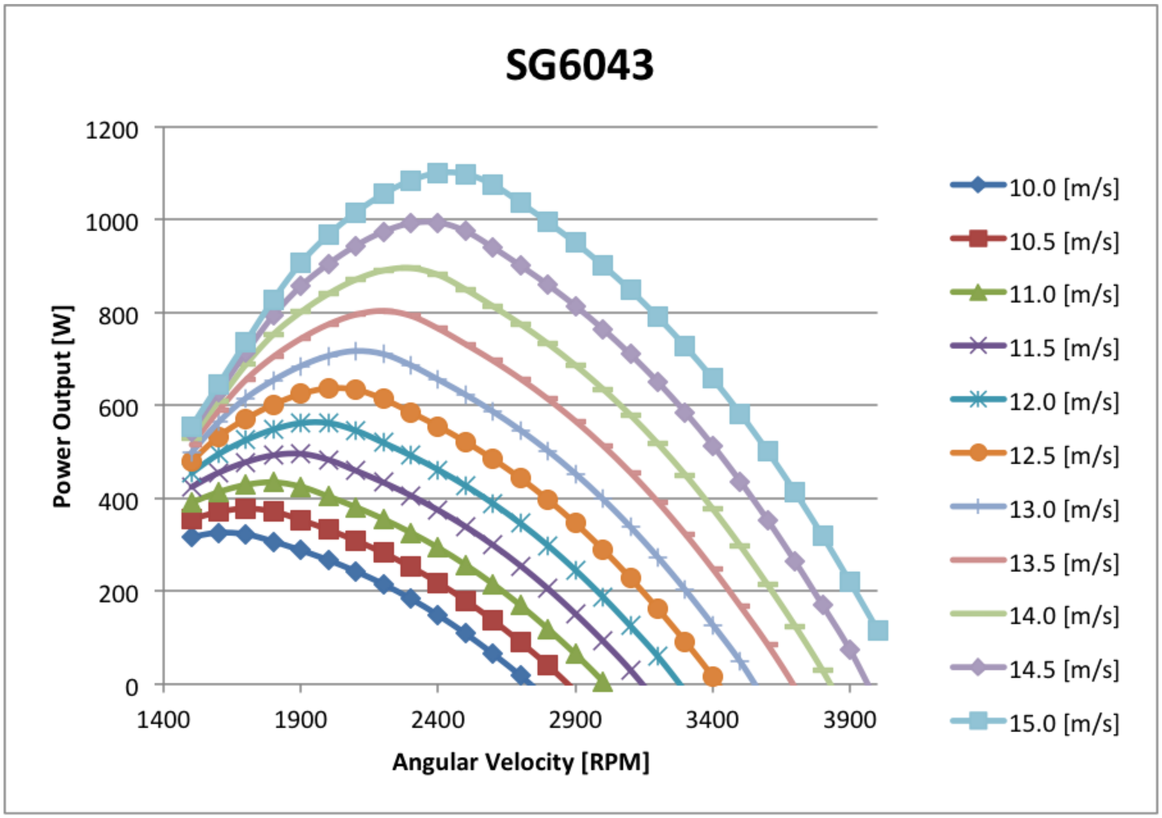

Figure 3.8: SG6043 Power v. Angular Velocity for a Range of Wind Speeds

needed to maintain the optimum geometry. The above initial comparison was based on dissimilar Reynolds Number data and therefore is not the best representation of the performance of the NACA 4415 at the expected operating condition. Based on catalogue by [**?**] of low Reynolds number airfoil data for wind turbine applications (pgs. 450-463), another analysis was conducted to include the second NACA 4415 with a lower Reynolds number that on par with the local Reynolds Number of the final design that was discussed earlier.

The airfoils selected with this criterion were run through WT_Perf to determine

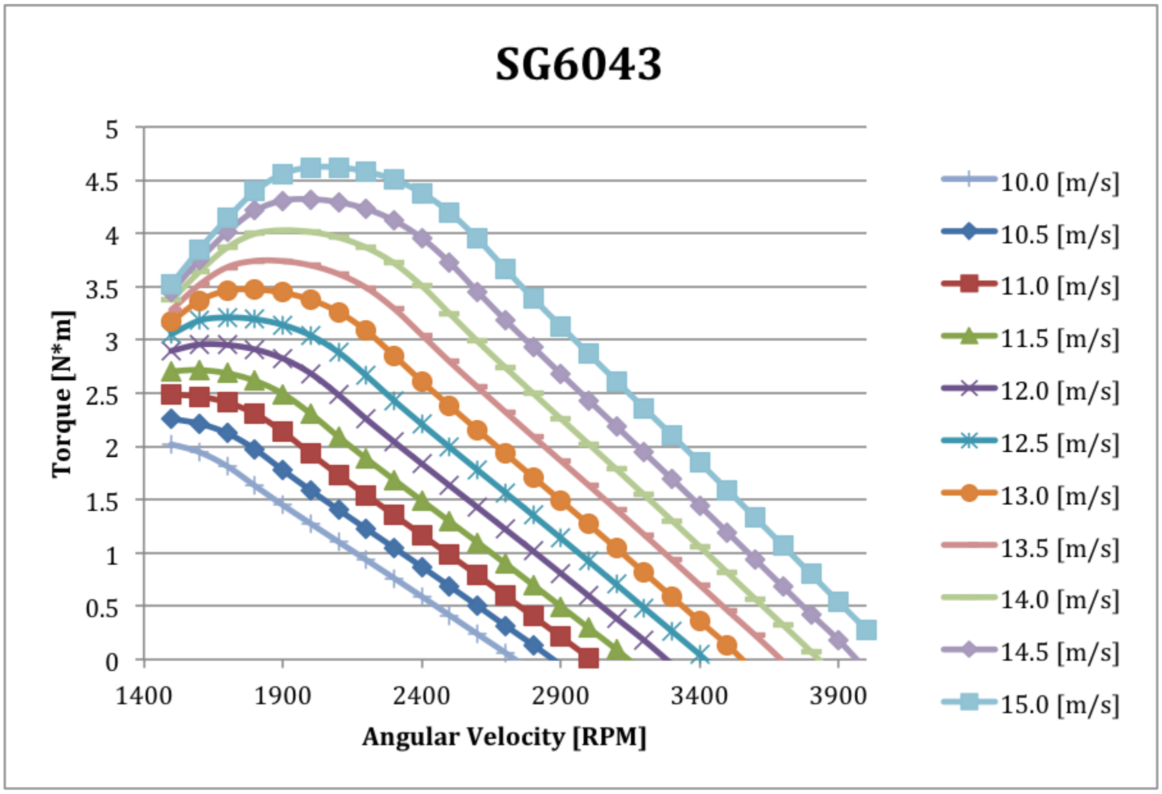

Figure 3.9: SG6043 Torque v. Angular Velocity for a Range of Wind Speeds

which airfoil would perform best with our given conditions. For the given angular velocity range, the SG604−series showed the best lift coefficients in comparison with drag while maintaining that lift well in rough surface conditions, proving to be the ideal airfoil theoretically for our application. A close runner up was the NACA 4415, which, being thicker than the SG6043, would be a good consideration if blade stiffness became a concern. With a definite airfoil geometry the next step was to determine the final chord and twist values.

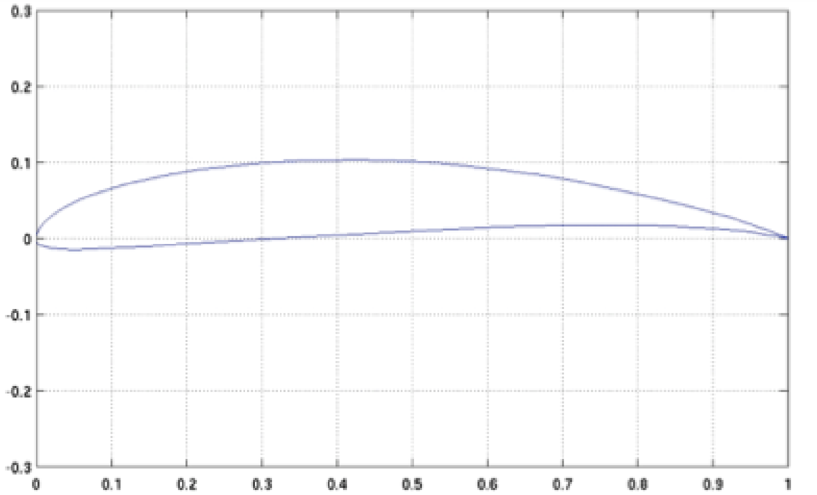

(a) SG6043

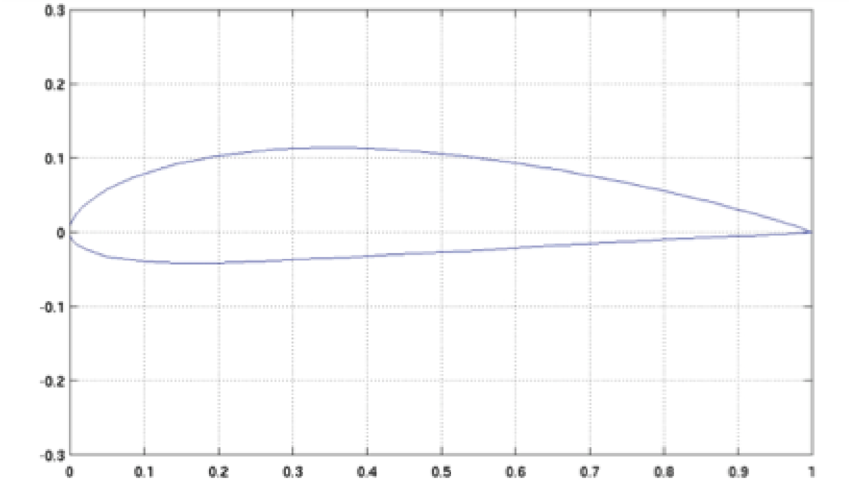

(b) NACA4415

Figure 3.10: Airfoil Comparison

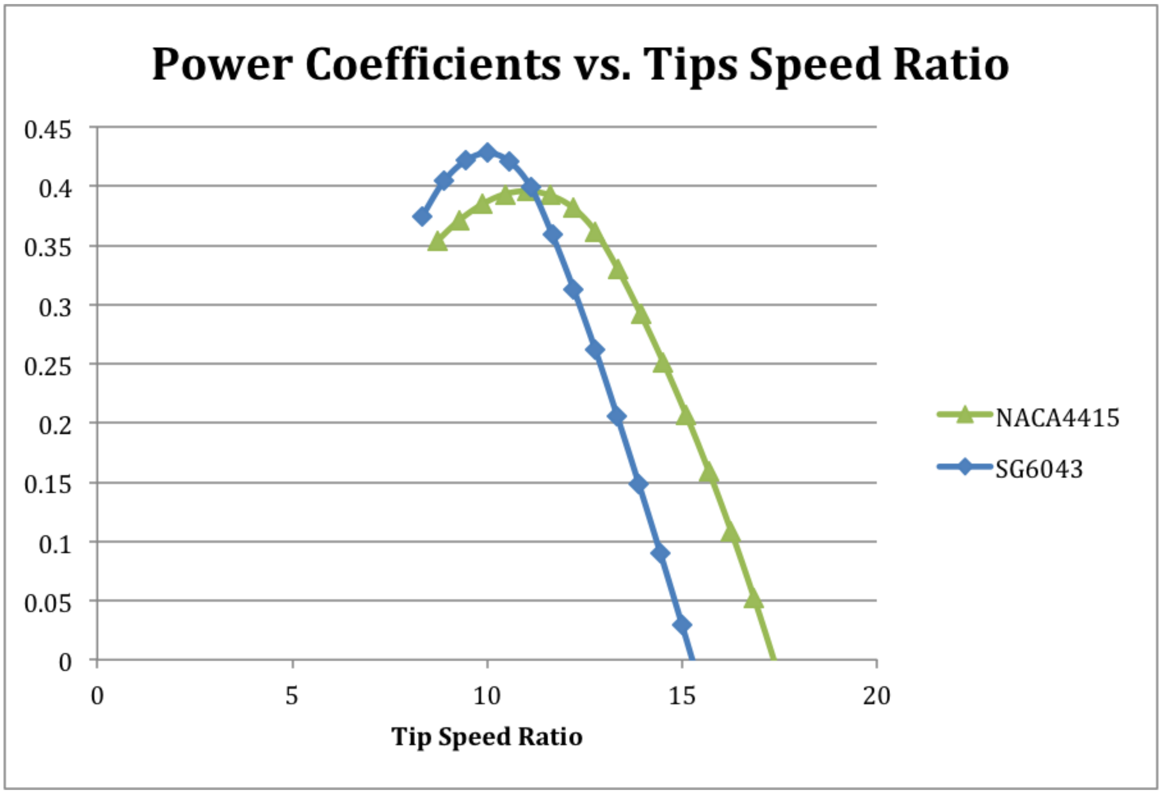

Figure 3.11: SG6043 & NACA4415 Coefficient of Performance v. Tip Speed Ratio

Basic Design Change

When considering a complete system for power generation, all the components must be well matched for the product to be successful as a whole. At this point a major change in the design parameters was made in order to ensure that the rotor would couple well with the electrical generator. Instead of an angular velocity range centered around 500 rpms, the new goal was to operate at an angular velocity as high as possible, up to an order of magnitude higher than originally assumed. The cost of the generator winding is inversely proportional to its frequency and the

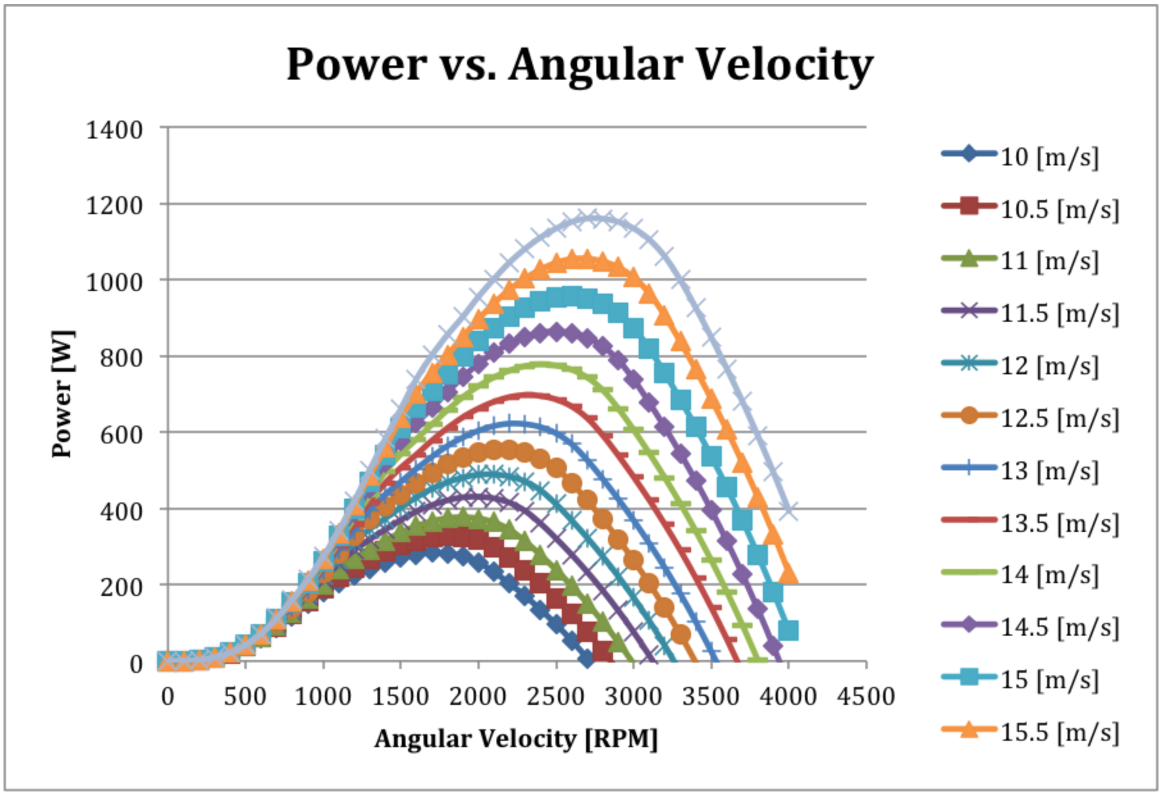

Figure 3.12: NACA4415 Power v. Angular Velocity for a Range of Wind Speeds

number of poles is limited in a small diameter generator. Therefore, increasing the rpm of operation of the rotor was determined as a low−cost, low complexity way of lowering the cost of the generator which a cost driver in this technology. Though 5000 rpms were considered optimal, the efficiency of a 2−foot radius blade operating in 25−35 mph wind limited the upper limit to about 3000 rpms or less. At this operating conditions, the Tip Speed Ratio is already much higher than commonly used in wind turbines, in the range 8−12. The twist angle along the blade has to change dramatically from root to tip between relatively high values, both negative and positive, to maintain angles of attack that provide high lift for all sections of

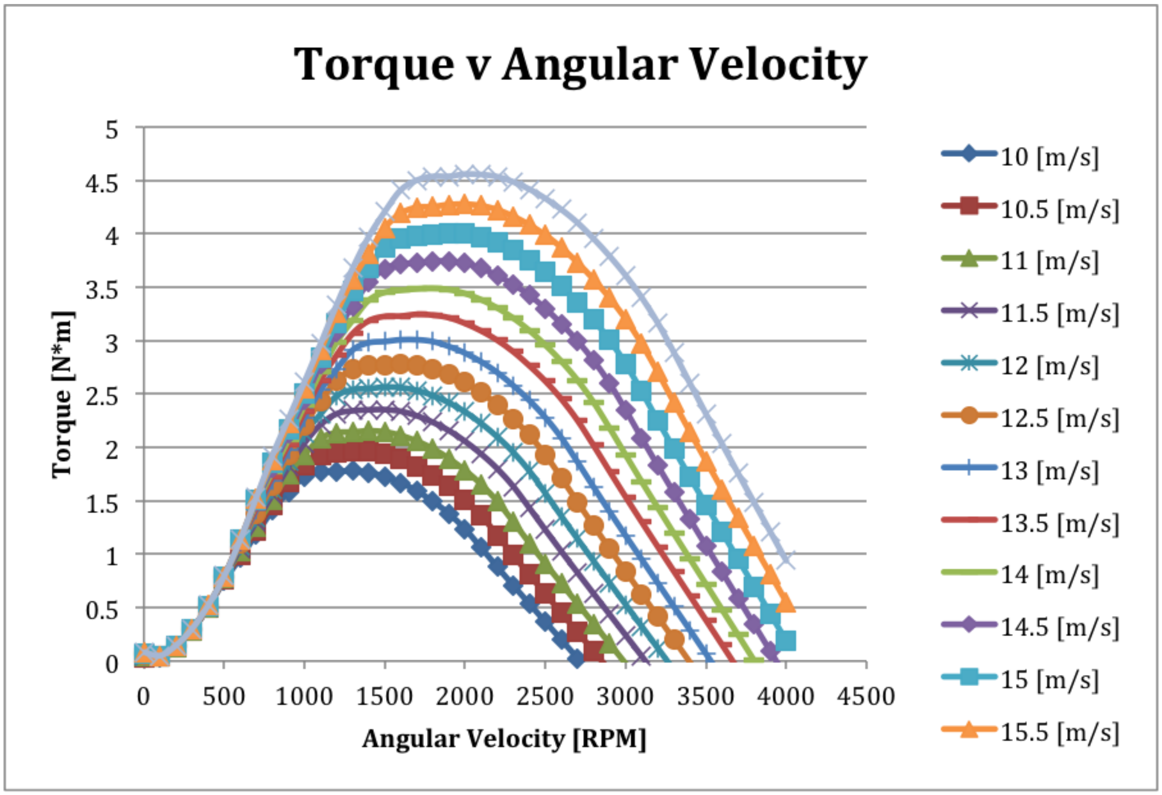

Figure 3.13: NACA4415 Torque v. Angular Velocity for a Range of Wind Speeds

the blade. This is a very challenging environment for design, and one that deviates significantly from the literature on wind turbine design.

The first change was to reduce the number of blades. With a large number of blades and a high angular velocity, the turbine would appear to the flow as a wall and the flow would tend to go around the obstruction instead of through the turbine to produce lift. Another major consideration for any motor or generator is the bearing design. A well–designed, well–balanced rotor allows for simpler bearings to be used. An odd number blades, specifically in a rotor design with fewer blades can lead to asymmetrical loading on bearings, which would require bearings that could

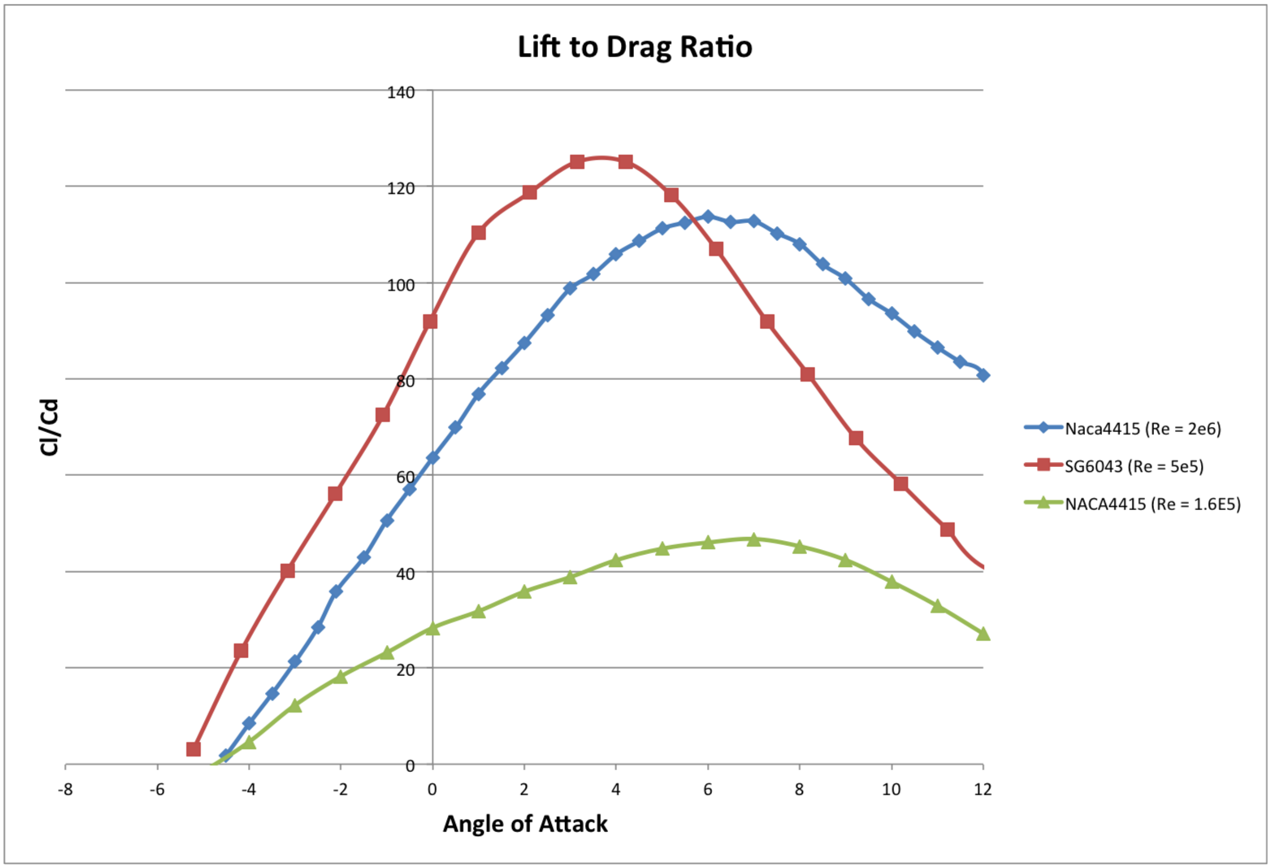

Figure 3.14: Ratio of Lift to Drag Versus Tip Speed Ratio

withstand that kind of loading. Six, four, and two bladed turbines were considered for the higher rotational speed design. The two-bladed design was found optimum because it allowed for a reasonable chord distribution (and a corresponding thickness distribution on the blade that was manufacturable and provided a certain level of required stiffness), even at the low solidity ratio required for high Tip Speed Ratio operation. Additionally, its symmetrical load distribution during rotation was beneficial for the long life, low maintenance requirements of this energy conversion device. Quick Return−On−Investment is critical for the financial success of any energy conversion system, particularly for a system that needs to be retrofitted into existing buildings.

Harp-opt was then utilized with the goal of maximizing efficiency for a given wind speed. Unexpectedly, the generator−driven increase in angular velocity lead not only to fewer number of blades, but also to reduced solidity of the individual blade geometry. Below is a comparison of the 10−bladed, low speed design, and the 2−bladed, high−speed design. The difference in solidity is clearly visible in the

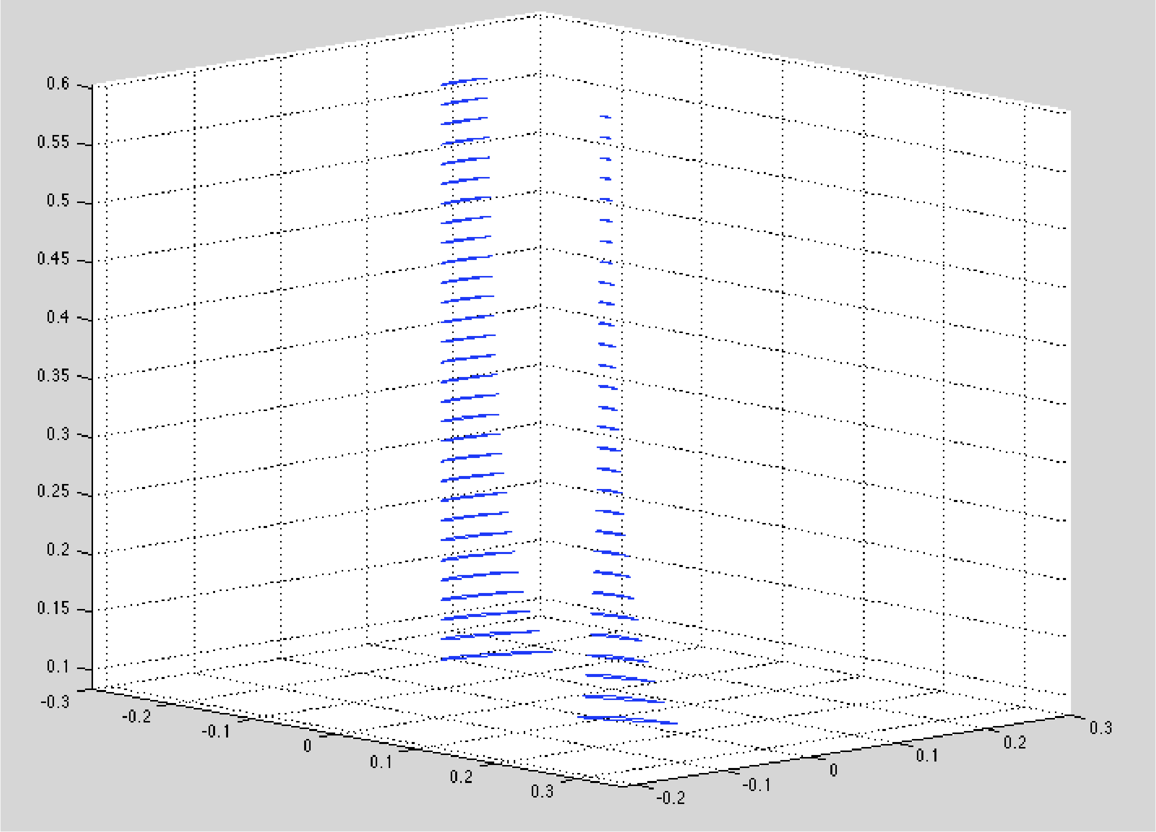

Figure 3.15: Solidity Comparison of Two Designs

side-by-side comparison of the blade designs. Solidity ratio, defined earlier, has a significant influence on the airfoil chord lengths because it is part of the formulation of the both the longitudinal and transverse axial induction factors equations (1.16). Although reasonable efficiency can still be attained at higher solidity ratios, in our case the low solidity result was desirable for two reasons. First, lower backpressure is a feature of low solidity ratio. In commercial scale wind generation, backpressure is not a primary consideration because upstream propagation of that pressure has no negative effects. In this case, because the source of free stream velocity is an exhaust fan in a building, backpressure is an important factor. If that pressure propagates upstream and effects the operation of the exhaust fan, then the value added in energy savings will partially be spent by the exhaust fan and ultimately will be lost in the increased load experienced by the fan. Secondarily, having a low solidity ratio allowed for a higher rotational speed, which is optimal for direct coupling with the generator. The output from Harp−Opt is presented in Figure 3.16.

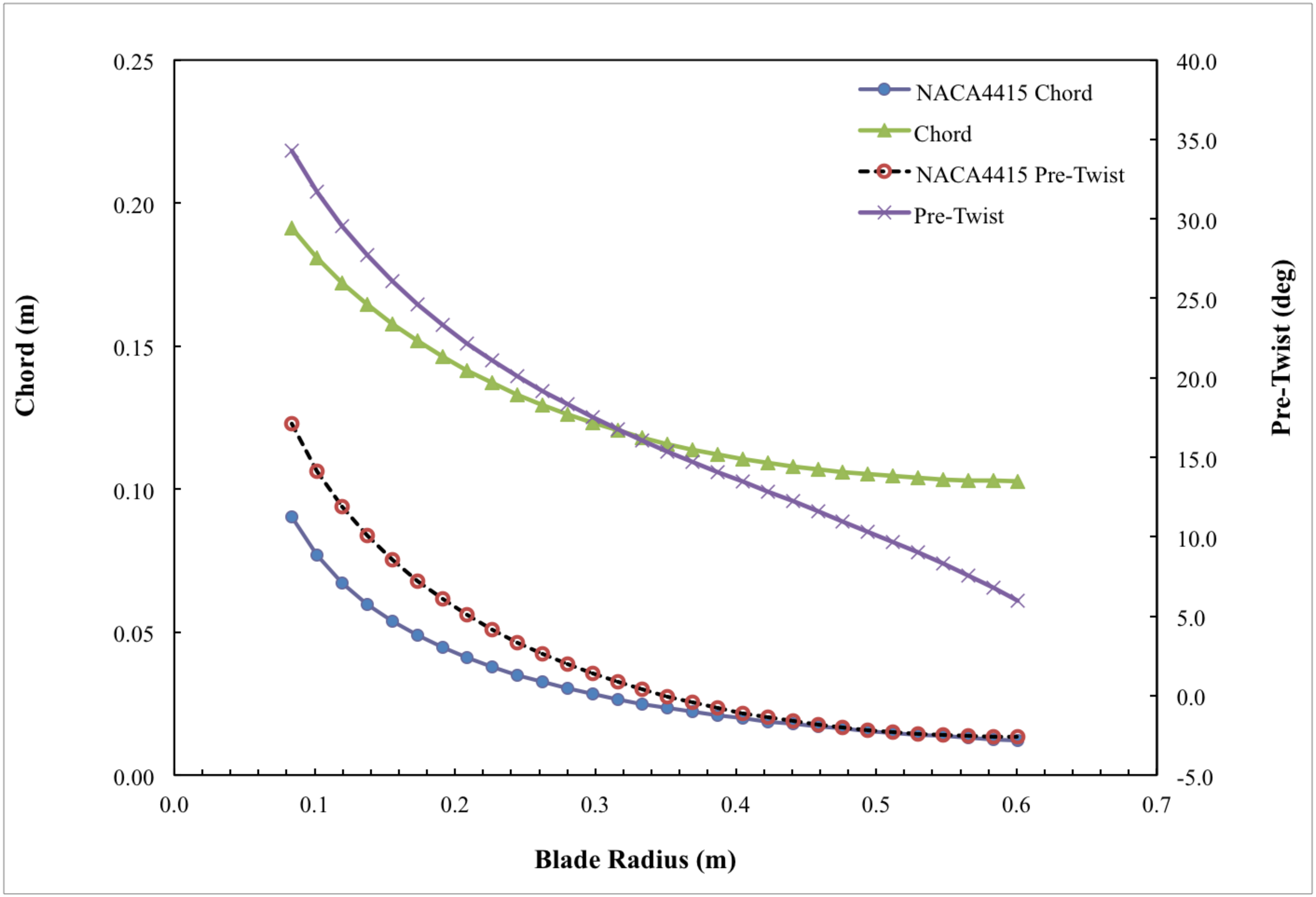

Figure 3.16: Comparison of Low Angular Velocity Blade Design v High Angular Velocity Blade Design

At this stage we were ready to build and test a prototype. In order to convert this theoretical geometry optimized with Harp−Opt into a three−dimensional CAD model, the two-dimensional airfoil geometry was scaled by the chord length and rotated by the twist that was determined at each of the 30 sections in MATLAB. Initially, in both the first and second prototypes, the airfoil sections were aligned along the leading edge of each airfoil. The location chosen to apply predeflection was the quarterchord of each airfoil. In order to make the blade more structurally sound, in addition to the predeflection, the airfoil sections were align along the quarterchord line and the final pre−twist was applied about the same line. An example of the scaled and rotated sections can be seen in Figure 3.17.

Then those sections were converted in their x,y,z coordinates and imported as curves into SolidWorks. All thirty sections were used in a lofting feature to recreate the blade as an actual solid object. Figure 3.18 is an example of the completed Prototype 1.0 3−D model.

A hub design was created based on the mechanical connection with the electrical generator and the two blades were merged to form a single body that did not require any fastening hardware and could be manufactured in one piece, as shown in Figure 3.18.

Before the experimental testing of the first prototype, we performed higher fidelity modeling in order to more accurately predict power output and to determine how much backpressure would be produced. A domain was created in Gambit that included the jet expansion volume. The purpose of the jet expansion volume was to ensure that the exhaust outlet expanded as is theoretically predicted and was not hampered by the mesh. In place of a physical blade geometry a disk is created for use by the virtual blade model (VBM). A computational fluid dynamics software was used to calculate torque, power, efficiency, and backpressure (which is not able

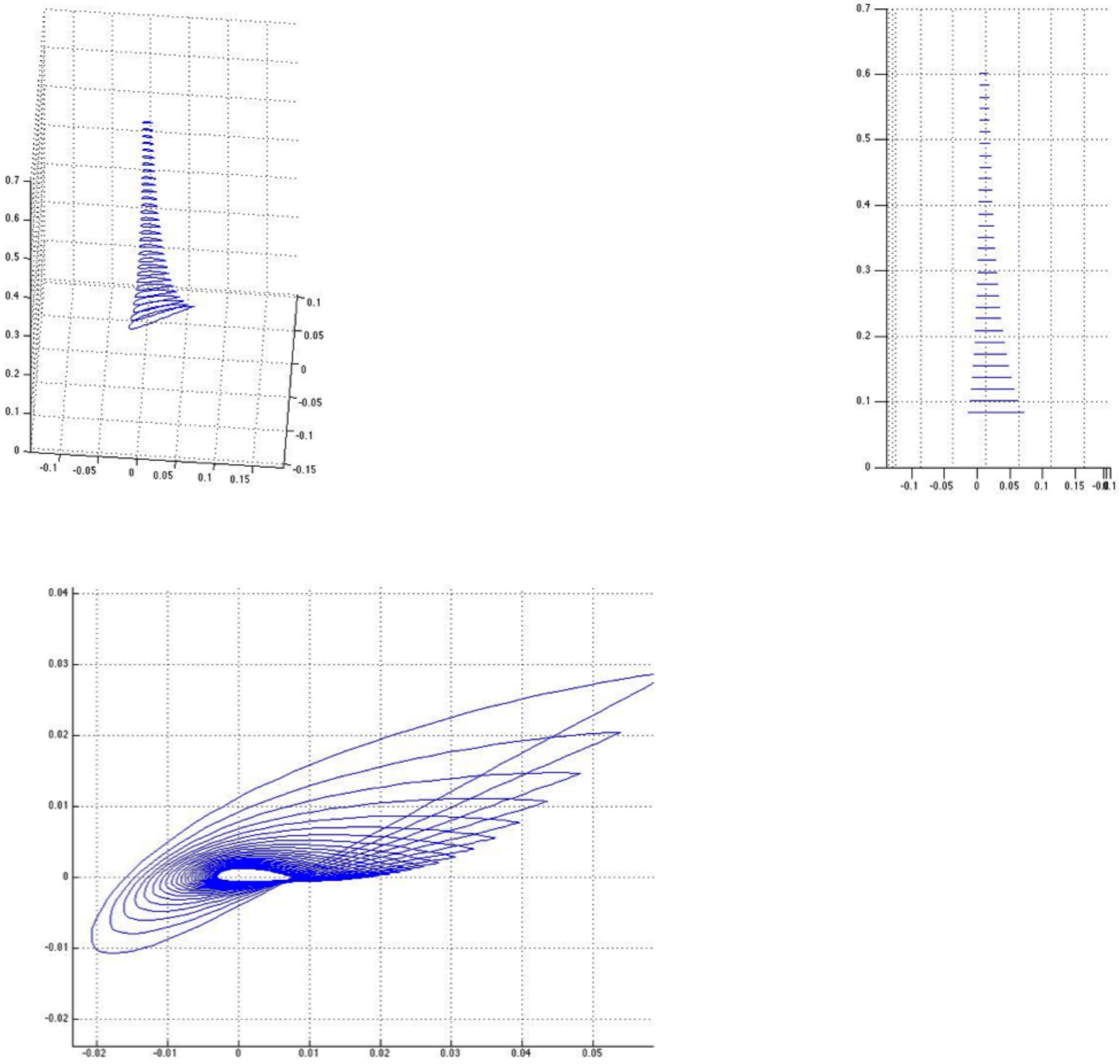

Figure 3.17: Prototype 2.0 Blade Design (without predeflection)

Figure 3.18: 3−D CAD Model of Prototype 1

to be determined theoretically or from the Blade Element Theory WT-Perf computations) of the design in a much more realistic setting. This domain includes the proximity of the floor on the roof, which would present a no slip boundary relatively near the turbine rotor, hindering entrainment and the fact that the turbine is not in an infinite fluid with uniform speed, but instead is in front of a turbulent jet with a finite cross-section. Predicting overall power output and backpressure are essential in determining if this project is marketable. The last piece of the puzzle is experimental data to complete to design research and make recommendations for improvement.

3.2 Solid Modeling and Manufacturing

The original material and manufacturing process selected for the blade was a fiber-resin composite using a vacuum-bag production process. Vacuum-bag composite manufacturing is a cheap, simple, and fast way to build individual parts to be used for prototypes that have complex shapes. As the design developed and stiffness became a concern, the ability of the vacuum bag process to produce an exceptionally stiff part was unclear. Due to the blade small thickness, particularly near the tips, the moment of inertia to both bending and torsion was insufficient to prevent significant twisting or deflection.

The high rotational velocity required to match the generator frequency for low cost and high efficiency created a change in the fundamental concept for the blade design and the logic behind the planning of how the product would be manufactured. Initially the plan was to make multiple high solidity blades, with the same design, and affix them to a central hub to produce the turbine rotor. Figure 3.19 is a conceptual design for the multiple blade units rotor paradigm.

Figure 3.19: Individually Manufactured Blade Conceptual Design

The aerodynamic requirements of a high efficiency rotor at very high rotational speed, the operational tip speed ratio was set to 10-11 in an effort to maximize generator frequency in direct drive with the rotor shaft without jeopardizing efficiency, imposed a very low solidity ratio for the rotor. This meant a complete redesign of the rotor and of the individual blades, that became much more “svelte” with a rapidly decreasing chord length along the span. Thus, the optimum design became a two bladed turbine, with very thin and slim blades. An early CAD model of the two-bladed rotor, with the two blades broken off from the central hub, can be seen in Figure 3.20. The final rotor design involved a single part that encompassed all three elements. The hub nosecone is also shown for completion. This part was manufactured in foam from an aluminum mold designed as part of this thesis. It was based on a 4:1 length-to-diameter ratio paraboloid.

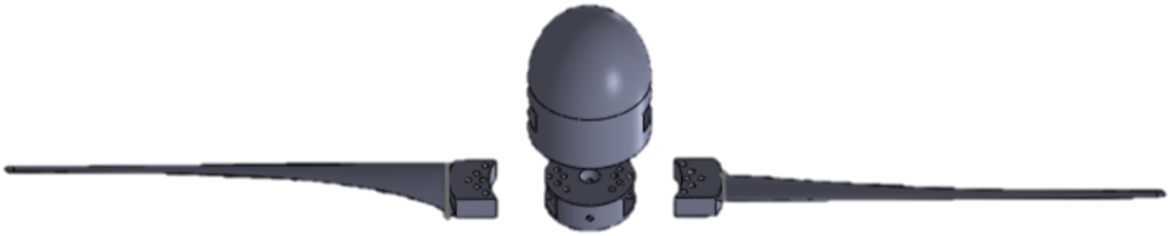

Figure 3.20: Conceptual Hub,Blade & Nose Cone Assembly

This presented a new opportunity for manufacturing the rotor as a single part, with significant improvements in the structural properties of the blade and reduced cost: Dry lay-up, compression molding is a popular choice for manufacturing in composite materials for complex parts that involve a large aspect ratio. For example, composite skateboards, snowboards, skis, and even specialty car parts are frequently made using the compression molding process with dry composite lay-ups. Compression molding is a process where the desired shape is cut into a mold, the fiber is laid up in one of the mold halves, the mold in infused with resin, closed, heated, and pressed with on a high pressure (10,000 psi) hydraulic press. The below figure is a picture of the lay-up and mold for the prototype 1.0 design.

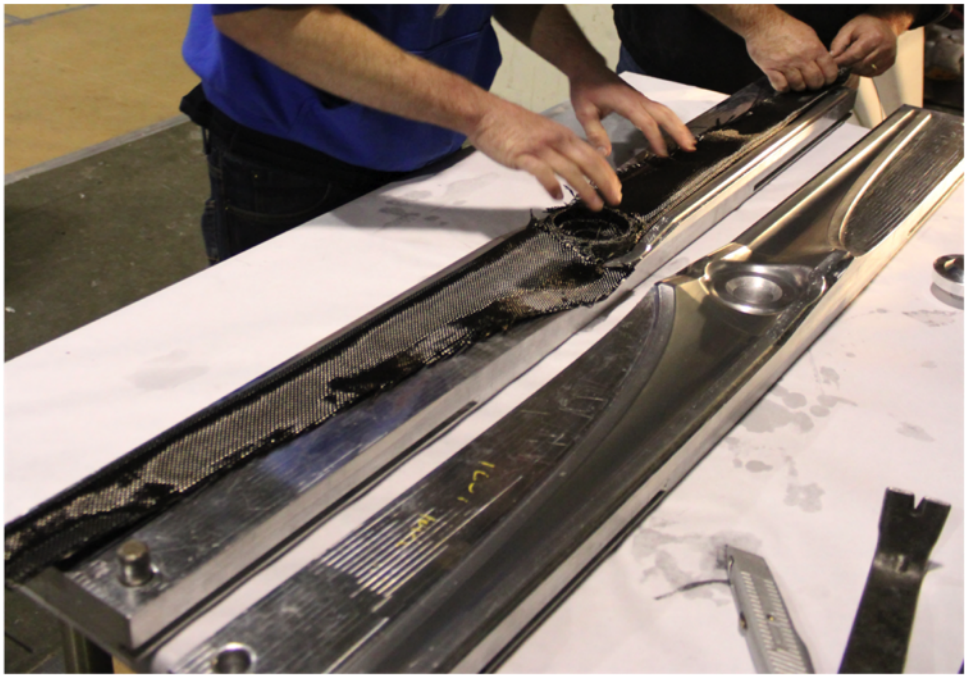

Figure 3.21: Prototype 1.0 Rotor During Lay-up Process

This type of manufacturing process is well suited for a linear part that does not require a large planform area and large volume mold. The two-bladed rotor is a long, slim, part only about 3 inches at its widest part, and 48 inches in length, that can be molded including the hub in one piece. Three or more blades would require a much larger and much more expensive mold or require that blades be made individually and fastened to the mold, which leads to complicating factors like assembly costs, additional parts, and additional wear concerns. Fiberglass and carbon-fiber were considered as potential choices for the fiber material in the composite. The relatively small amount of material used for the part tilted the decision in favor of carbon as the additional cost for the carbon-fiber was negligible in comparison to the multiple benefits that carbon offers, including increased mechanical strength, enhanced stiffness, higher resistance to wear, and less absorption of humidity.

The rotor has a core throughout that provides a torsion box and strength particularly in the hub and near hub region. Fiber direction and layered combination of fiber matting is another way to directionally resist bending and torsional moments. The blade was found to be very stiff torsionally from the first prototype, but multiple iterations with different lay-ups were required in order to increase bending stiffness to an acceptable amount before wind tunnel testing.

Chapter 4

EXPERIMENTATION RESULTS AND DESIGN MODIFICATION

4.1 Prototype 1 Experiment

Multiple experiments have been conducted on the performance and structural integrity of the composite rotors designed and manufactured for this thesis. Initial experiments were conducted at the University of Washington Aerodynamics Laboratory. The wind tunnel housed in this laboratory was designed for much smaller prototype testing with a 3 foot by 3 foot square test section. However, because this is an open return tunnel, the exhaust end provides a near realistic environment to test the rotor blades in. The first experimental set−up consisted of the rotor mounted onto a 7/8 inch shaft held by two bearings on an aluminum structure. An assembly of a torque cell, optical encoder, and variable friction brake was attached to the back end of the shaft. The axis of the set−up was aligned with the axis of the wind tunnel. The diameter of the wind tunnel at the outlet is 61 inches, which is larger than the initial design parameter of 4 foot by 4 foot square outlet. A view of the setup, with the exhaust end of the wind tunnel on the left side of the image and the flow coming from left to right onto the black rotor in the center of the image, can be seen in Figure 4.1.

The encoder and torque data were recorded via LabView and used to calculate power output. The brake was manually controlled via a potentiometer. The first observation from the experiments was that prototype 1.0 did not self−start. Even after multiple attempts to reduce friction in the experimental set−up, the blade

Figure 4.1: Prototype 1 Experimental Set-up

would not turn or accelerate to operating speeds without a starter bringing the blade up to about 1200 rotations per minute. With the extreme blade geometry and the goal of maximizing angular velocity, the designed twist resulted in blade section orientation primarily in the direction of rotation. The root section was only 17.5 degrees away from the direction of rotation.

Once the system was accelerated to rotational operating speeds, the blade performed well and produced significant power. The data collected was approximate because the brake was not accurately controlled and presented significant instabilities in the operation, without the ability to maintain a constant load or rpm. When the data was sorted based on the power measurements from least to greatest, and averaged over a given range, the plots in Figure 4.2 resulted. In order to show the correlation of power (or coefficient of performance) with angular velocity (or Tip Speed Ratio),

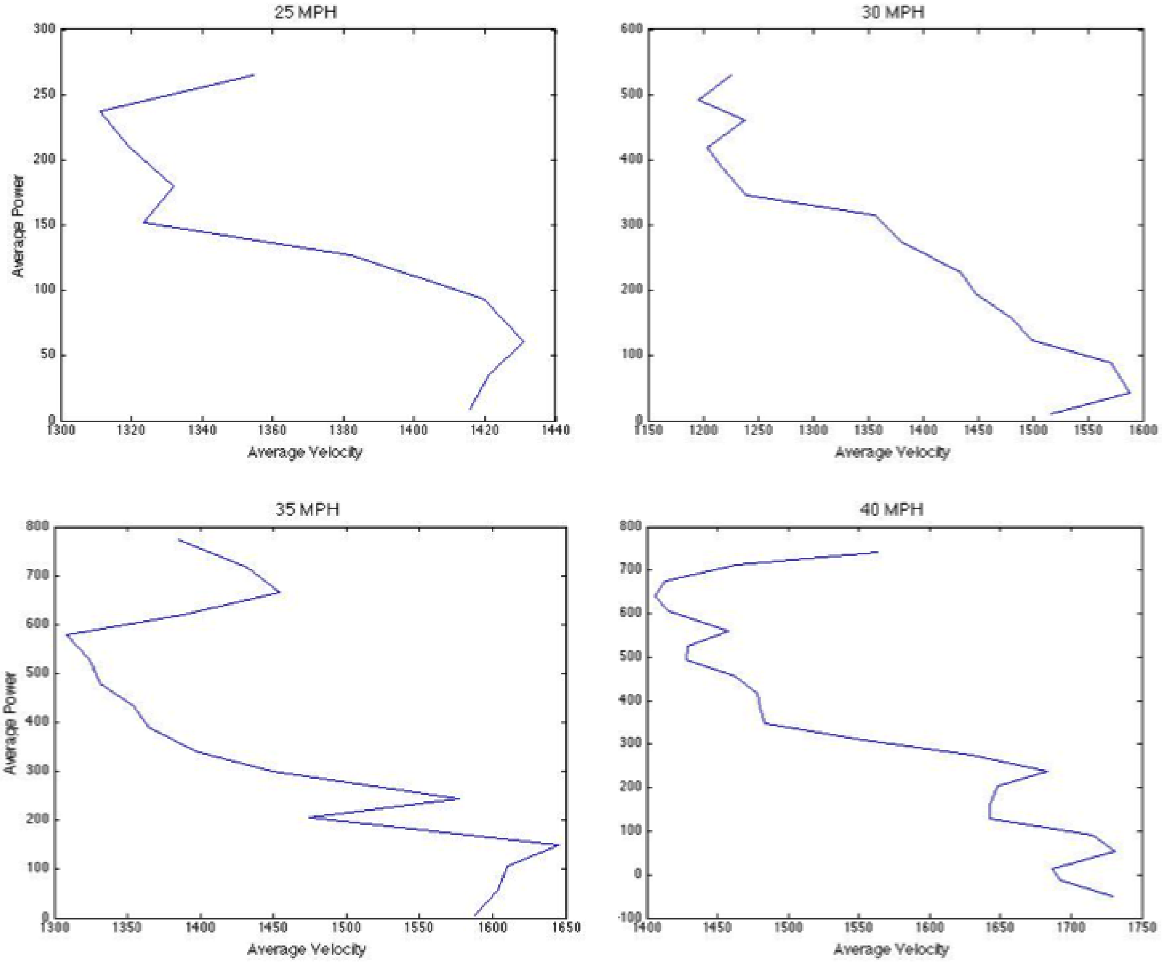

Figure 4.2: Prototype 1 Experimental Results

the angular speed was averaged for the same data points that fell in a given range of power, and then the units were converted from rad/s to rpm. The data is noisy, but a clear trend shows the free spinning velocity, at zero load, to be in the 1400 to 1800 rpm, increasing with wind speed. As the load was applied, the power dissipated in the brake increased to a maximum of 300 for the 25 mph wind, and up to a maximum of 800 Watts, saturating at that value for wind speeds of 35 and 40 mph. This is indicative of the fact that the brake was being overpowered by the rotor and could not dissipate the amount of energy that the turbine was putting on the shaft. For the low speeds, 25 and 30 mph, as the brake was applied it went through a very nonlinear transition where the resistance torque jumped suddenly and stalled the turbine. The angular velocity decreased progressively from 1400−1500 rpm at free spin to about 1300−1200 rpm at relatively low torque, at which point the next small increase in the brake control resulted in a large jump in torque (visible also at the intermediate values in high wind speed plots) and the turbine stalled. In the last plot, starting at about 650 watts, the power curve almost remains flat. At this time the rheostat was being adjusted to increase braking force, however, because the system had heated up significantly braking force was decreasing, thus allowing the angular velocity to increase. The first power recordings measured between 100 watts and, a closer to predicted power of, 800 watts.

In summary, power measurements in this system were very preliminary. The inconsistency came primarily from the fact that the brake had poor repeatability and was poorly controlled by the potentiometer provided by the manufacturer. It was overpowered for this system, and had characteristics significantly affected by heat and angular velocity. Additional factors that added noise to the system were: system misalignment, blade and generator adaptor imbalance, bearing and brake placement, blade manufacturing inconsistencies, and varying velocity from the wind tunnel exhaust. One possible improvement to the system could have been to add an inertial wheel to help reduce the angular velocity fluctuations that resulted from imbalance, vibration, and varying wind speed. With the starting torque concerns, design improvement and manufacturing timeline would allow for the design of a better testing set-up. The first step was to find a brake suitable for future experiments.

4.2 Deflection Measurements

Early on, as the initial blade dimensions were being determined, structural integrity and stiffness became a concern. A very thin chord length, which leads to a very thin airfoil thickness, could result in significant deflection during operation to a degree that would be detrimental to performance. The manufacturing process and materials were specifically chosen to produce a blade that was as stiff as was possible. However, during prototype 1.0 testing significant deflection was easily observed. In order to better understand and quantify the amount of deflection at different wind speeds and loading conditions and to gather information concerning the need to include pre-deflection in the second prototype, a high-speed camera that could capture the blade at a fixed point during its rotation was used during an experiment. The camera was a Vision Research Phantom V12.1M, which is a grey scale camera with the capability of taking up to 1 million frames per second. The wide−angle lens was aligned such that the long edge was vertical and the lower short edge was aligned with the lower tip of the blade when the turbine was held in a vertical position as can be seen in Figure 4.3. The camera was programmed to take video at 6200 frames per second with a resolution of 1280 x 800 and was focused on the lowest point of rotation. The set−up can be seen in Figure 4.3 below. An initial shot was taken of the still blade next to a simple micrometer. Then, the

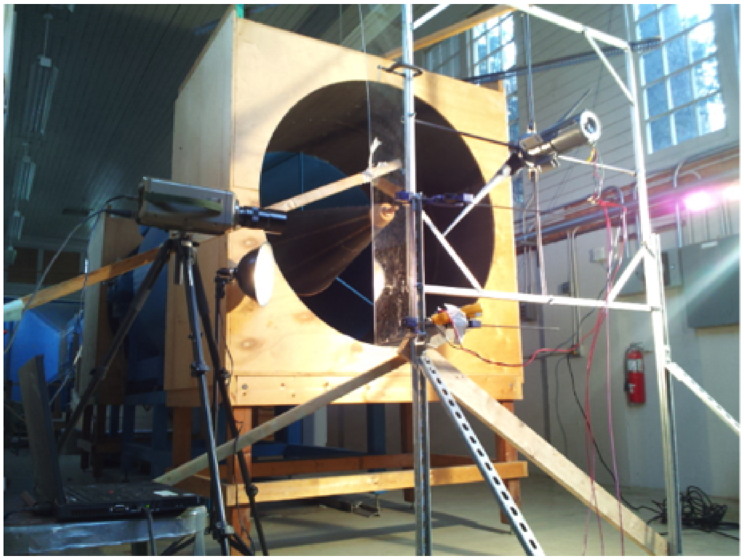

Figure 4.3: High Speed Camera Deflection Measurement Set−up

rotor was tested at operating conditions for varying wind speeds and brake loads, and high−speed videos recorded the deflection of the two blades during their rotation.

ImageJ was utilized to process the images. A program was developed that determined the location of the leading edge of the blade at nine evenly spaced intervals. The amount of deflection at each section was determined by comparing the high speed images against the motionless calibration image, and the displacement of the leading edge at each of the nine sections subtracted from their static positions. Figure 4.5 is the resulting data displayed graphically:

The deflection represented in figure 4.5 shows the results for the blade from just after mid-span to the tip, with the wind direction going from bottom of the page to top and the blade deflecting in the downwind direction. The pre−deflection that was included in the second prototype was based on the 35 mile per hour loaded

Calibrated Image Blade In Rotation

Figure 4.4: Comparison of Calibration Image and Rotating Blade Image

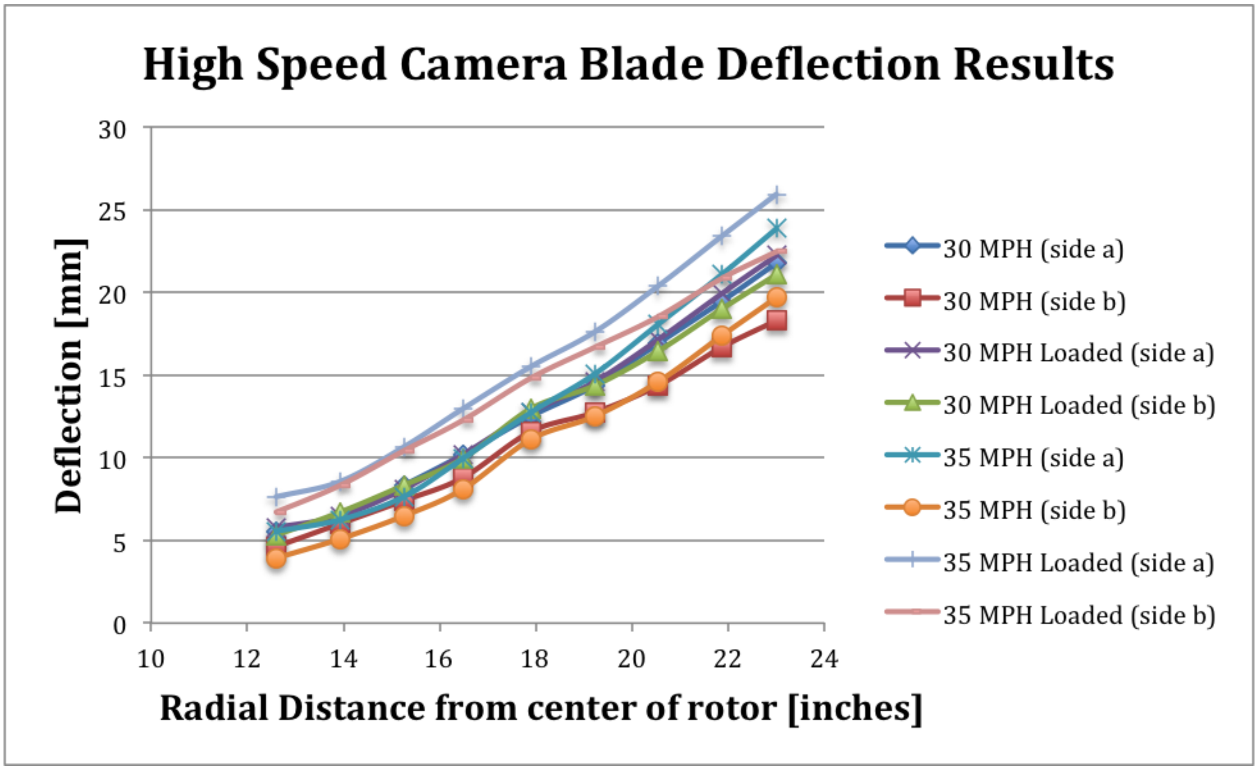

Figure 4.5: Processed Deflection Results

case, with a smooth polynomial line fit to the data and scaled down to 75% of the original. Though only the last half of the blade was visualized in the high-speed video the entire blade was pre−deflected based on the best fit curve. Zero deflection near the root as imposed on the polynomial fit to match the blade physical response where it was not visualized. Therefore, the application of the curve-fit to the entire blade length is an adequate approximation for the predeflection.

It is not desirable for the blade to be deflected towards the wind during operation, therefore only a partial deflection was considered for the second prototype. However, a significant pre−deflection should not be a concern because centrifugal

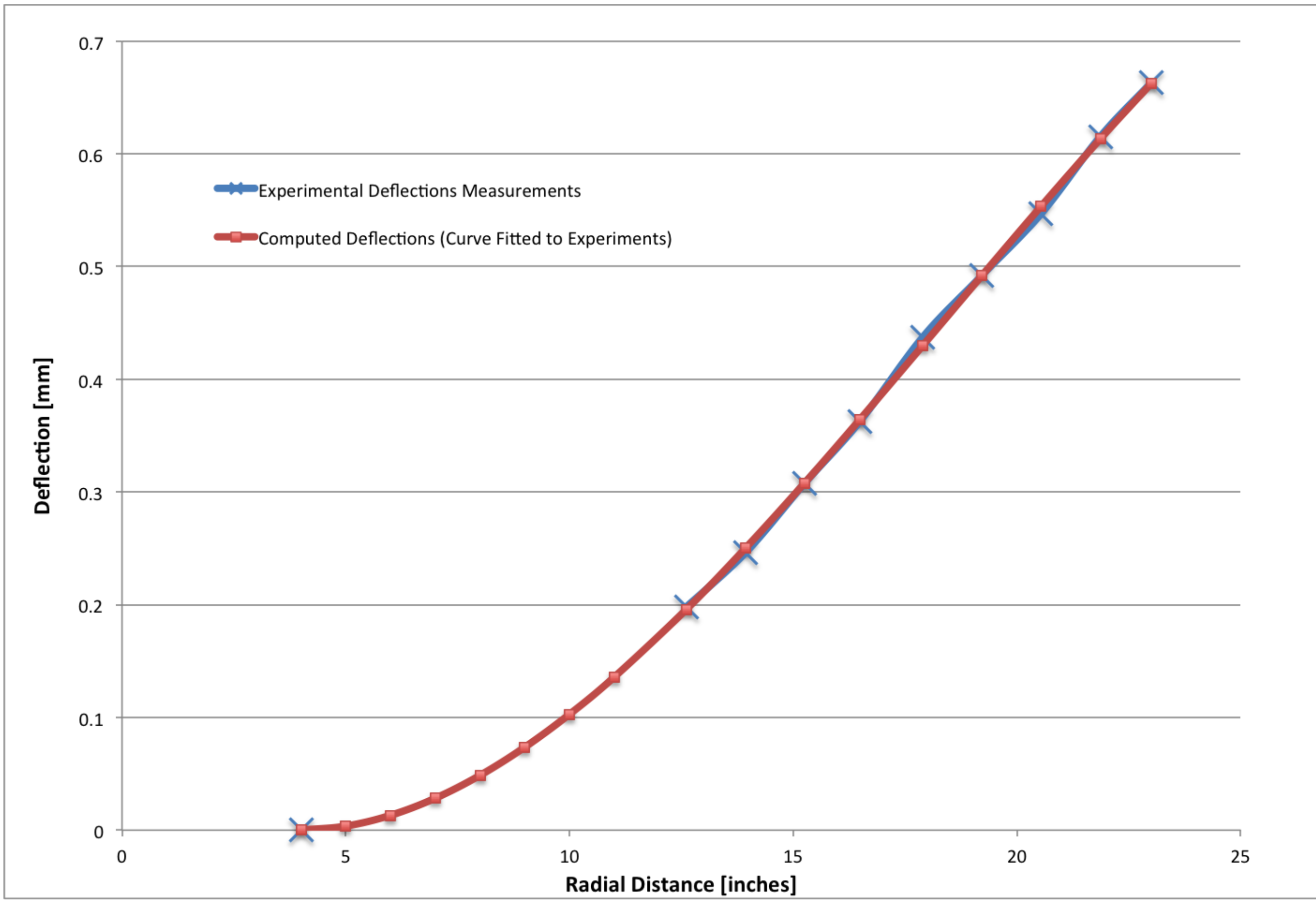

Figure 4.6: Deflection of the Blade with a third Order Best Fit Polynomial

force initially acts to reduce the pre−deflection even without the force of the wind or other aerodynamic forces. The blade deflection was taken as a whole without separating out the deflecting and straightening forces. The opposite effect of rotation (centrifugal) and aerodynamic loading will work to minimize deflection if the rotor operates far from the conditions used to set the added pre−deflection: if the wind speed is lower, the loading but also the rpm will be smaller; if the wind speed is higher, the loading will increase, but so will the rpm, leading to contained blade deflection. Secondarily, a full pre−deflection would be unwise because the exact effects of the modified twist and material lay−up on the bending characteristics of the blade on the second prototype were unknown at that time. A profile view of the 2.0 design shows the resulting blade pre−deflection. Further testing is needed to determine the resulting deflection of the second prototype.

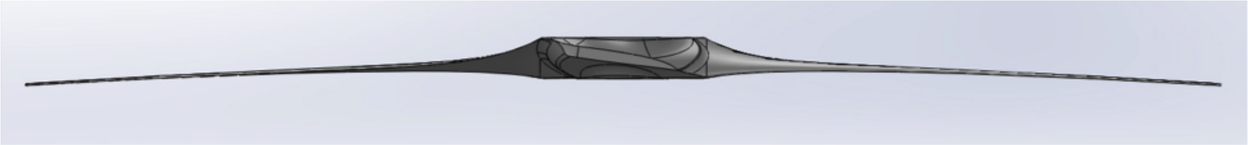

Figure 4.7: Profile View of Prototype 2.0 Blade Design

4.2.1 Starting Torque

Clearly observable in the first prototype experiment was the fact that the blade was not self−starting. A trade−off study was conducted to determine the effect of twist changes on the efficiency of the blade. Figure 4.8 is a comparison of the starting torque improvement and the loss of efficiency.

Four different twist cases were evaluated. The first case, was the optimal case that the first prototype was based on, with a root twist of 17 degrees. The three other cases were 25, 35, and 45 degrees at the root. In each case, the adjacent airfoil sections were adjusted as necessary to maintain a smooth transition from the root section out the tip. As the twist increased the number of affected airfoils also increased, which then resulted in a much greater increase in starting torque (as more airfoils were adjusted towards the the wind) and a greater decrease in efficiency at high Tip Speed Ratios. Another change that resulted from adjusting the twist was

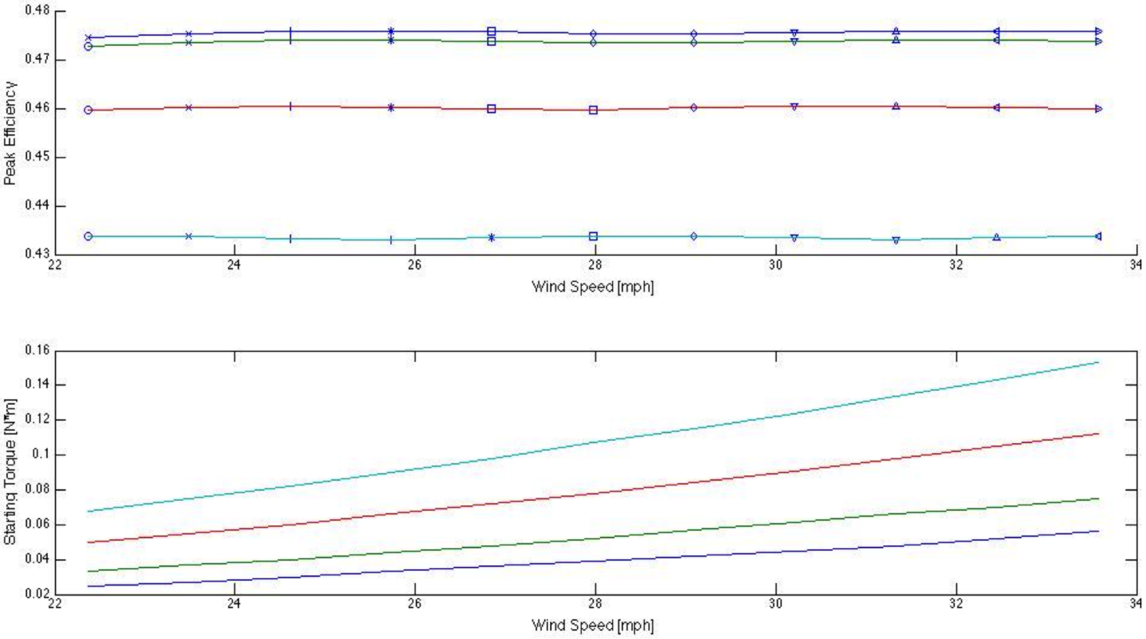

Figure 4.8: Trade−off Study of Efficiency and Starting Torque

the angular velocity at which the efficiency was the highest. The angular velocity was evaluated at 100 rpm increments and the decrease was noticeable even at that resolution. The decrease in rotor speed is undesirable in coupling with a generator. The 25 degree twist case was selected because it resulted in the smallest decrease in both efficiency and angular velocity, while still appreciably increasing the starting torque. Lastly, the theoretically predicted starting torque for the 25 degree case was compared with the generator design and confirmed that the rotor torque well exceeded the generator design.

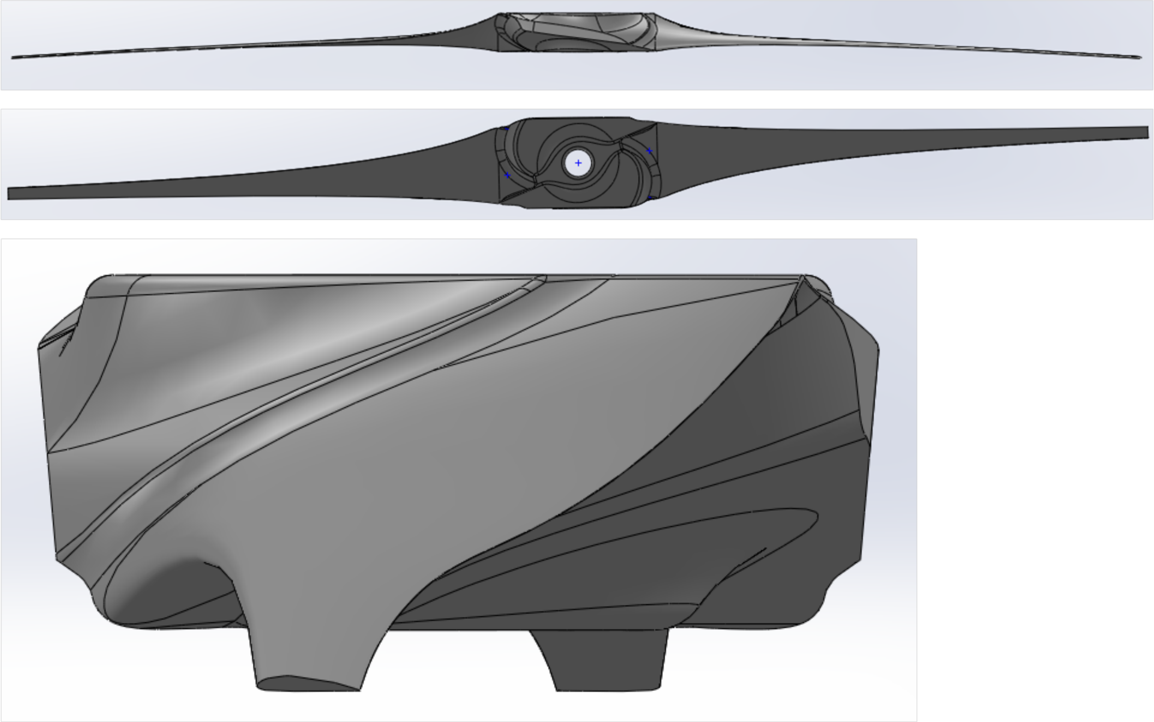

Figure 4.9: Multi−view of Prototype 2.0

4.2.2 Prototype 1 Lessons Learned and prototype 2 changes

Prototype 1 evaluation was successful in that it yielded a number of lessons learned. First, a better system for controlling the rotor and measuring the power output was needed. Second, even with the thicker airfoil, the reduction in solidity resulted in significant deflection of the rotor during operation. One method to minimize that effect is to pre-deflect the rotor such that under operating conditions it operates effectively. Finally, the highest efficiency twist profile resulted in a very low starting torque; an undesirable condition for direct coupling with a generator. One way to solve the problem is to increase the twist of the airfoil sections near the root, but at the cost of efficiency and angular velocity.

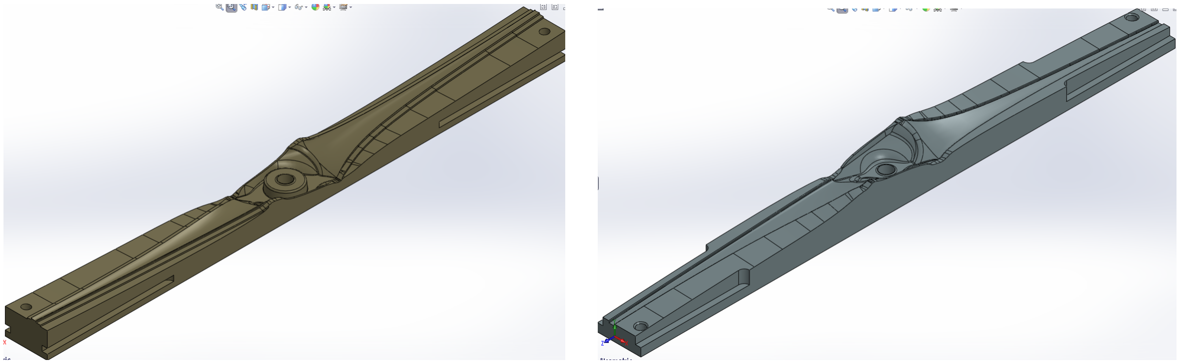

Upper Half

Lower Half

Figure 4.10: Prototype 2.0 Mold

The mold for the second prototype also has some unique features in order to improve the production process. The biggest change is having male and female mold halves that are designed to shear the carbon fiber matting that goes outside the rotor form. Also incorporated in the second prototype is a carbon fiber ′sock′ that prevents the fiber layers from slipping out of the mold or out of position during molding. This ′sock′ is carbon fiber matting that has been woven together to form a closed shape that can be pulled over the existing layers as a final layer that holds everything in place. Even though this thesis has not explored the strengthening effects that a variety of carbon fiber lay-ups, core making, and core alternatives can and do have on the stiffness and operating characteristics of the rotor, many combinations have been explored as a part of manufacturing the rotor.

4.3 Final Prototype Experiment

The first set of experiments was designed to provide general power data to validate the initial design theory. The first and second prototype designs were tested using the first method. In this second set of experiments, the goal was to characterize the second prototype blade with high accuracy torque and rotational speed measurements, at multiple wind speeds in a repeatable test in order to provide publishable results.

4.3.1 Kirsten Wind Tunnel Experiment

The primary advantage of the Kirsten wind tunnel compared to the Aerodynamics Lab wind tunnel, is that it is large enough that the rotor can be tested inside the test section as opposed to downstream of the exhaust of a smaller open return wind tunnel. The uniform flow that the Kirsten tunnel exhibits makes the experimental data obtained under this ideal conditions more comparable to the results found in computational modeling.

The F. K. Kirsten Wind Tunnel opened for testing in 1939, and is housed in a concrete and brick building on the University of Washington campus, adjacent to Guggenheim Hall. It is a double-return, closed circuit wind tunnel. The test section has a rectangular cross-section eight feet high, twelve feet wide and ten feet long, with fillets in the corners. The test section is vented to the atmosphere and can be viewed from all sides. Two 500-hp dc motors drive two 14 feet 9 inches diameter, seven-blade fans to provide the test section with airspeeds of 200 MPH for a typical-sized wind tunnel model. The tunnel is capable of airspeeds of 250 MPH with a clean test section. Figure 4.11 shows three: plan, front and elevation, views of the Kirsten wind tunnel.

The test set-up includes a $T-$slot frame with a wooden base to support a Torspec 100TCD eddy current brake, which was directly coupled to the blade via a single aluminum adaptor. The blade was centered in the tunnel both vertically and horizontally. A photograph of the setup inside the Kirsten test section is shown in Figure 4.12.

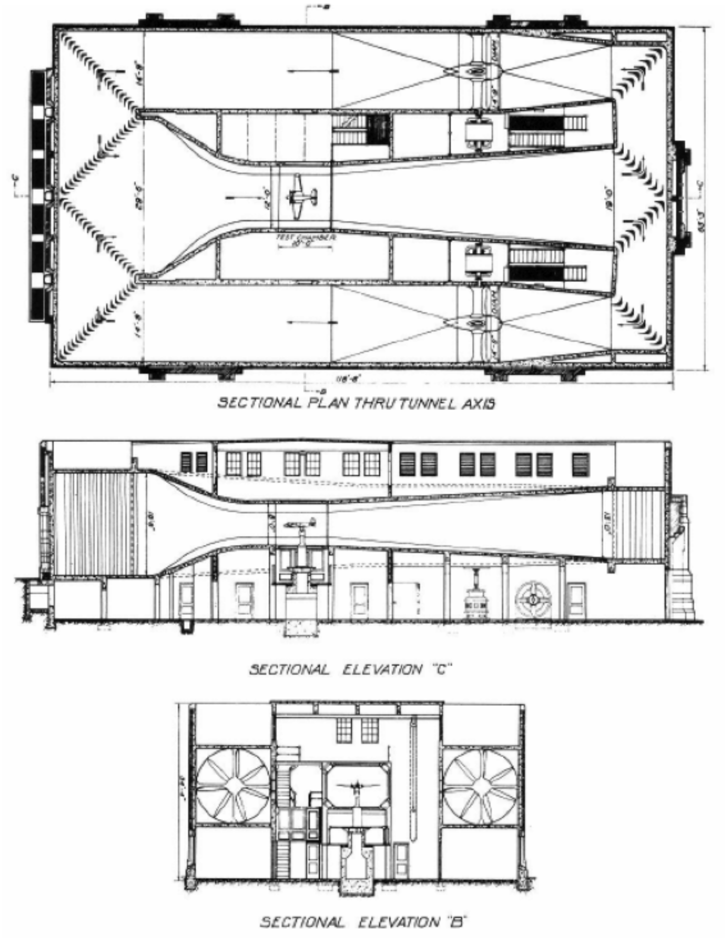

Figure 4.11: Kirsten Wind Tunnel Three−view Schematic

Furthermore, it was meticulously leveled and squared with the tunnel to ensure accurate data collection. A metal bar with plumb bobs on both sides was affixed square to and across the wooden base. Carpenter squares were taped to the floor of the text section square to the test section and measuring tapes were extended forward from the squares. The locations of the plumb bobs were measured and then the stand was adjusted so that the plumbs on both sides measured the same

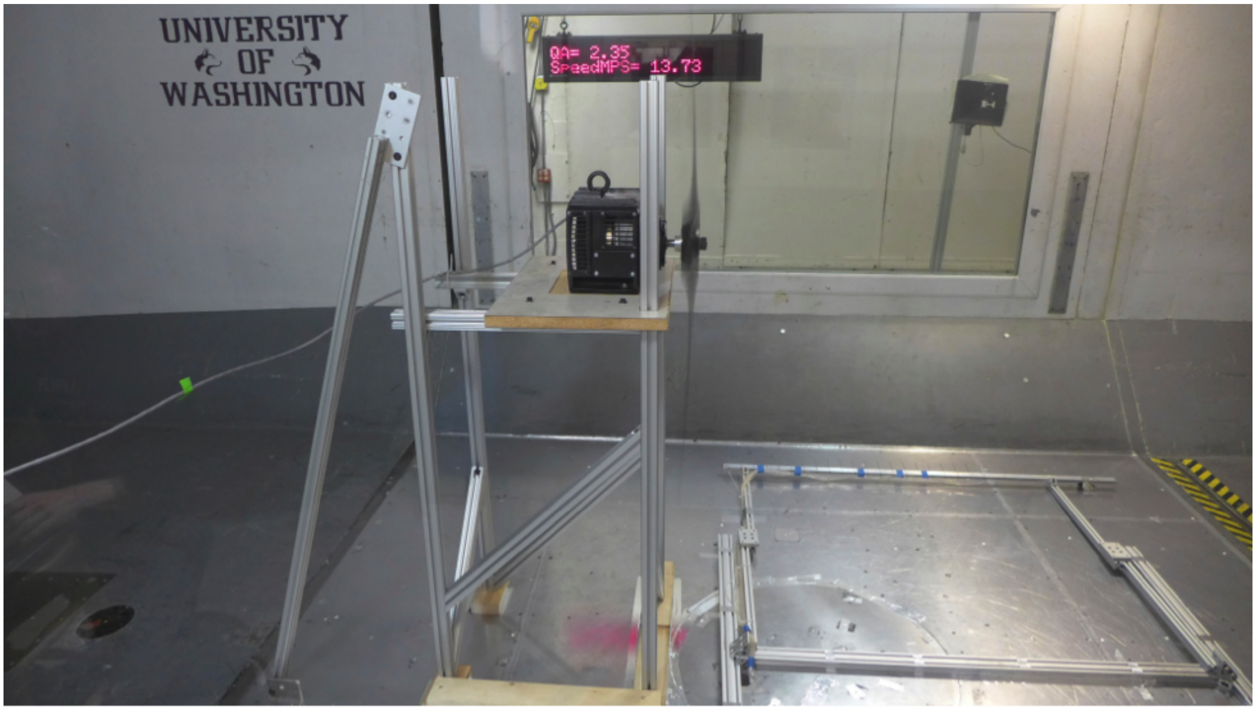

Figure 4.12: Kirsten Experimental Set-up

distance from the back of the test section. A picture of this labor−intensive process, carried out meticulously and in a highly professional manner by a team of undergraduate Kirsten operators, is shown in Figure 4.13.

4.3.2 Experimental Results

Wind tunnel measurements were taken for wind speeds increasing at half m/s intervals from 10 through 14 m/s and then at one m/s intervals from 14 through 17 m/s. At each wind speed, the angular velocity was modulated to simulate a variety of loading conditions. The eddy current brake was controlled by a closed loop control board that allowed us to control the angular velocity of the turbine in a

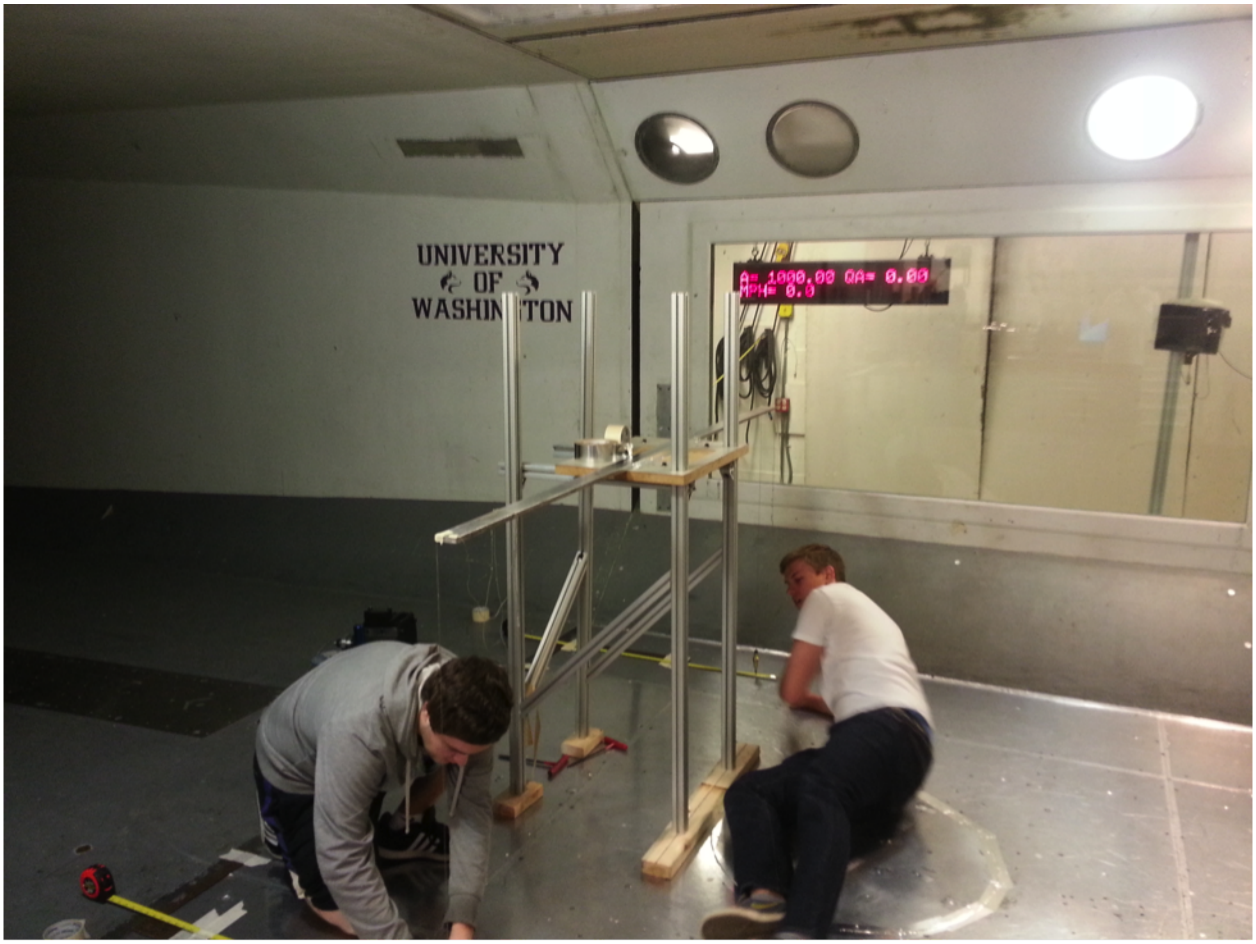

Figure 4.13: Squaring the Rig to the wind Tunnel Test Section

similar manner as a generator would. The controller had an output for angular velocity, and coil amperage was also measured so that it can be correlated to determine torque, and thus power, generated by the turbine. We started at low speed and then gradually worked our way up to about 24 m/s in an attempt to force the blade to accelerate to operating speed without using an external start−up mechanism. Initial attempts failed and the set-up had a significant vibration at wind speeds at or above 20 m/s. We adjusted the cross−supports and added an angled support that was bolted to the floor. Stiffness was immediately and significantly improved, so we further attempted to start the turbine up to about 30 m/s. The blade rotated freely, but did not reach the expected unloaded operating speed of about 3000 rpms. The next concern was blockage and vorticity from the static pressure rig on the flow hitting the turbine in addition to some blockage immediately behind the blade by the cross−member supports. The pressure rig was laid down and secured to the floor (removal was not necessary) and the forward cross−member was lowered as much as possible. The change did increase overall angular velocity of the blade, but not enough for the system to reach full speed self sustaining regime, so an external starter was applied with a max angular velocity of 850 rpms, but without success. Multiple blades have been manufactured so prototype version 2.0 blade # 2 was replaced with blade #4 (on hand were #2, #4, & #5 (Blade #1 was manufactured, but not delivered due to a weak structure). Blade #4 did reach up to 820 rpms without self sustaining rotation. Finally, a faster starting motor was acquired and the blade did accelerate to its full speed regime at 10 m/s. Causes for the high start−up speed were considered to be three fold. First, a friction sound in the eddy current brake was heard during part of the rotation that had not been previously observed and secondly there was significant additional blockage just after the blade due to the supports that had not been present in earlier experiments because the system was raised higher, so the front vertical supports that previously were under the board that the brake is bolted to, are now sticking up about 1.5 feet above the board in order to allow us to run in the center of the wind tunnel. More importantly however, is the significant amount of resistance torque that the eddy current brake maintains without an input current. Figure 4.14 is the data curve that correlates angular velocity, intensity, and torque provided by the manufacturer.

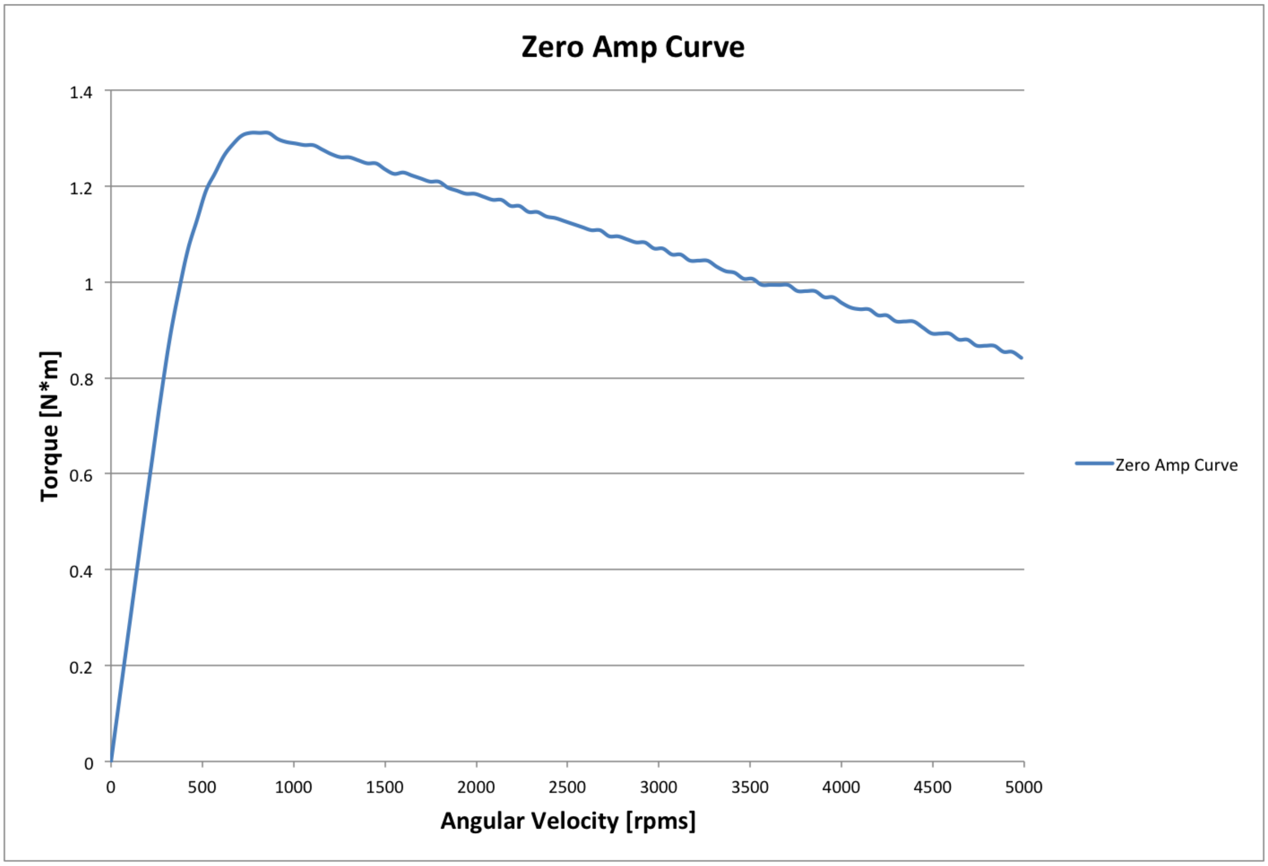

Figure 4.14: Torque, Angular Velocity, and Intenisty Curves for the Eddy Current Brake

Once the starting torque is overcome by the rotor it begins to spin, which in turn will produce more torque. However, the increase in torque from the wind is smaller than the dramatic increase in resistance torque in the eddy current brake. Notice that at low angular velocity around 600 rpms the torque in the brake peaks to approximately 1.3 N*m of torque. Because of the need for a large angular velocity in order to directly couple with an efficient and cost effective generator, the overall torque produced by the rotor is very low and therefore was unable to overcome the large increase in torque from the free spinning brake. Due to these problems the system had to be started externally with a higher speed friction starter while the wind was blowing and then the data measurements were taken.

Data acquisition and tunnel operation required multiple participants. In order to set the wind speed, the local operator and safety observer relayed the desired speed to the control booth. The control booth operator adjusted the wind tunnel fan speed and pitch to achieve the equivalent flow rate through the test section. When the control booth operator was satisfied with the condition of the flow, data acquisition began. The eddy current brake was then engaged by a third person via LabView software and two types of data were recorded. A time stamp was recorded with each data point which included the eddy current brake coil amperage and the frequency of rotation. After the brake was engage the booth operator again adjusted the wind tunnel to ensure that flow through the test section was maintained. During the pressure testing a similar process was followed, while a third system gathered pressure readings from all the pitot static tubes simultaneously.

Back−Pressure Measurements

An additional frame was set−up after the initial power trials that included 21 pitot static tubes used to measure backpressure in front of the turbine. A picture of the pressure measurement setup is shown in Figure 4.15.

This information is critical for exhaust recovery because any backpressure that feeds upstream will change the operating characteristics of the exhaust system. This is the one absolutely unacceptable result for this design. A test with the shroud design was not possible in this tunnel because a prototype model has not yet been manufactured.

Pressure measurements were taken by an electronic pressure scanning system (EPS).

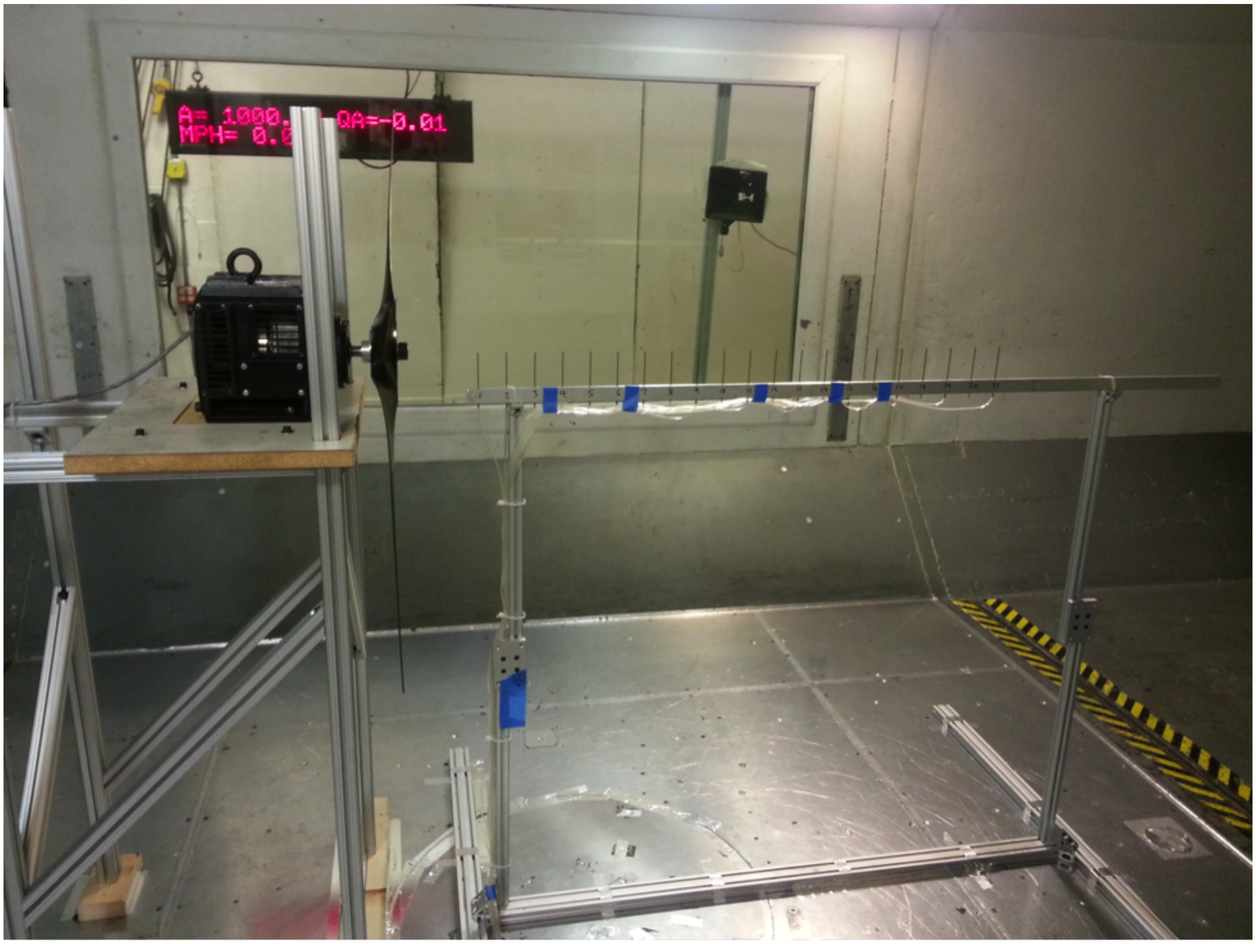

Figure 4.15: Experimental Set−up with Pressure Rig

UWAL has two Scanivalve EPS modules: 1) 128−port, 5−psi range module using 64 transducers, Model ZOC 33; 2) 32−port, 0.72−psi range module, Model ZOC 23B. Both modules have an accuracy of 0.05% of the full−scale range. The system was automatically calibrated. This system allows simultaneous recording of up to eight modules.

Figure 4.17 is instantaneous pressure data taken during an experiment. The data

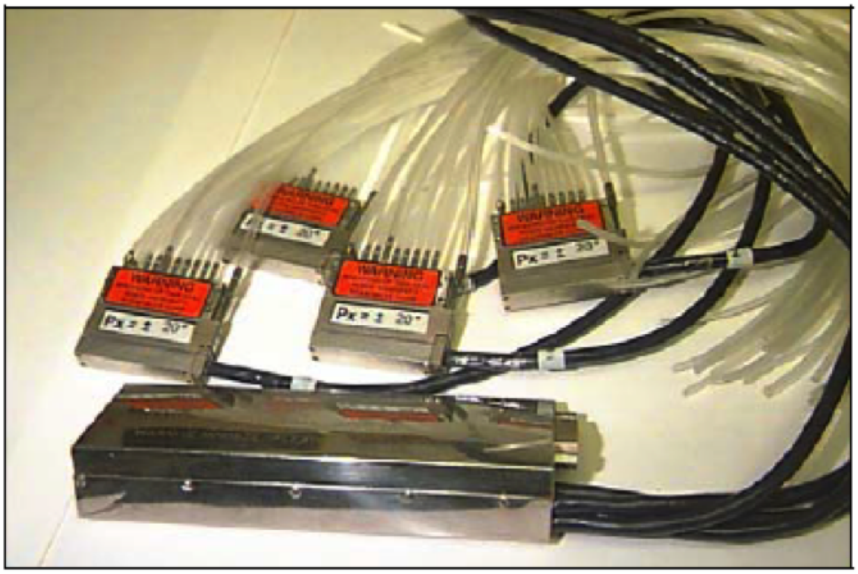

Figure 4.16: Pressure Transducers Used in Pressure Data Gathering

represents the pressure difference between the references pressure (upstream at the entrance to the wind tunnel test section) and the one at which the reading is being taken. A few corrections that can be made in the future is to have the reference pressure be outside the wind tunnel, which was not the case in this experiment. Further analysis is required, but clearly the turbine provides very little, if any, backpressure.

4.3.3 Torque/Power Data

Unlike the first experiment where torque was measured by a torque cell, the angular velocity by an encoder (optical) and the torque was applied a particle brake, in this more advanced stage, the eddy current brake filled the role of the brake, the torque cell, and the encoder. Though the frequency could be directly measured and

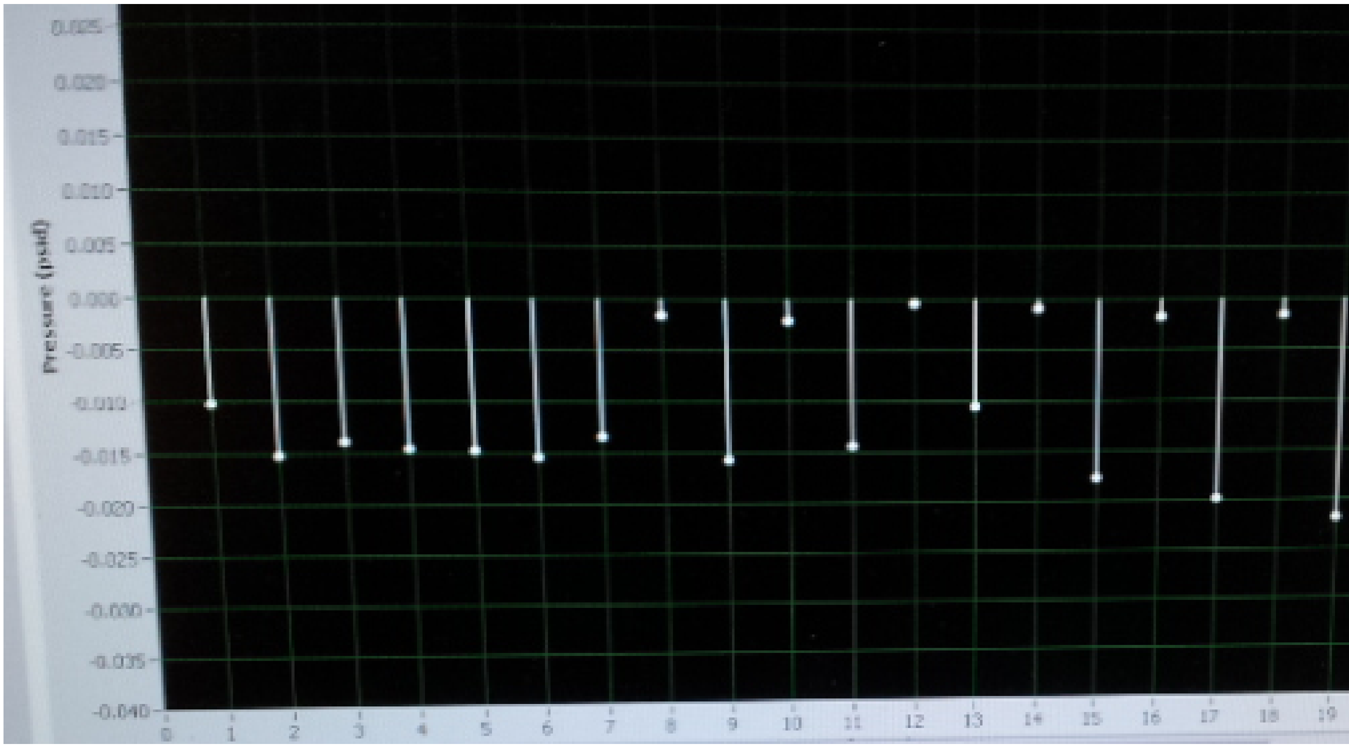

Figure 4.17: Preliminary Pressure Data

controlled, torque data was not directly measured. The manufacturer provides a chart that correlates the coil amperage and the angular velocity with the torque. Figure 4.14 is one curve from that chart which is shown in full in figure 4.18. In order to determine torque at each data point, triple linear interpolation was used for each data point consisting of an angular velocity and a coil amperage in order to determine the torque measurement.

There were a number of valuable outputs from the eddy current brake system that were utilized to produce the compiled information in this section. Figure 4.19 represents the completely unfiltered data.

The first filter pass was to remove outliers and the fluctuations present when the torque in the brake was adjusted. Figure 4.20 is post filter 1.

Finally, the data at each angular velocity was averaged, plotted, and the points that represent the greatest amount of data were connected with a line.

The thesis provides great value in the final comparison of theory, computational results, and finally prototype testing. Figure 4.22 is a comparison of C$_P$ versus TSR (λ).

As expected, the theoretical values of power collapse onto one curve when non−dimensionalized. Similarly, the experimental data also collapses onto one curve when non-dimensionalized. This is a very nice result indicating that the data was acquired robustly, and that it satisfies dimensional similarity in terms of the Reynolds number and Tip Speed Ratio (the two non dimensional parameters that control the aerodynamic efficiency of the rotor) and also that the turbine performs as expected. An 11 to 14 percent increase in C$_P$ is the difference between the theoretical values and the Kirsten Wind Tunnel experimental values. This is related to the fact that the turbine presents a significant amount of blockage to the flow and therefore the 'infinite free stream' assumption is no longer valid, thus resulting in a higher efficiency than theoretically predicted. Data taken at 16 m/s, however, does not follow the same trends as the rest of the included data, because of an unexplained harmonic vibration during this test.

In each of the dimensional charts 4.23 4.24 4.25 4.26 the peak of power and torque are very near the theoretical values. Two important conclusions can be drawn from that result. The first is that the process chosen for manufacturing yielded a turbine shape that very accurately follows the given three−dimensional model. More importantly, the design process is validated by the fact that the data produced by the prototype follows the same form as it was theoretically designed for. Though there is some uncertainty in the interpolation of the torque data as described previously, the relationship of the experimental data to the theoretical values also indicates that the interpolation was accurate.

Data between 12.5 m/s and 14 m/s have a nearly identical drop at the higher angular velocities. This phenomenon can be explained by the control process of the wind tunnel. The turbine began at free spin instead of at rest and the angular velocity was reduced quickly because of time constraints up to a range near the ideal maximum efficiency. During the quick transition the wind tunnel operators were not able to keep pace with the increasing power extracted from the stream, thus the wind in the tunnel was slightly below the requested wind speed.

Experimental data exceeds the theoretical data in both torque and power. This error comes from how the experiment differed from theory. The blade itself provides enough blockage, even in the large wind tunnel, to produce a significant increase in power, where the theory is based on a blade in a infinite and uniform flow. The support structure also present a certain amount of blockage to the flow through the wind tunnel as well. Though less significant in magnitude, the wind tunnel also had wind speed fluctuations that could account for a small amount of the increased power if consistently above average.

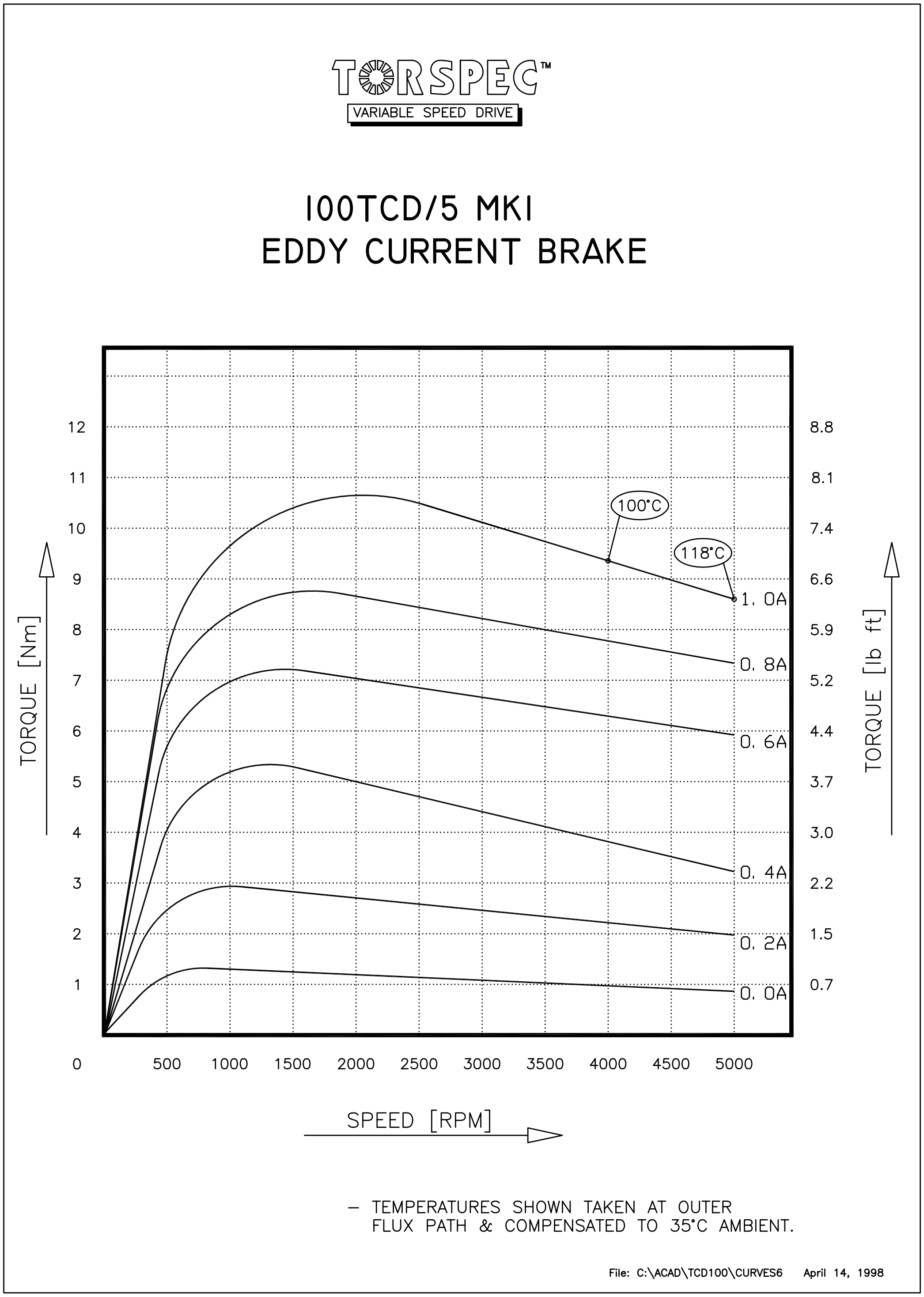

Figure 4.18: Angular Velocity, Intensity and Torque Relationship

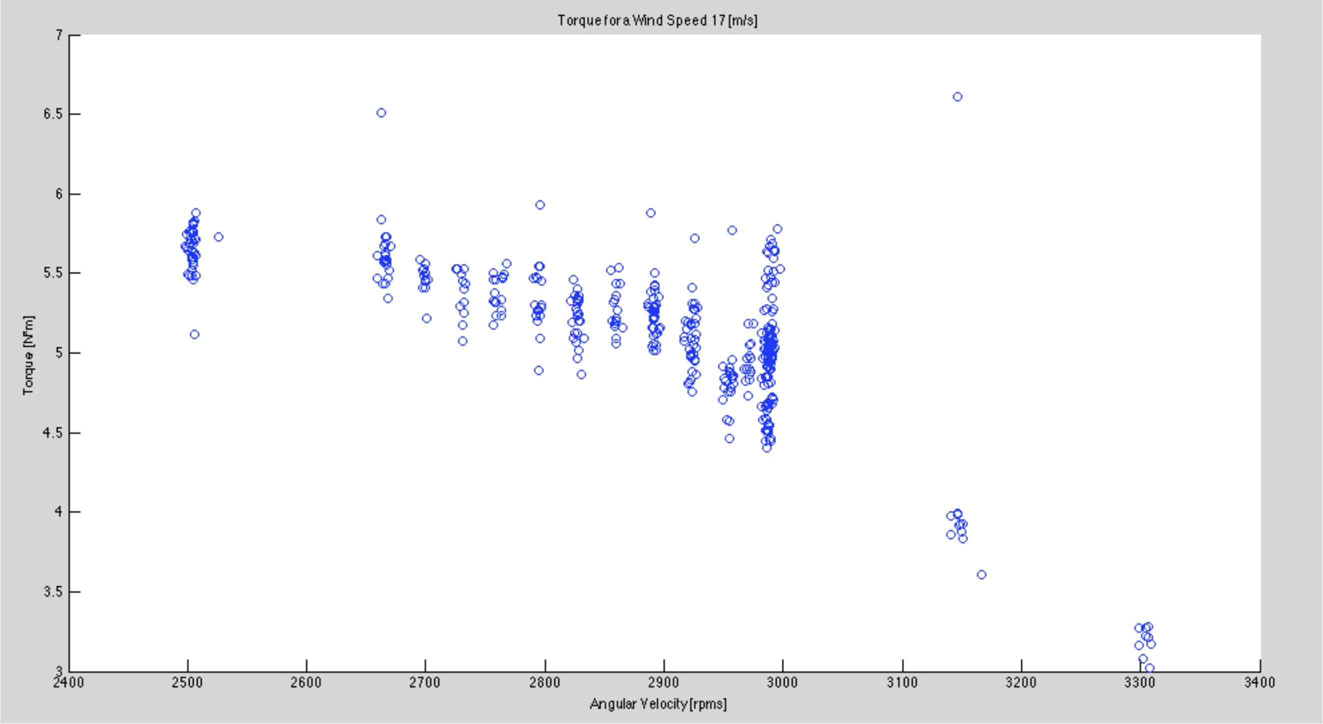

Figure 4.19: Unfiltered Torque Data

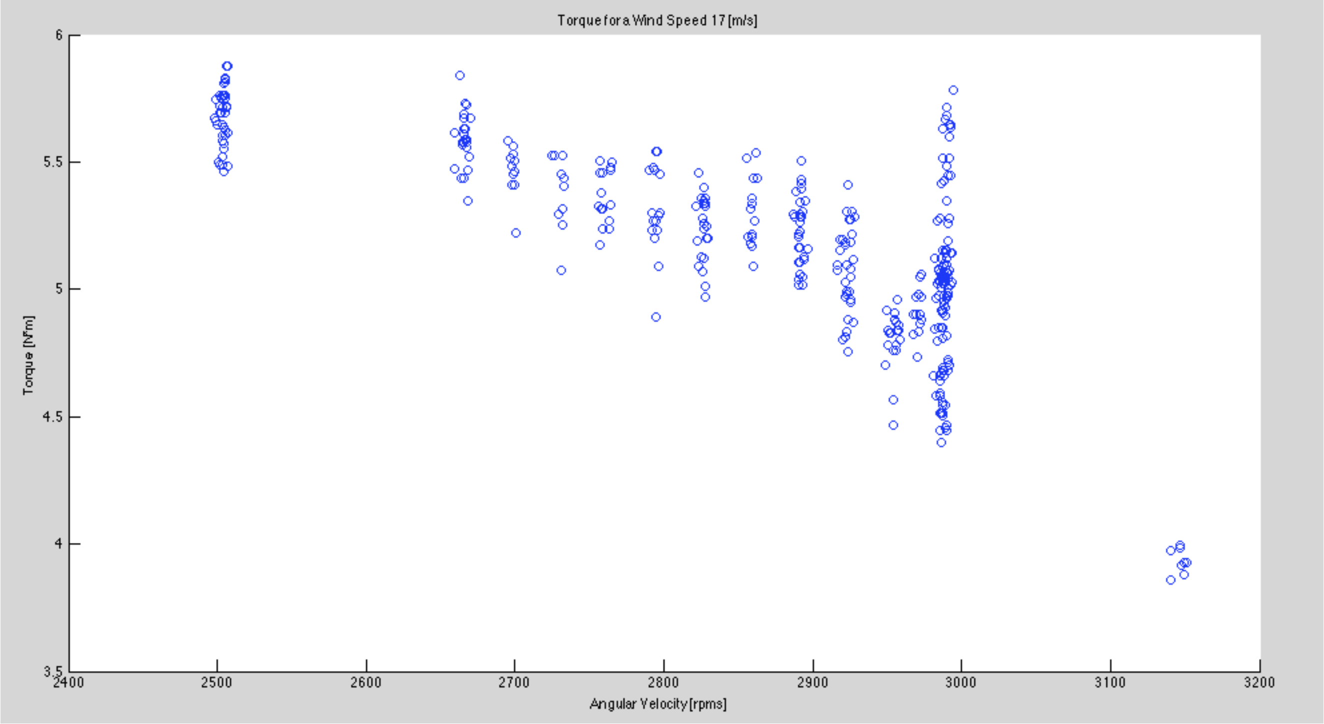

Figure 4.20: Filtered Torque Data

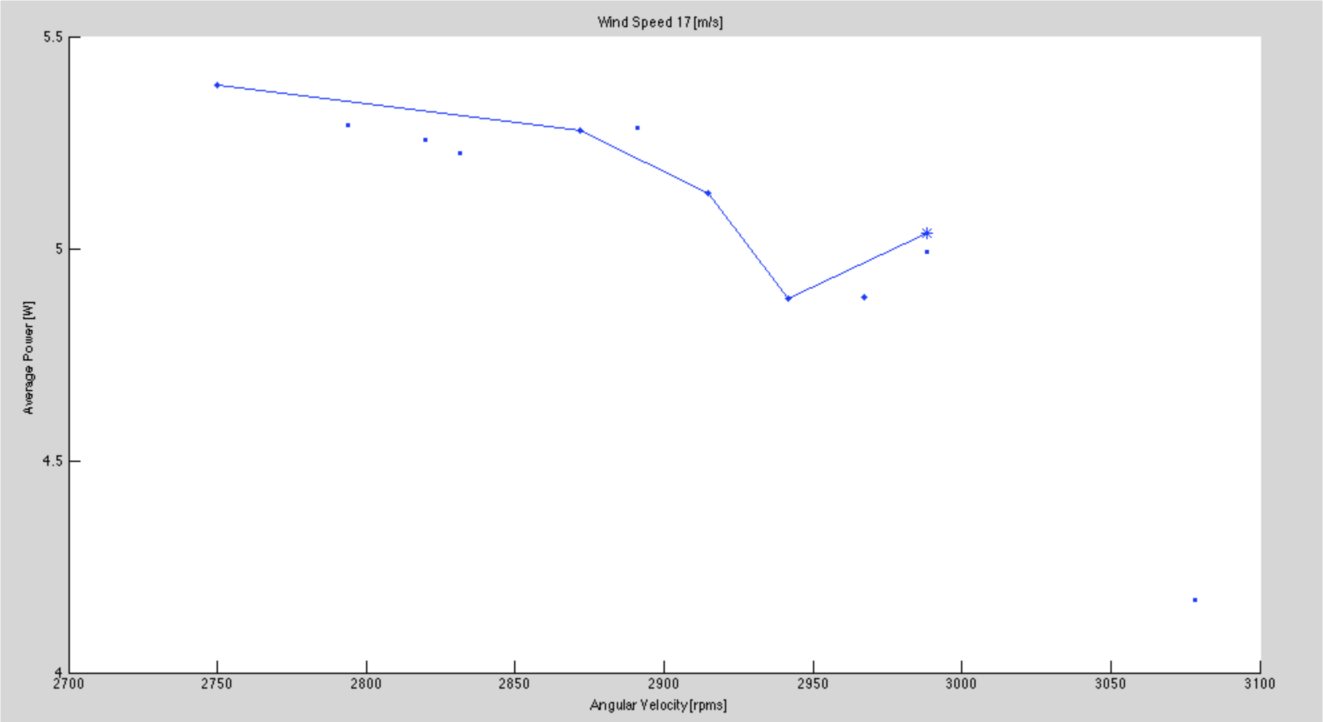

Figure 4.21: Averaged Torque Data

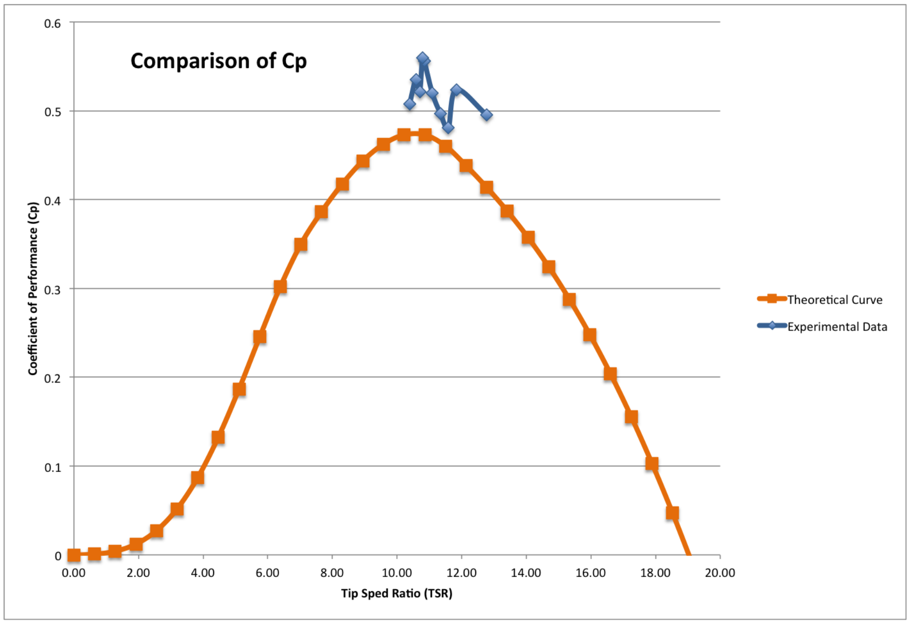

Figure 4.22: Coefficient of Performance Comparison Chart

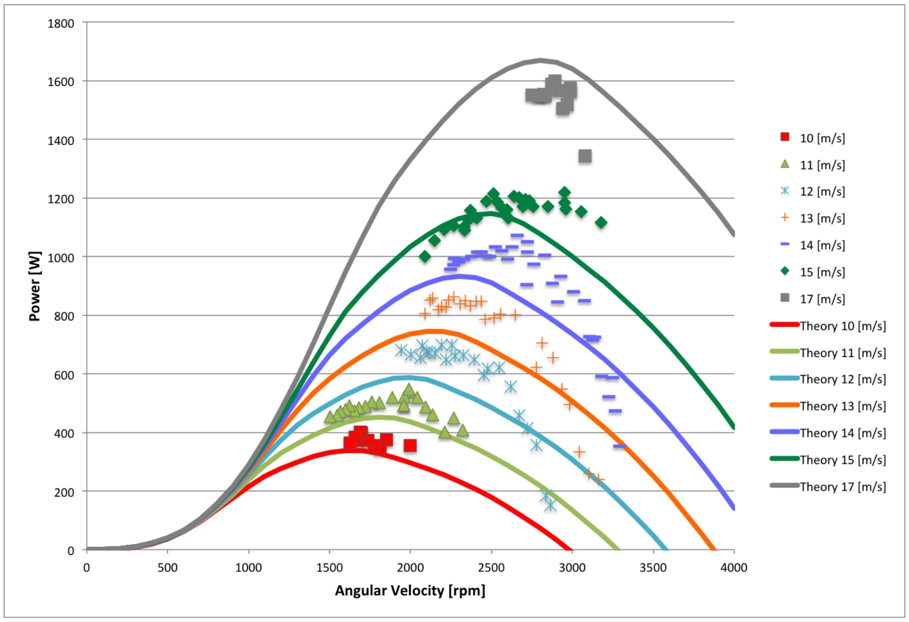

Figure 4.23: Power versus Angular Velocity

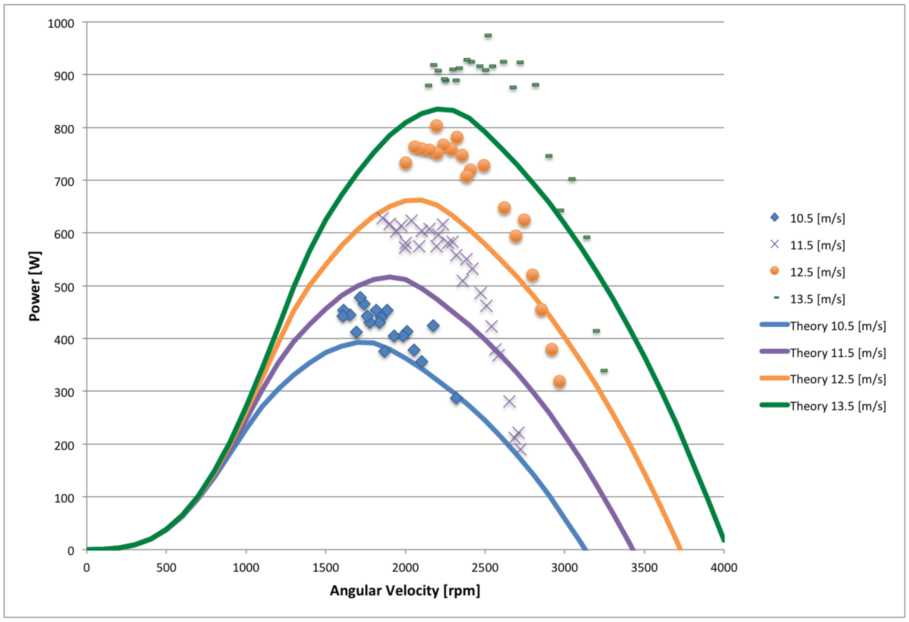

Figure 4.24: Power versus Angular Velocity

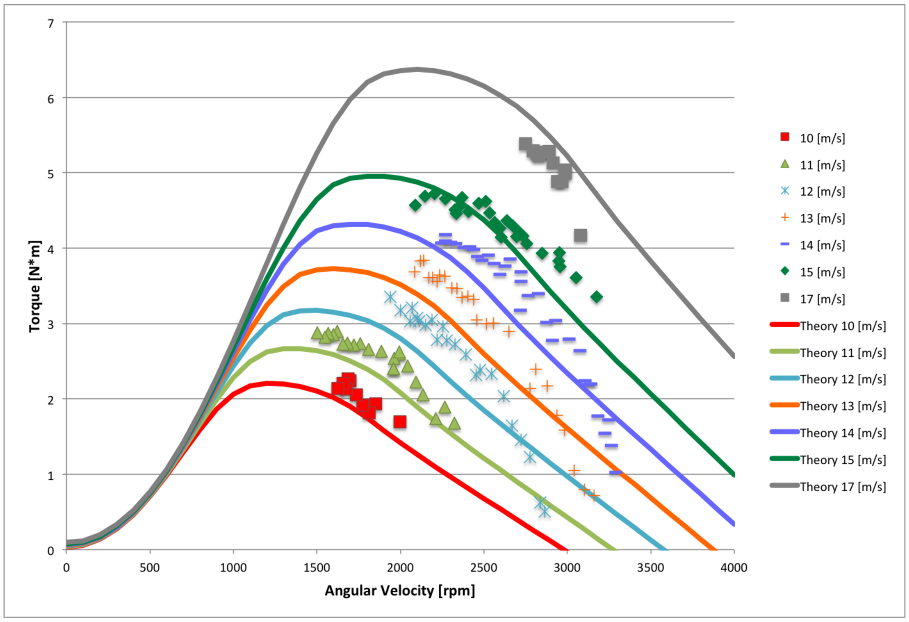

Figure 4.25: Torque versus Angular Velocity

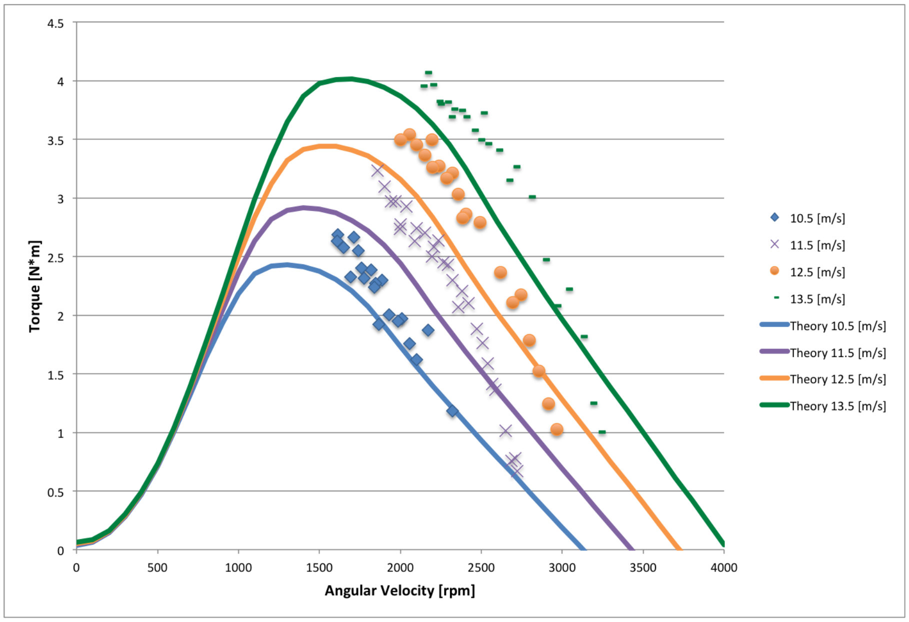

Figure 4.26: Torque versus Angular Velocity

Chapter 5

CONCLUSION

5.1 Conclusions

We have designed, manufactured and tested a small-scale wind turbine for specific application, namely the recovery of kinetic energy from the exhaust of building ventilation. Because commercial building ventilation, specially biomedical labs and data centers, operate at full capacity 24 hours a day, 7 days a week, year round, they represent an excellent target for the design of an optimized turbine that reaches high efficiency under a set wind speed and rotational velocity at the shaft (Tip Speed Ratio). With this very specific set of operating conditions (wind speeds of 10-15 m/s and rotational speeds of 2000-3000 rpms, for a Tip Speed Ratio of about 10) we performed the design and manufacture of a high efficiency small scale turbine (4 feet diameter). The prediction of very high efficiency provided by the design code, based on the Blade Element Theory, was verified by experiments in the wind tunnel, confirming that much higher efficiency than conventional utility-scale wind turbines can be achieved in this type of very focused application, up to 45-50%. The methodology presented in this thesis represents a robust design and manufacturing protocol to follow when designing a small−scale turbine. Lastly, the results provided here represent a holistic approach that includes theoretical, computational, and experimental data, with a feedback mechanism to inform the redesign of a more advanced prototype after the initial testing, to include a feature that was considered critical, such as the self starting torque, in the design workflow.

5.2 Future Work

Important work on this project still remains. First, the pressure data taken in the wind tunnel needs to be carefully processed and analyzed. Initial inspection seems to indicate that the data should be acquired with a fairing around the pitot static tubes that would allow measurements of static pressure in front of the turbine without self−induced flow disturbances. The effect of blockage in the wind tunnel should be analyzed and the data adjusted to account for the possible increase in efficiency and perturbation of the pressure gradient in front of the turbine. The results could then be compared on equal footing with the theoretical predictions. Secondly, a further experiment should be conducted to gather data for a wider range of angular velocities, from free spinning down to start-up, and longer time series should be collected for averaging once the wind tunnel has reached stable operation after setting the turbine load. In the near future, the first shroud prototype will be completed and follow−on testing will be conducted to determine the increase in efficiency from the shroud. Lastly, a second shroud design based on the ducted turbine theory could be examined to allow for the use of a single size rotor turbine on a larger range of exhaust outlets (going up to 6 feet diameter).